

# Laser Locking For Trapped-Ion Quantum Networks

A master's thesis submitted to the faculty of mathematics,  
computer science and physics, of the University of Innsbruck

in partial fulfillment of the requirements for the degree of

**Master of Science (MSc)**

carried out at the Institute of Experimental Physics

under the supervision of  
o.Univ.-Prof. Dr. Rainer Blatt  
and Dr. Ben Lanyon

presented by

**Helene Hainzer**

February 2018

# Abstract

This thesis reports on the setup of a transfer lock for trapped-ion based quantum network experiments. Such a system allows a cavity-mediated Raman process to be frequency-stabilized via laser locking. As a result, a coherent interface to map quantum information encoded in a trapped-ion qubit onto a photon qubit can be realized. The transfer lock scheme is based on frequency-stabilizing two lasers to an external reference-cavity, which was achieved in the course of this thesis. Linewidths and drift rates of the locked lasers were determined via frequency beat measurements. One of the locked laser systems was then used to stabilize the length of a test-cavity in air. Finally, a laser on the  $^{40}\text{Ca}^+$  optical qubit transition was locked to the reference-cavity, which allowed for the observation of Rabi flops.

# Contents

<b>1. Introduction</b>	<b>1</b>
<b>2. Quantum Networks</b>	<b>3</b>
2.1. Basic Principles of Quantum Networks . . . . .	3
2.1.1. Theoretical Concepts . . . . .	3
2.1.2. State of the Art in Quantum Network Experiments . . . . .	5
2.2. Trapped Calcium Ions as Network Nodes . . . . .	6
2.2.1. Atomic Level Scheme . . . . .	6
2.2.2. Trapping and Cooling . . . . .	7
2.2.3. Qubit State Readout . . . . .	8
2.3. Manipulation of the Electronic State of Trapped Ions With Lasers . . . . .	8
2.3.1. Light-Atom Interaction in the Dipole Approximation . . . . .	8
2.3.2. Coherent Manipulation and Dissipative Processes . . . . .	10
2.3.3. Raman Transitions in a Three-Level Atom . . . . .	13
2.4. Coupling a Trapped-Ion Qubit to a Photon Qubit . . . . .	15
2.4.1. Cavity Quantum Electrodynamics . . . . .	15
2.4.2. Cavity-Mediated Raman Process . . . . .	18
2.5. Trapped-Ion Quantum Network Protocols . . . . .	19
2.5.1. Quantum State Transfer From an Ion to a Photon . . . . .	20
2.5.2. Ion-Photon Entanglement and Remote Ion-Ion Entanglement . . . . .	21
<b>3. Lasers and Laser Locking</b>	<b>23</b>
3.1. Basic Principles of Laser Operation . . . . .	23
3.1.1. General Principles . . . . .	23
3.1.2. Diode Laser . . . . .	24
3.1.3. Titanium Sapphire Laser . . . . .	25
3.1.4. Laser Linewidth and Drift . . . . .	26
3.2. Frequency-Stabilization of a Laser . . . . .	27
3.2.1. An Optical Cavity as a Frequency Reference . . . . .	27
3.2.2. Pound-Drever-Hall Laser Locking Scheme . . . . .	33
3.2.3. Feedback Elements of Lasers . . . . .	36
3.3. Characterization of a Stabilized Laser System . . . . .	37
3.3.1. Linewidth Estimation Based on the Spectrum of the PDH Error Signal . . . . .	38
3.3.2. Frequency Beat Measurement . . . . .	41
3.3.3. Ramsey Experiment . . . . .	44

## Contents

<b>4. A Transfer Lock for Cavity-Mediated Raman Transitions</b>	<b>46</b>
4.1. Our Approach to Frequency-Stabilize the Cavity-Mediated Raman Process and Experimental Goals . . . . .	46
<b>5. Experimental Setup of the Transfer Lock</b>	<b>49</b>
5.1. Reference-Cavity and Vacuum Chamber Assembly . . . . .	49
5.2. Reference-Cavity Characteristics . . . . .	51
5.2.1. Zero-Crossing Temperature . . . . .	51
5.2.2. Geometry . . . . .	52
5.2.3. Mirror Properties . . . . .	53
5.3. Lasers . . . . .	57
5.3.1. Ion-Cavity Locking Laser . . . . .	57
5.3.2. Raman Laser . . . . .	57
5.4. Optical and Electronic Setup of the Transfer Lock . . . . .	58
5.4.1. Optical Setup . . . . .	59
5.4.2. Electronic Setup . . . . .	59
<b>6. Characterization of the Frequency-Stability of the Locked Lasers</b>	<b>61</b>
6.1. Linewidths of the Lasers . . . . .	62
6.1.1. MSquared Ti:Sa Laser and Diode Laser at 785 nm . . . . .	62
6.1.2. MSquared Ti:Sa Laser at 729 nm . . . . .	66
6.2. Drifts of the Lasers . . . . .	67
<b>7. Application of the Stabilized Laser Systems</b>	<b>70</b>
7.1. Test Ion-Cavity Lock at 785 nm . . . . .	70
7.1.1. Test Ion-Cavity Properties . . . . .	70
7.1.2. Test Ion-Cavity Lock Characterization . . . . .	72
7.2. Manipulation of a Trapped $^{40}\text{Ca}^+$ Ion on the 729 nm Qubit Transition . .	76
<b>8. Conclusion and Outlook</b>	<b>78</b>
<b>A. PDH Error Signals of the Lasers at 785 nm and 729 nm</b>	<b>80</b>
<b>B. Beat Note Between Diode Laser and MSquared Ti:Sa Laser</b>	<b>82</b>
<b>C. Laser Drift Measurements</b>	<b>83</b>
<b>Bibliography</b>	<b>85</b>
<b>Acknowledgments</b>	<b>90</b>

# List of Abbreviations

AC Alternating Current  
AOM Acousto-Optic Modulator  
ATF Advanced Thin Films  
CCD Charge-Coupled Device  
CQED Cavity Quantum Electrodynamics  
CW Continuous Wave  
DC Direct Current  
DL Diode Laser  
ECDL Extended-Cavity Diode Laser  
EOM Electro-Optic Modulator  
FALC Fast Analog Linewidth Control  
FFT Fast Fourier Transform  
FSR Free Spectral Range  
FWHM Full Width at Half Maximum  
GTP Glan Thompson Polarizer  
HV High Voltage  
HWHM Half Width at Half Maximum  
ICE Instrument Control by Ethernet  
IQOQI Institute for Quantum Optics and Quantum Information  
LP Low Pass  
OI Optical Isolator  
PBS Polarizing Beam Splitter  
PID Proportional-Integral-Derivative  
PM Polarization-Maintaining  
PMT Photo-Multiplier Tube  
PSD Power Spectral Density  
RAM Residual Amplitude Modulation  
RF Radio Frequency  
RMS Root Mean Square  
SciNet Scalable Ion Trap Network  
SLS Stable Laser Systems  
SRS Stanford Research Systems  
S/N Signal/Noise  
TEM Transversal Electro-Magnetic  
Ti:Sa Titanium-Sapphire  
QFC Quantum Frequency Conversion  
ULE Ultra-Low Expansion glass

# 1. Introduction

Quantum information science is a field of research that has experienced rapid growth in recent years. The interest in building devices based on the generation and manipulation of quantum information encoded in quantum mechanical two-level systems (qubits), stems from the possibilities provided by such systems, in terms of computational speedup over classical computers [1], fundamentally secure communication [2] and enhancement in measurement precision [3]. Small-scale quantum systems are already being used successfully to implement few-qubit algorithms [4] and perform quantum simulations [5]. However, for such quantum processors to be able to constitute an advantage over classical computing devices, quantum system sizes in the lab need to be scaled up. This has proven to be challenging due to e.g. decoherence effects [6], which increase with the system size.

In classical information processing the connection of computers via a network allows for the shared use of computational resources. Similarly, being able to transfer quantum information from one quantum computer to another provides the possibility of distributed quantum computing [7]. By connecting multiple smaller-scale quantum processors in a quantum network some scalability-related problems can be circumvented. Another application for quantum networks is in quantum communication and cryptography. Quantum key distribution protocols allow for fundamentally secure communication [8] across a quantum network. Network nodes can act as quantum repeater stations, enabling the distribution of quantum information over long distances [9].

At the University of Innsbruck and the Institute for Quantum Optics and Quantum Information (IQOQI), a three-node quantum network is being built at the moment, in the course of the SciNet (Scalable Ion Trap Network) project. Here, the network nodes consist of cavity-enhanced trapped  $^{40}\text{Ca}^+$  ion systems. Over the past years, trapped ions have proven to be a promising candidate in quantum information experiments, due to the high level of control that is possible over them in the lab [10]. In combination with an optical cavity around the trapped ion, it is possible to realize an interface which maps the quantum information stored in an ion qubit onto a photon qubit, that can then be distributed across a quantum network [11]. Nodes A and B of the SciNet network are located in the experimental physics university building: Node A consists of a well-established trapped-ion cavity setup, which has been under vacuum for many years [12] [13]. State mapping from an ion to a photon qubit [14] as well as the generation of entanglement between an ion qubit and photon qubit [15] has been successfully demonstrated with this setup. Node B differs from node A in the fact that the node B cavity is fiber-integrated, which allows for small mode volumes. Node C, which has a similar design to the node A system but cavity mirror parameters optimized for quantum networking, is being set up from scratch in the IQOQI building. A 400 m underground fiber link allows this node to be connected to nodes A and B in the university building. Since one problem of the distribution of

## 1. Introduction

quantum information over long distances is photon loss in optical fibers, the team at node C also investigates quantum frequency conversion (QFC) to change the wavelength of photons emitted by trapped ions to the telecom C band at 1550 nm, which is absorbed significantly less in optical fibers [16].

This master's thesis was carried out at Node C in the IQOQI building. The topic of the thesis is related to the aforementioned ion-photon interface: One of the keys to create a quantum network based on trapped-ion nodes is to implement an interface, in which the quantum information encoded in an ion qubit can be mapped onto a photon qubit. In our setup, this interface is based on a cavity-mediated Raman process involving three different electronic states of a trapped ion. One arm of this Raman transition is driven by a laser field, whereas the other arm is driven by coupling to the vacuum field of an optical cavity around the ion. This cavity-mediated Raman process has to be frequency-stabilized via laser locking. A "transfer lock" scheme is used to implement this frequency-stabilization, which requires two lasers to be locked to an external reference-cavity. One of these lasers will drive one arm of the Raman transition, whereas the other laser will be used as a stable reference to lock the length of the optical cavity around the ion. In the course of this master's thesis, the two laser systems, which will be used for the transfer lock at Node C, were stabilized to an external intrinsically stable reference-cavity. This work was carried out while node C was still under construction. Specifically, at the time of writing this thesis, the cavity around the ion is still missing but our ion trap has already been put in vacuum. As a result, it was not possible to test the transfer lock on a cavity-enhanced trapped-ion system in vacuum. However, a test setup was built, where a cavity was locked in air, using one of the stabilized laser systems as a reference.

The layout of this thesis is now presented. The next chapter (chapter 2) contains three parts. First, a brief general introduction on quantum networks is provided, followed by a focus on trapped-ion based networks. Second, theory on the interaction between atoms and light is presented, which allows for the understanding of the dynamics of the cavity-mediated Raman process in a cavity-enhanced trapped-ion system. Third, two basic quantum network protocols are explained, based on the cavity-mediated Raman process. Chapter 3 presents the relevant theoretical and experimental concepts on lasers and laser stabilization. Specifically, a scheme to lock a laser to a cavity as a frequency reference (and vice versa) is introduced, as well as linewidth estimation techniques, which will be applied in the experimental chapters 6 and 7. In chapter 4, our approach to frequency-stabilize the cavity-mediated Raman process (the transfer lock scheme) is given along with our experimental goals. Chapters 5, 6 and 7 present the experimental achievements of this thesis. Chapter 5 is about the experimental setup of the transfer lock, specifically the reference-cavity and vacuum chamber assembly, as well as the optical and electronic setup. The reference-cavity is the centerpiece of the transfer lock. It was not only coated to be used for the transfer lock at 785 nm and 786 nm, but additionally to serve another purpose in our system: to lock a laser on the  $^{40}\text{Ca}^+$  qubit transition at 729 nm. In chapter 6, the frequency-stability of two laser systems, locked to the reference-cavity, is investigated via frequency beat measurements with a frequency comb and a narrow reference laser. Here, the key results of this thesis, i.e. the locked laser linewidths and drift rates, are presented. In chapter 7, the stabilized laser systems are applied to lock a test-cavity in air and manipulate a trapped  $^{40}\text{Ca}^+$  ion on the 729 nm optical qubit transition.

# 2. Quantum Networks

## 2.1. Basic Principles of Quantum Networks

Quantum networks are important tools in quantum information science, allowing for the distribution of quantum information between physically separated quantum computers. Since quantum information is encoded in the state of a quantum mechanical e.g. two-level system (quantum bit, qubit), its distribution is fundamentally different and more complex than classical information distribution. In this section, the building blocks of quantum networks, key concepts of the distribution of quantum information and state of the art developments in the field are briefly presented.

### 2.1.1. Theoretical Concepts

#### Encoding of Quantum Information

The basic unit of classical information is the bit, which has the two possible states 0 and 1. In analogy, a qubit is the basic unit of quantum information [17]. Even though there are also only two possible outcomes when a qubit is measured, e.g.  $|0\rangle$  and  $|1\rangle$  when performing a projective measurement in the logical basis, the state of a qubit  $|\Psi\rangle$  can also be in a superposition of both, which can be represented mathematically as

$$|\Psi\rangle = \alpha|0\rangle + \beta|1\rangle = \begin{pmatrix} \alpha \\ \beta \end{pmatrix}. \quad (2.1)$$

If the state of the qubit can be described by a linear combination of the orthonormal basis states  $|0\rangle = \begin{pmatrix} 1 \\ 0 \end{pmatrix}$  and  $|1\rangle = \begin{pmatrix} 0 \\ 1 \end{pmatrix}$ , as in eq. 2.1, the qubit is said to be in a pure state.

For every ‘Ket’-vector  $|\Psi\rangle$  there exists a ‘Bra’-vector  $\langle\Psi| = (\alpha^*, \beta^*)$ , where  $*$  denotes the complex conjugate. The complex numbers  $\alpha$  and  $\beta$  represent probability amplitudes, where the probability of measuring the qubit to be in state  $|0\rangle$  ( $|1\rangle$ ) is given by  $|\alpha|^2$  ( $|\beta|^2$ ). Since the probabilities of the qubit being in either of the two basis states have to add up to one it follows that  $|\alpha|^2 + |\beta|^2 = 1$ . In the lab, the values of  $|\alpha|^2$  and  $|\beta|^2$  can be determined by preparing and measuring the same state many times.

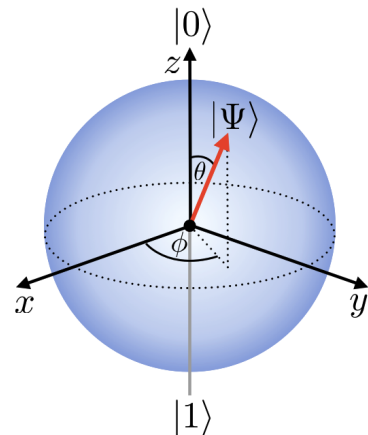


**Figure 2.1.:** The Bloch sphere: The quantum state of a single qubit can be described by its coordinates, i.e. projections onto the x, y and z-axis.

## 2. Quantum Networks

The Bloch sphere, which is shown in figure 2.1, is a convenient visualization of the possible states of a single qubit. Any pure state can be represented by a point on the surface of this unit sphere with polar coordinates (angles)  $\theta$  and  $\phi$ , allowing eq. 2.1 to be rewritten as

$$|\Psi\rangle = e^{i\gamma} (\cos(\theta/2) |0\rangle + e^{i\phi} \sin(\theta/2) |1\rangle). \quad (2.2)$$

Here,  $e^{i\gamma}$  is a global phase factor which has no observable effect and is usually ignored. In figure 2.1, the north and south poles of the sphere correspond to the logical basis states  $|0\rangle$  and  $|1\rangle$  and states that lie in the equatorial plane correspond to equal superpositions of those basis states.

The state of a qubit can also be represented as a density matrix [17]

$$\rho = \sum_i p_i |\Psi_i\rangle \langle \Psi_i| \quad (2.3)$$

where  $|\Psi_i\rangle$  are the possible states the system can be in with respective probabilities  $p_i$ . Choosing  $\{|\phi_m\rangle\}$  as an orthonormal basis, the elements of the density matrix can be written as

$$\rho_{mn} = \sum_i p_i \langle \phi_m | \Psi_i \rangle \langle \Psi_i | \phi_n \rangle = \langle \phi_m | \rho | \phi_n \rangle. \quad (2.4)$$

The density matrix is usually presented in the logical basis, where the states  $|\phi_m\rangle$  are the logical states of the qubit. In this case, the diagonal elements of the density matrix correspond to the state populations. The off-diagonal elements are called coherences and provide information about the phase relationship between the populations. The density matrix allows for the description of quantum states which are not pure states, i.e. they cannot be described as a single state vector but only as a statistical ensemble of different state vectors, each emerging with probability  $p_i$ . Such quantum states are called mixed states.

### Distribution of Quantum Information

The key concept of quantum information distribution is the transfer of a quantum state  $|\Psi\rangle$  across a network, while preserving the quantum superposition. To physically implement a quantum network, suitable nodes, interfaces and channels are required [18]. A *node* is a device in which quantum information can be generated, processed and stored. The quantum information encoded in “stationary” qubits at one node has to be mapped onto “flying” qubits via an appropriate *interface* and then transferred via a quantum *channel* to another node. As a result, the individual quantum processors can communicate with each other over the channel. Quantum information can then be distributed in two ways: First, the quantum state can be directly transferred from one node to another. Second, entanglement between nodes can first be generated to act as a resource for the teleportation of a quantum state across the network [19].

### 2.1.2. State of the Art in Quantum Network Experiments

#### Nodes

Quantum systems such as atoms, superconducting qubits, quantum dots or nitrogen-vacancy centers can be used to encode stationary qubits [1] [20]. Quantum information can be stored in these systems for their respective coherence time, which is limited due to coupling to the environment. One of the most promising approaches to encoding a stationary qubit is based on the use of two long-lived internal, e.g. electronic, states of an atom. In terms of using atoms as quantum network nodes, there exist different schemes, based on single particles like neutral atoms [21] or trapped ions [22] [23], and other schemes based on ensembles of atoms [24]. In section 2.2, the use of trapped  $^{40}\text{Ca}^+$  ion nodes, is discussed.

#### Interfaces

Single atoms or ions can also act as single photon sources. Photons are ideally suited to distribute quantum information as they experience little interaction with one another and the environment. However, the implementation of an interface, which allows for the mapping of a quantum state stored in a stationary qubit onto a photon qubit, is challenging. Schemes for single-photon generation, based on spontaneous emission from an excited state, have the disadvantage that the spatial uncertainty related to photon emission results in an inefficient photon collection. Also, in the case of a multi-level system such as an atom, there can be multiple decay channels available, which results in an additional spectral uncertainty. One approach for the deterministic generation of single photons into a well-defined spatial and spectral mode of the radiation field is based on a proposal by Cirac *et al.* [11]. Here, the coupling between an atom and a light field is greatly enhanced by placing the atom inside an optical cavity. The dipole coupling between the atom and the vacuum cavity field can be used to trigger the generation of a photon into the cavity mode. In section 2.4 a scheme for single-photon generation based on a three-level atom, specifically a trapped  $^{40}\text{Ca}^+$  ion, inside a cavity is discussed. Such a system acts as a coherent light-matter interface, where the quantum state of the atom can be deterministically mapped onto the emitted photon. Trapped ions are well-suited systems for the realization of such an interface as the ion's position within the cavity standing wave field can be controlled with very high precision [25].

#### Links

In order to interconnect nodes and distribute information in a quantum network via photons, a free-space link, e.g via satellites, can be used, which has very recently been demonstrated experimentally [26]. However, it is often more convenient to use optical fibers as quantum channels, due to a higher flexibility in terms of the position of the nodes. One problem of fiber networks is that the absorption in fibers can be large for optical photons. Quantum frequency conversion (QFC) provides the possibility to convert the wavelength of a photon to a wavelength, e.g. in the infrared IR-B regime, which is absorbed significantly less in optical fibers and thus allows for the distribution of

## 2. Quantum Networks

quantum information over hundreds of kilometers [16] [27]. An additional benefit of QFC is that different kinds of quantum systems, which emit and absorb photons at specific and different wavelengths, can be connected in a hybrid quantum network.

### Protocols

Basic protocols for the distribution of quantum information across a quantum network are presented in section 2.5 for quantum networks based on trapped-ion nodes. These schemes enable state mapping between stationary and flying qubits, and thus the direct state transfer, as well as the generation of entanglement between remote nodes.

## 2.2. Trapped Calcium Ions as Network Nodes

Any approximation of a two-level quantum system can be employed to encode a physical qubit. A multi-level quantum system can be used in the case that two states can be successfully decoupled from the rest, which is often the case for the electronic levels of an atom. The electronic levels are non-uniformly spaced and addressable individually with e.g. narrow linewidth lasers. A good choice for a qubit has proven to be two long-lived states of the single outer valence electron of a singularly ionized alkaline-earth atom. In Innsbruck, and several other groups around the world,  $^{40}\text{Ca}^+$  ions confined in a linear Paul trap are employed as qubits, which is one of the leading ionic species in quantum information science [28] [29] [30]. In the lab, such trapped-ion systems are among the most precisely controllable quantum systems available. Trapped-ion qubits exhibit long coherence and storage times, are addressable individually due to their spacing of a few  $\mu\text{m}$  in the trap, their quantum state can be detected efficiently via electron shelving and a toolbox of universal gate operations is available for their manipulation [31]. They are also single-photon sources, which makes them a suitable choice for a quantum network node [32].

### 2.2.1. Atomic Level Scheme

The electronic states of an atom are described via the notation  $n^{2s+1}l_j$  where  $n$  is the principal quantum number,  $s$  is the absolute value of the spin of the electron,  $l$  is the orbital angular momentum and  $j = |l \pm s|$ . Figure 2.2 provides an overview of the electronic levels of  $^{40}\text{Ca}^+$ , used in experiments in Innsbruck. In ion trap experiments a magnetic field of a few Gauss is typically applied to lift the degeneracy of the Zeeman manifold. Therefore, the magnetic quantum number  $m_j$  has to be considered as well, which is not shown in figure 2.2.

An optical qubit is usually encoded in the  $4^2\text{S}_{1/2}$  ( $|1\rangle$ ) ground state and the  $3^2\text{D}_{5/2}$  ( $|0\rangle$ ) metastable excited state which has a lifetime of  $\tau = 1.168\text{ s}$  [33]. The long lifetime of the excited state makes this qubit convenient for storing and processing quantum information as the time it takes to perform gate operations with established methods (typically in the range of 10 to 100  $\mu\text{s}$ ) is significantly shorter than the lifetime of the excited state [31].

## 2. Quantum Networks

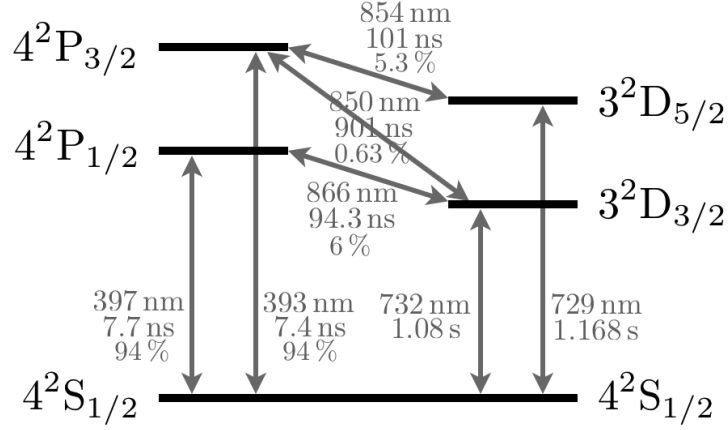


**Figure 2.2.:** Electronic levels of  $^{40}\text{Ca}^+$  used in experiments in Innsbruck [31]: A stationary qubit is encoded in the  $4^2S_{1/2}$  ground state and the  $3^2D_{5/2}$  metastable excited state. State detection as well as Doppler cooling can be performed on the electric dipole transition  $4^2S_{1/2} \longleftrightarrow 4^2P_{1/2}$  with a repumper from  $3^2D_{3/2}$  to  $4^2P_{1/2}$ . Sideband cooling can be performed on the electric quadrupole transition  $4^2S_{1/2} \longleftrightarrow 3^2D_{5/2}$ . The gray numbers next to the gray arrows, which represent the transitions, denote the energy separation of the states in units of wavelength (top), excited state lifetime (middle) and branching ratio, i.e. the fraction of decays via the transition with respect to all possible decay channels (bottom).

### 2.2.2. Trapping and Cooling

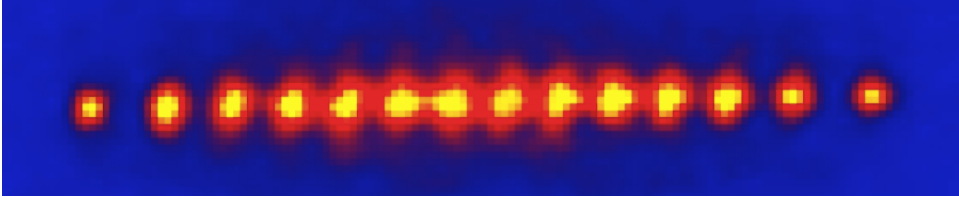


**Figure 2.3.:** 14-ion crystal in a linear Paul trap: The  $^{40}\text{Ca}^+$  ions are confined in the axial (from the left and right side) and radial direction. The distance between the ions is about  $4 \mu\text{m}$ . Image taken from [31].

To confine the ions in a linear Paul trap [34], thermal calcium vapour is sprayed into the trap from a hot oven. Then the atoms are charged in a two-stage photo-ionization process. One laser has a suitable frequency to excite an electron of the desired calcium isotope and a second laser takes the electron to the continuum. Doppler laser cooling [35], which acts to slow down the ions via the scattering of off-resonant photons, is performed on the dipole transition from the  $4^2S_{1/2}$  to the short-lived  $4^2P_{1/2}$  state (lifetime  $\tau = 7 \text{ ns}$  [36]). In order to avoid the accumulation of population in the long-lived  $3^2D_{3/2}$  state, a laser on the  $4^2P_{1/2} \longleftrightarrow 3^2D_{3/2}$  transition acts as a repumper. Under the influence of Doppler cooling, the charged ions align in the trap, where they are confined in the radial direction via an RF field oscillating at several 10 MHz. According to Earnshaw's theorem [37], it is not possible to confine a charged particle in all three spatial directions using only static electric fields. However, an average confining force, here in the radial direction, can be achieved by using a time-varying electric field, oscillating at a rate faster than

## 2. Quantum Networks

the time it would take the ion to escape the trap. Additional confinement in the axial direction is achieved via a constant electric field. The resulting effective three-dimensional confinement corresponds to (approximate) harmonic trapping potentials in three spatial directions.

A 14-ion string is shown in figure 2.3. Here, a fraction of the 397 nm photons emitted by the ions during Doppler cooling is detected with a CCD camera. The ions in the string share many harmonic modes of oscillation. Therefore the ionic qubit in the trap can be modelled as a two-level atom and three harmonic oscillators, corresponding to the three spatial directions.

### 2.2.3. Qubit State Readout

The  $4^2S_{1/2} \longleftrightarrow 4^2P_{1/2}$  transition at 397 nm is also used to measure the quantum state of the qubit. In the case that the qubit is in a superposition between  $4^2S_{1/2}$  and  $3^2D_{5/2}$ , turning on 397 nm light projects the qubit either into the  $4^2S_{1/2}$  or  $3^2D_{5/2}$  state. If the qubit is projected into the  $4^2S_{1/2}$  state, the electron is excited by the laser to  $4^2P_{1/2}$ , a short-lived state, from which it rapidly decays. Many photons are scattered which can be detected with a CCD camera, as shown in figure 2.3, or a photo-multiplier tube (PMT). In the case that the electron is projected into the  $3^2D_{5/2}$  state, it does not interact with the laser light and no light is scattered. This is known as the electron shelving method, and was first demonstrated for ions in [38] [39] [40].

## 2.3. Manipulation of the Electronic State of Trapped Ions With Lasers

As mentioned in the previous section, trapped ions can be manipulated via laser fields. For example, transitions between the electronic states of an ion at or around optical frequencies can be driven when a laser interacts with the ion for a certain amount of time. In this section, theory on the interaction between light and an atom is presented, mainly based on books by Crispin Gardiner and Peter Zoller [41] [24]. First, the interaction of a two-level atom with a classical driving field (laser) and the environment is discussed, which illustrates the coherent population transfer on the long-lived qubit transition and the effect of dissipative processes. The theory is then extended to three-level atoms, in which population can be coherently transferred between two long-lived ground states via off-resonant coupling with two classical driving fields to a short-lived excited state. This forms the basis for the following section 2.4, where the coupling of a trapped-ion qubit to a photon qubit, based on population transfer in a three-level atom, is presented.

### 2.3.1. Light-Atom Interaction in the Dipole Approximation

An electron with mass  $m$ , momentum  $\vec{p}$ , charge  $-e$  at location  $\vec{x}$ , which is bound to an atom's nucleus in a Coulomb potential  $V(\vec{x})$ , and which interacts with the electromagnetic

## 2. Quantum Networks

field can be described (in Coulomb gauge) by the Hamiltonian [41]

$$\hat{H} = \underbrace{\frac{1}{2m}(\vec{p} + e\vec{A}(\vec{x}))^2 + V(\vec{x})}_{\hat{H}_{\text{atom}} + \hat{H}_{\text{int}}} + \underbrace{\sum_k \hbar\omega_k(\hat{a}_k^\dagger\hat{a}_k + \frac{1}{2})}_{\hat{H}_{\text{light}}}. \quad (2.5)$$

The terms  $\hat{H}_{\text{atom}} + \hat{H}_{\text{int}}$  represent the Hamiltonian of the atom and the coupling to the electromagnetic field. According to classical electromagnetism and the Lagrangian formalism, the coupling to the electromagnetic field can be introduced by modifying the momentum by the vector potential  $\vec{A}$  which is related to the electric field  $\vec{E}$  of the light [42]. The last term  $\hat{H}_{\text{light}}$  of the Hamiltonian in eq. 2.5 represents the quantized radiation field, where light is described as a sum of harmonic oscillators, the modes  $k$  of the radiation field with respective frequencies  $\omega_k$ . The creation (annihilation) operator  $\hat{a}_k^\dagger$  ( $\hat{a}_k$ ) represents the creation (destruction) of a photon in a mode  $k$ . To simplify the interaction between the light field and atom, the long wavelength approximation can be applied, which is valid for the optical regime of the electromagnetic spectrum, where the wavelength of the light is much larger than the spatial extent of the atom. As a result, the vector potential  $\vec{A}(\vec{x})$  is replaced by its value at the origin  $\vec{A}(\vec{0})$ . Performing a unitary operation, which is basically just a change of basis,

$$\hat{H}' = e^{-\frac{i}{\hbar}\vec{A}(0)\vec{d}}\hat{H}e^{+\frac{i}{\hbar}\vec{A}(0)\vec{d}} \quad (2.6)$$

where the dipole operator

$$\vec{d} = -e\vec{x} \quad (2.7)$$

is introduced, allows the interaction part of the Hamiltonian to be written as

$$H_{\text{int}} = -\vec{d} \cdot \vec{E}(0) \quad (2.8)$$

which is the well-known dipole interaction Hamiltonian [42].

### Two-Level Approximation

The energy eigenstates of the atom can be written in Ket-notation  $|i\rangle$  where  $E_i = \hbar\omega_i$  is the corresponding energy eigenvalue. The Hamiltonian for the atom can then be written as [41]

$$\hat{H}_{\text{atom}} = \sum_i E_i |i\rangle\langle i| \quad (2.9)$$

and similarly, the dipole operator can be written as

$$-\vec{d} = \sum_{f,i} \vec{d}_{if} |f\rangle\langle i|. \quad (2.10)$$

As discussed previously, in the case of trapped ions manipulated with lasers, such a multi-level system can be reduced to a two-level system, due to the non-uniform spacing of the electronic energy levels and the ability to address two levels individually. Only the ground state  $|g\rangle$  and excited state  $|e\rangle$

$$|g\rangle = \begin{pmatrix} 0 \\ 1 \end{pmatrix}, |e\rangle = \begin{pmatrix} 1 \\ 0 \end{pmatrix} \quad (2.11)$$

## 2. Quantum Networks

are considered with respective energy eigenvalues  $E_g = \hbar\omega_g$  and  $E_e = \hbar\omega_e$ . The Hamiltonian for the atom can therefore be written as

$$\hat{H}_{\text{atom}} = \hbar\omega_g|g\rangle\langle g| + \hbar\omega_e|e\rangle\langle e| = \begin{pmatrix} \hbar\omega_e & 0 \\ 0 & \hbar\omega_g \end{pmatrix}. \quad (2.12)$$

The dipole operator, which describes the coupling between the ground and excited state via a dipole transition, can be expressed as

$$-\vec{d} = \vec{d}_{eg}|g\rangle\langle e| + \vec{d}_{ge}|e\rangle\langle g| = \vec{d}_{eg}\hat{\sigma}_- + \vec{d}_{ge}\hat{\sigma}_+ = \begin{pmatrix} 0 & \vec{d}_{eg} \\ \vec{d}_{ge} & 0 \end{pmatrix} \quad (2.13)$$

where the operator  $\hat{\sigma}_- = |g\rangle\langle e|$  ( $\hat{\sigma}_+ = |e\rangle\langle g|$ ) de-excites (excites) the atom. Considering that  $\vec{d}_{eg} = \vec{d}_{ge}^*$  the interaction Hamiltonian can be written as

$$\hat{H}_{\text{int}} = \begin{pmatrix} 0 & \vec{d}_{eg} \cdot \vec{E}(0) \\ \vec{d}_{eg}^* \cdot \vec{E}(0) & 0 \end{pmatrix}. \quad (2.14)$$

Note, that the form of this equation is also valid for higher order moments, e.g. when coupling the ground and excited state via an electric quadrupole transition. Here, the interaction Hamiltonian takes the form  $\vec{q}_{eg} \cdot \nabla \vec{E}$ , i.e. the gradient of the electric field of the light  $\nabla \vec{E}$  couples to the quadrupole moment  $\vec{q}_{eg}$  [43]. The following theory is based on dipole transitions but is also valid for e.g. quadrupole transition, when considering the respective coupling terms.

### 2.3.2. Coherent Manipulation and Dissipative Processes

#### Semiclassical Approximation: Interaction Between a Strong Classical Driving Field and a Two-Level Atom

The light field of a laser can be described by a coherent state with many photons [24]. Adding or subtracting a single photon by applying  $\hat{a}$  or  $\hat{a}^\dagger$  basically does not change the state of the light field. Therefore, it is sufficient to treat the interaction between a laser field and atom semiclassically. Since in that case there is no Hamiltonian associated with the classical light field, the total Hamiltonian describing the situation consists of the Hamiltonian for the atom and the coupling between atom and light field:

$$\hat{H} = \begin{pmatrix} \hbar\omega_e & \vec{d}_{eg} \cdot \vec{E}(0) \\ \vec{d}_{eg}^* \cdot \vec{E}(0) & \hbar\omega_g \end{pmatrix} \quad (2.15)$$

Considering a monochromatic electromagnetic field, the coupling terms can be written as [41]

$$\vec{d}_{eg} \cdot \vec{E}(0, t) = 2i\mathcal{E} \cos(\omega t) \quad (2.16)$$

where  $\omega$  is the frequency of the light. The Hamiltonian can be transformed into a rotating reference frame (interaction picture), denoted by  $\sim$ , where the time dependence is absorbed in a unitary transformation:

$$\tilde{H} = \hbar \begin{pmatrix} -\Delta & -\frac{1}{2}\Omega \\ -\frac{1}{2}\Omega & 0 \end{pmatrix} \quad (2.17)$$

## 2. Quantum Networks

Only the evolution of the electronic state of the atom due to the interaction between the light field and atom is then considered. Terms in the Hamiltonian where the light field approximately co-rotates with the reference frame are kept while rapidly oscillating (at the sum of the atomic and light frequencies) terms can be neglected as they correspond to non-resonant processes [41]. In eq. 2.17,  $\Delta = \omega - \omega_{eg}$  is the detuning between laser frequency  $\omega$  and atomic transition frequency  $\omega_{eg} = \omega_e - \omega_g$  and

$$\Omega = \frac{|2\mathcal{E}|}{\hbar} = \frac{|\vec{d}_{eg} \cdot \vec{E}|}{\hbar} \quad (2.18)$$

is the Rabi frequency, which quantifies the coupling strength between the atom and light field.

### Unitary Evolution and Spontaneous Decay

In the case that no information is lost to the environment, the dynamics of a quantum system, e.g. laser-driven dynamics on the long-lived qubit transition of an ion, can be described by unitary operations

$$\hat{U}(t) = e^{-\frac{i}{\hbar}\hat{H}t} \quad (2.19)$$

under a Hamiltonian  $\hat{H}^1$ . This is just the solution to the Schrödinger equation for a time-independent Hamiltonian. The time-evolved density matrix of the quantum system can then be written as

$$\rho(t) = \hat{U}(t)\rho(t=0)\hat{U}^\dagger(t). \quad (2.20)$$

However, a quantum system in the lab cannot be shielded from interaction with its environment, which can lead to unwanted dissipative processes. One important example, amplitude damping, describes an atom in the excited state coupling to the vacuum and undergoing spontaneous emission. Here, the excited state can decay to the ground state by emission of a single photon which carries away any information about the superposition state. All possible states get mapped onto the ground state and if the photon is not detected all quantum information is lost to the environment. Such a process is described by a non-unitary operation on the quantum system.

In general, the evolution of the quantum state of a system, which experiences coupling to its environment, can be expressed via a Master equation formalism. Such a Master equation describes the time evolution of all elements of the density matrix. The Master equation in Lindblad form [17] is given by

$$\frac{d\rho}{dt} = -\frac{i}{\hbar}[\hat{H}, \rho] + \sum_j (2\hat{L}_j\rho\hat{L}_j^\dagger - \hat{L}_j^\dagger\hat{L}_j\rho - \rho\hat{L}_j^\dagger\hat{L}_j) \quad (2.21)$$

where  $\hat{L}_j$  are Lindblad operators, which represent the coupling between the system and the environment.

The Master equation for a two-level atom interacting with a laser (unitary evolution) and the environment through spontaneous emission is given by

$$\frac{d\rho}{dt} = -\frac{i}{\hbar}[\hat{H}, \rho] + \frac{\Gamma}{2}(2\hat{\sigma}_-\rho\hat{\sigma}_+ - \hat{\sigma}_+\hat{\sigma}_-\rho - \rho\hat{\sigma}_+\hat{\sigma}_-) \quad (2.22)$$

---

<sup>1</sup>This is valid on timescales much shorter than the lifetime of the qubit and when using a laser with a coherence time much longer than these timescales.

## 2. Quantum Networks

where  $\sqrt{\Gamma/2}\hat{\sigma}_-$  is the appropriate Lindblad operator as it takes the atom from excited to ground state with spontaneous emission rate  $\Gamma$ .

The spontaneous emission rate can be described by Fermi's golden rule in the dipole approximation in free space and vacuum as [24]

$$\Gamma = \frac{\omega_{eg}^3 |\vec{d}_{eg}|^2}{3\pi\epsilon_0 \hbar c^3}. \quad (2.23)$$

The solutions to the Master equation in eq. 2.22 are the optical Bloch equations. They allow for the description of the unitary evolution of the system due to the driving field as well as the coupling to the environment, which can be expressed via damping terms. Using the Hamiltonian 2.17 in eq. 2.22 leads to the optical Bloch equations in a rotating reference frame:

$$\begin{pmatrix} \dot{\tilde{\rho}}_{ee} & \dot{\tilde{\rho}}_{eg} \\ \dot{\tilde{\rho}}_{ge} & \dot{\tilde{\rho}}_{gg} \end{pmatrix} = \begin{pmatrix} -\frac{i\Omega}{2}(\tilde{\rho}_{eg} - \tilde{\rho}_{ge}) - \Gamma\tilde{\rho}_{ee} & -\frac{i\Omega}{2}(\tilde{\rho}_{gg} - \tilde{\rho}_{ee}) + i\delta\tilde{\rho}_{eg} - \frac{\Gamma}{2}\tilde{\rho}_{eg} \\ -\frac{i\Omega}{2}(\tilde{\rho}_{ee} - \tilde{\rho}_{gg}) + i\delta\tilde{\rho}_{ge} - \frac{\Gamma}{2}\tilde{\rho}_{ge} & -\frac{i\Omega}{2}(\tilde{\rho}_{ge} - \tilde{\rho}_{eg}) + \Gamma\tilde{\rho}_{ee} \end{pmatrix} \quad (2.24)$$

Solving this system of coupled differential equations provides e.g. information about the evolution of the excited state population of the two-level atom. In the case that  $\Gamma = 0$ , i.e. spontaneous emission is neglected and only the unitary part of the time evolution is considered, Rabi oscillations [24] between the ground and excited state occur.

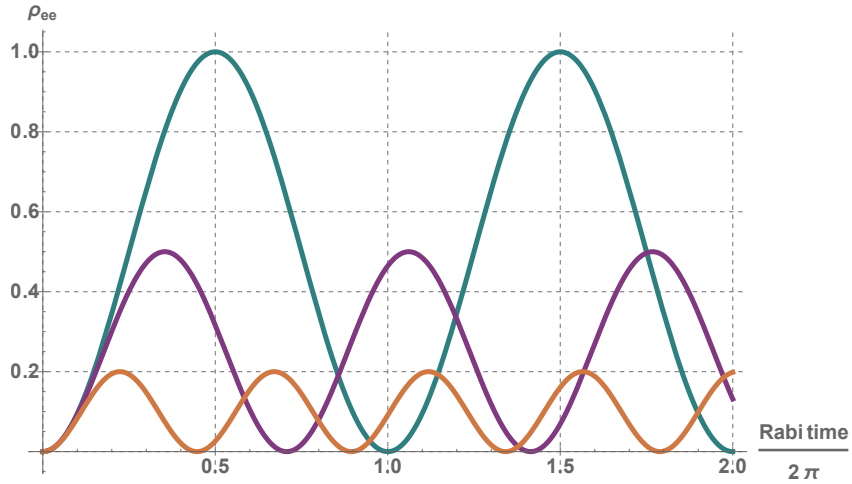


**Figure 2.4.:** Time evolution of the excited state population of a two-level atom as given by the optical Bloch equations without damping for  $\Delta = 0$  (green),  $\Delta = \Omega$  (purple) and  $\Delta = 2\Omega$  (orange). Here, the time axis is given in units of Rabi time ( $1/\Omega$ ).

Rabi oscillations for different detunings are shown in figure 2.4, where initially all population is in the ground state. In the case that the frequency of the laser is exactly on resonance with the atomic transition frequency, such that  $\Delta = 0$ , the frequency of these oscillations is given by the Rabi frequency  $\Omega$ . If the laser frequency is detuned from the transition frequency, the oscillation frequency increases. The effective Rabi frequency, with which the population of the excited state oscillates, is given by

$$\Omega_{\text{eff}} = \sqrt{\Omega^2 + \Delta^2}. \quad (2.25)$$

## 2. Quantum Networks

The maximum excitation probability decreases with detuning and is given by

$$P_{\max} = \frac{\Omega^2}{\Omega_{\text{eff}}^2}. \quad (2.26)$$

If  $\Gamma \neq 0$ , coupling to the environment will result in a damping of the Rabi oscillations, as shown in figure 2.5. For small decay rates, Rabi oscillations are still visible but on a long timescale, population cannot be moved between ground and excited state any more.

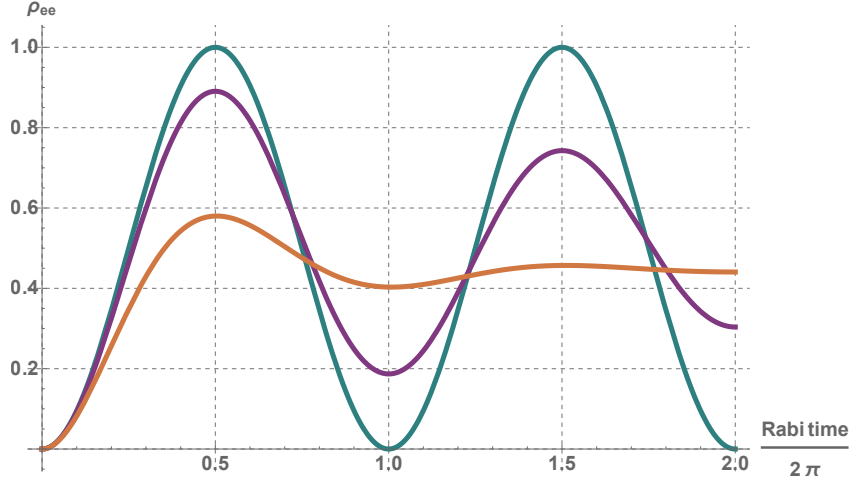


**Figure 2.5.:** Time evolution of the excited state population of a two-level atom as given by the optical Bloch equations for  $\Delta = 0$  with damping rate  $\Gamma = 0$  (green),  $\Gamma = 0.1\Omega$  (purple) and  $\Gamma = 0.5\Omega$  (orange).

### 2.3.3. Raman Transitions in a Three-Level Atom

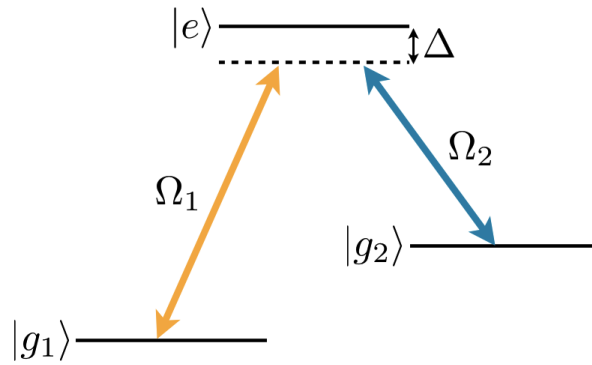


**Figure 2.6.:** Three-level  $\Lambda$ -type system:  $|g_1\rangle$  and  $|g_2\rangle$  represent two long-lived states, which are off-resonantly coupled (detuning  $\Delta$ ) with two driving fields with Rabi frequencies  $\Omega_1$  and  $\Omega_2$  via a short-lived excited state  $|e\rangle$ .

In section 2.4, the implementation of a deterministic single photon source based on a three-level atom will be presented. Therefore, first a theory extension to three-level atoms is provided. In a “ $\Lambda$ -type” three-level system, shown in figure 2.6, with two long-lived

## 2. Quantum Networks

ground states, a coherent transfer of population between the ground states is possible, by means of off-resonant coupling to a short-lived excited state, using two driving fields. In such a ‘‘Raman process’’, the off-resonant coupling allows population of the excited state and therefore spontaneous emission from that state to be suppressed. In the context of quantum networks, a Raman process can be used to coherently map quantum information from an atomic qubit to a photon qubit, by replacing one of the drive lasers with an optical cavity (section 2.4). Another important application of Raman processes is driving non-optical transitions, for which lasers are unavailable.

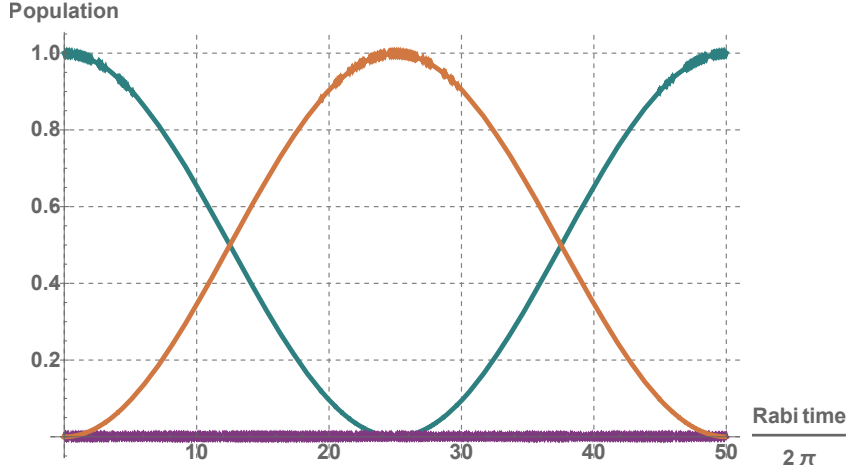


**Figure 2.7.:** Dynamics of the populations of a three-level system under the Hamiltonian 2.28: The population of  $|g_1\rangle$  (green),  $|g_2\rangle$  (orange) and  $|e\rangle$  (purple) is shown as a function of the Rabi time for  $\Omega_1 = \Omega_2$  and a detuning  $\Delta = 25\Omega_1$ .

Equivalent to the theory of a two-level atom interacting with a classical light field, a Hamiltonian for a three-level atom, with energy eigenstates

$$|g_1\rangle = \begin{pmatrix} 1 \\ 0 \\ 0 \end{pmatrix}, |e\rangle = \begin{pmatrix} 0 \\ 1 \\ 0 \end{pmatrix}, |g_2\rangle = \begin{pmatrix} 0 \\ 0 \\ 1 \end{pmatrix}, \quad (2.27)$$

interacting with two classical light fields can be derived in a rotating reference frame as

$$\tilde{H} = \begin{pmatrix} 0 & \frac{1}{2}\hbar\Omega_1 & 0 \\ \frac{1}{2}\hbar\Omega_1 & -\hbar\Delta & \frac{1}{2}\hbar\Omega_2 \\ 0 & \frac{1}{2}\hbar\Omega_2 & 0 \end{pmatrix}. \quad (2.28)$$

The two driving fields with coupling strengths  $\Omega_1$  and  $\Omega_2$  are detuned by  $\Delta$  from the excited state  $|e\rangle$ , which has a total spontaneous emission rate  $\Gamma$  taking into account the two possible decay channels in the three-level system. This Hamiltonian corresponds to a situation where the difference in the two driving frequencies is equal to the transition frequency between  $|g_1\rangle$  and  $|g_2\rangle$ <sup>2</sup>, as indicated in figure 2.6. In the case of large detunings, i.e.  $\Delta \gg \Omega_1, \Omega_2, \Gamma$ , the excited state can be adiabatically eliminated in the

<sup>2</sup>In reality, the energy shift of the atomic levels due to the AC Stark effect induced by off-resonant driving has to be considered.

## 2. Quantum Networks

calculation and an effective two-level system is obtained, where the population of  $|g_1\rangle$  and  $|g_2\rangle$  coherently oscillates with an effective Rabi frequency [13]

$$\Omega_{\text{eff}} = \frac{\Omega_1\Omega_2}{2\Delta} \quad (2.29)$$

which is shown in figure 2.7.

The effective decay rate of the excited state can be approximated by [12]

$$\Gamma_{\text{eff}} \approx \frac{\Omega_1^2}{4\Delta^2}\Gamma. \quad (2.30)$$

In summary, the effective Rabi frequency decreases with increasing detuning as  $\Omega_1/\Delta$ , whereas the effective decay rate decreases as  $(\Omega_1/\Delta)^2$ . It is therefore always possible to achieve an effective Rabi frequency which is larger than the rate of spontaneous decay for large detunings, even if the Rabi frequency  $\Omega_2$  of the second laser field is small.

## 2.4. Coupling a Trapped-Ion Qubit to a Photon Qubit

The theory on three-level atoms from the previous section lays the groundwork for the theory on the implementation of a light-matter interface for quantum networking, which is presented in this section. In contrast to before, where the two ground states of a three-level atom were coupled with two drive lasers, here one of the lasers is replaced by an optical cavity.

An optical cavity or optical resonator is an arrangement of mirrors, where light can be confined and stored. The simplest cavity consists of two mirrors, which reflect light back and forth such that a standing wave forms inside. Only the longitudinal modes of the cavity, which satisfy the resonance condition

$$n\lambda = 2L, \quad (2.31)$$

where  $n$  is an integer,  $\lambda$  is the wavelength of the light and  $2L$  is the optical round trip path length, can constructively interfere inside the cavity. In this section, first the theory of cavity quantum electrodynamics (cavity QED) is briefly introduced. This is followed by theory on the cavity-mediated Raman process, which allows for the coupling of a trapped-ion qubit inside an optical cavity to a photon qubit.

### 2.4.1. Cavity Quantum Electrodynamics

To enhance the coupling between a mode of the electromagnetic field and a two-level atom, the atom can be placed inside an optical cavity. The interaction of the atom and light inside the cavity is described by the theory of cavity QED, where the light field now has to be treated quantum mechanically, as presented in eq. 2.5. In the following, the interaction between an atom inside a cavity and a single cavity mode is considered. Here, the dynamics of the atom are only affected by a single mode, which is close to the atomic transition frequency. A single mode radiation field can be described by its electric field

$$\vec{E}(\vec{x}) = i(\vec{\mathcal{F}}(\vec{x})\hat{a} + \vec{\mathcal{F}}^*(\vec{x})\hat{a}^\dagger) \quad (2.32)$$

## 2. Quantum Networks

where  $\vec{\mathcal{F}}(\vec{x})$  is the appropriate spatial mode function for the cavity [24]. From the interaction Hamiltonian in eq. 2.14<sup>3</sup>, and the expression for the quantized electric field from eq. 2.32, one can derive a single-mode interaction Hamiltonian

$$\hat{H}_{\text{int}} = i(\vec{d}_{eg}\hat{\sigma}_- + +\vec{d}_{eg}^*\hat{\sigma}_+)(\vec{\mathcal{F}}\hat{a} + \vec{\mathcal{F}}^*\hat{a}^\dagger). \quad (2.33)$$

An important approximation, which can be made, is the rotating wave approximation, where terms like  $\sigma_+\hat{a}^\dagger$  and  $\sigma_-\hat{a}$  are omitted. Considering that the photon energy is close to the energy between the electronic levels, such terms describe non-resonant processes, which are suppressed. Mathematically, the rotating wave approximation (RWA) can be justified by transforming into the interaction picture, where these exact terms oscillate very fast, at the sum of the atomic and light frequencies, such that the average effect vanishes [24]. The single mode interaction Hamiltonian in rotating wave approximation can then be expressed as

$$\hat{H}_{\text{int}} = \hbar g(\hat{\sigma}_+\hat{a} + \hat{\sigma}_-\hat{a}^\dagger) \quad (2.34)$$

where

$$g = \frac{|\vec{d}_{eg} \cdot \vec{\mathcal{F}}|}{\hbar} \quad (2.35)$$

quantifies the coupling strength. The complete Hamiltonian, including the atomic part and single-mode radiation field is given by the Jaynes-Cummings Hamiltonian [44]

$$\hat{H}_{\text{JC}} = \hbar\omega_g|g\rangle\langle g| + \hbar\omega_e|e\rangle\langle e| + \hbar\omega\hat{a}^\dagger\hat{a} + \hbar g(\hat{a}^\dagger\hat{\sigma}_- + \hat{a}\hat{\sigma}_+). \quad (2.36)$$

The Hilbert space has the basis states  $|g, n\rangle$  and  $|e, n\rangle$ , which describe the state of the atom and number of photons in the cavity mode. The states of the light field correspond to the equidistantly spaced energy levels of a harmonic oscillator, where the lowest energy level corresponds to the vacuum state, i.e. no photons in the cavity. The Jaynes-Cummings Hamiltonian can be diagonalized in the basis of the dressed states, which for  $n = 1$  photon in the cavity take the form

$$\begin{aligned} |+, 1\rangle &= +\cos(\theta/2)|e, 0\rangle + \sin(\theta/2)|g, 1\rangle \\ |-, 1\rangle &= -\sin(\theta/2)|e, 0\rangle + \cos(\theta/2)|g, 1\rangle \end{aligned} \quad (2.37)$$

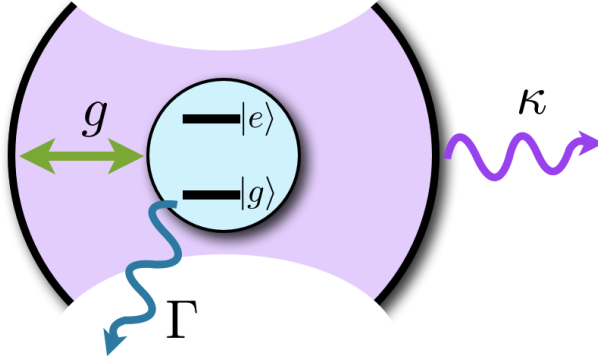
where

$$\tan(\theta) = -\frac{2g}{\delta} = -\frac{\Omega_{\text{vac}}}{\delta} \quad (2.38)$$

with the vacuum Rabi frequency  $\Omega_{\text{vac}}$  and detuning between cavity and atom  $\delta = \omega - \omega_{eg}$ . If  $\delta = 0$ , the eigenstates are  $|\pm, 1\rangle = \frac{1}{\sqrt{2}}(|g, 1\rangle \pm |e, 0\rangle)$  and the system undergoes Rabi oscillations with a frequency  $\Omega_{\text{vac}}$  between the basis states, when initially prepared in either one of the basis states.

---

<sup>3</sup>Here, the position dependence of the electric field should not be omitted as the coupling depends strongly on the ion's position within the cavity. Maximum coupling is achieved when the ion is very cold and at an antinode in the focus of the cavity. In the following,  $\vec{\mathcal{F}}$  describes the value of the mode function at which the coupling is maximized.

**Dissipation**


**Figure 2.8.:** Dynamics of an atom-cavity system:  $g$  represents the coupling between the two-level atom and cavity,  $\Gamma$  is the decay rate of the atom and  $\kappa$  corresponds to the cavity decay rate.

The interaction of an atom-cavity system with the environment is described via two processes: First, the atom can decay by emission of a photon into a field mode not confined by the cavity. Second, the electromagnetic field mode inside the cavity can couple to the input and output fields through a partially transmissive cavity mirror. These two processes are described by the Lindblad operators  $\sqrt{\Gamma/2}\hat{\sigma}_-$  and  $\sqrt{\kappa/2}\hat{a}$ , respectively, where  $\kappa$  corresponds to the rate of photon decay out of the cavity. Therefore, there exist three parameters which determine the dynamics of such an atom-cavity system, as illustrated in figure 2.8: The coupling strength  $g$  between atom and cavity and the decay rates  $\Gamma$  and  $\kappa$ . The case  $g \gg \Gamma, \kappa$  describes the strong coupling regime, where coherent evolution is dominant over dissipative effects. In quantum network experiments it is important to find a balance between these parameters, such that photons can both be created and sent out of the cavity at a convenient rate. The cavity decay rate depends on the properties of the mirrors via [45]

$$\kappa = \frac{c\pi}{FL} \quad (2.39)$$

where  $c$  is the speed of light,  $F$  is the Finesse, a parameter related to the total round trip losses in a cavity, and  $L$  is the optical path length of the cavity. The atom-cavity coupling constant  $g$  is inversely proportional to the mode volume in a cavity  $L\omega_0^2\pi/4$ , where  $\omega_0$  is the waist radius, the smallest beam radius at the focus of the cavity mode. The maximum coupling constant can be calculated as [25]

$$g = \sqrt{\frac{c\Gamma\lambda^2}{\pi^2 L\omega_0^2}}. \quad (2.40)$$

If the mode volume and therefore the cavity length decreases, the coupling strength between atom and cavity increases. In ion-trap experiments it is difficult to achieve strong coupling as reducing the cavity length too much can result in the dielectric cavity mirrors perturbing the trapping potential.

## 2.4.2. Cavity-Mediated Raman Process

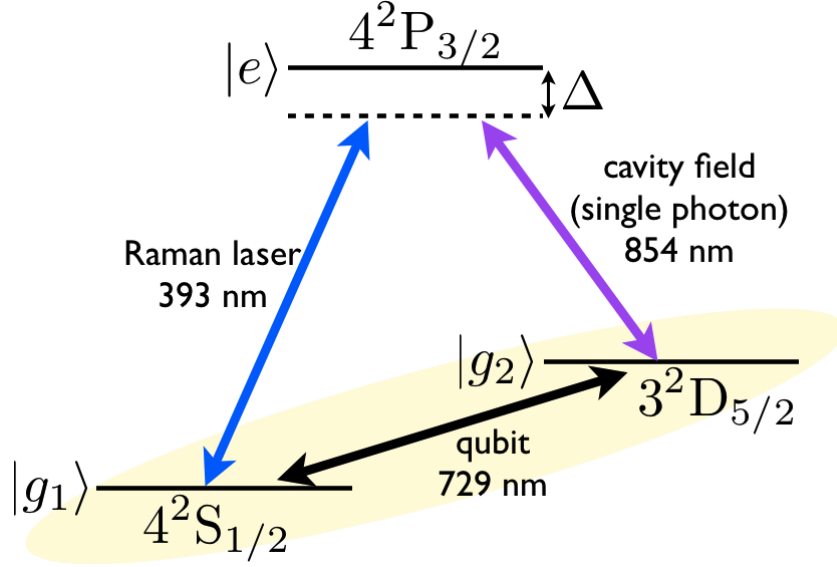


**Figure 2.9.:** Three electronic states of  $^{40}\text{Ca}^+$  which are involved in the cavity-mediated Raman process: A 393 nm drive laser off-resonantly couples the  $4^2\text{S}_{1/2}$  and  $4^2\text{P}_{3/2}$  levels and the ion off-resonantly couples to the cavity on the 854 nm transition, connecting the states  $4^2\text{P}_{3/2}$  and  $3^2\text{D}_{5/2}$ , which triggers the generation of a photon. The two long-lived states  $4^2\text{S}_{1/2}$  and  $3^2\text{D}_{5/2}$  are the basis states of the 729 nm optical qubit (stationary qubit).

A three-level atom in a  $\Lambda$ -configuration placed inside an optical cavity provides a possibility for the implementation of a coherent light-matter interface for quantum networking. In order to realize a photon link between trapped-ion nodes, a deterministic single photon generation process is desired. This can be achieved via a cavity-mediated Raman process, where an optical cavity provides coherent coupling such that a photon is emitted into a spatially and spectrally well-defined output mode.

The process is similar to the Raman process discussed in section 2.3.3, where  $|g_1\rangle$  and  $|g_2\rangle$  are two long-lived states of a three-level  $\Lambda$ -type system, the stationary qubit basis states, and  $|e\rangle$  is a short-lived excited state. In contrast to before however, here only one arm of the Raman transition from  $|g_1\rangle$  to  $|e\rangle$  is off-resonantly driven by a laser with Rabi frequency  $\Omega_1$ . The other arm of the transition is off-resonantly driven by coupling to the vacuum field of the cavity with coupling constant  $g$ . As before, the excited state can be adiabatically eliminated for a large detuning  $\Delta \gg \Omega_1, g$ . If the difference in driving frequencies is equal to the transition frequency between  $|g_1\rangle$  and  $|g_2\rangle$  the dynamics of the cavity mediated Raman transition in a rotating reference frame can be described by a Jaynes-Cummings type interaction Hamiltonian

$$\tilde{H} = \hbar\Omega_{\text{eff}}(|g_1\rangle\langle g_2| + |g_2\rangle\langle g_1|\hat{a}^\dagger). \quad (2.41)$$

Population is directly transferred between  $|g_1\rangle$  and  $|g_2\rangle$  with an effective Rabi frequency

$$\Omega_{\text{eff}} = \frac{g\Omega_1}{2\Delta} \quad (2.42)$$

## 2. Quantum Networks

in direct analogy to eq. 2.29, where the second laser field is now replaced by the atom-cavity coupling  $g$ . In the case that the electron is initially in state  $|g_1\rangle$ , the drive laser off-resonantly couples the states  $|g_1\rangle$  and  $|e\rangle$  and the atom couples to the cavity on the  $|e\rangle \longleftrightarrow |g_2\rangle$  transition, which triggers the generation of a photon, denoted by  $\hat{a}^\dagger$ , into the cavity mode ( $|g_1, 0\rangle \longrightarrow |g_2, 1\rangle$ ). In the case that the electron is initially in the  $|g_2\rangle$  state and there is no photon in the cavity<sup>4</sup>, it does not couple to the Raman laser and no photon emission is triggered. As before, the effective decay rate from the excited state  $|e\rangle$  is given by eq. 2.30. There are now two conditions for a coherent population transfer. First,  $\Omega_{\text{eff}} \gg \Gamma_{\text{eff}}$  to suppress spontaneous emission into modes not confined by the cavity, which can be achieved by increasing the detuning. Second,  $\Omega_{\text{eff}} > \kappa$  such that the transfer is complete before the photon completely leaves the cavity [25].

In  $^{40}\text{Ca}^+$ , a cavity-mediated Raman transition can be realized involving the  $4^2\text{S}_{1/2}$ ,  $4^2\text{P}_{3/2}$  and  $3^2\text{D}_{5/2}$  levels. One arm of the Raman transition, from  $4^2\text{S}_{1/2}$  to  $4^2\text{P}_{3/2}$ , is off-resonantly driven by a 393 nm laser and the other arm of the Raman transition, from  $4^2\text{P}_{3/2}$  to  $3^2\text{D}_{5/2}$  (854 nm), is off-resonantly driven by the cavity. After emission of an 854 nm photon, the electron is in the metastable excited state  $3^2\text{D}_{5/2}$  of the 729 nm optical qubit. In free space, the emission from the  $4^2\text{P}_{3/2}$  state would lead to an 854 nm photon only in 5.3% of the cases, as reflected by the branching ratio shown in fig. 2.2. The photon emission on this transition can be greatly enhanced as a result of the coupling to the cavity.

When implementing such a cavity-mediated Raman process in the lab, there are requirements to how frequency-narrow and frequency-stable (relatively and absolutely stable) the two arms of the Raman transition should be. This frequency-stability can be achieved via laser locking. In chapter 4 our approach to frequency-stabilize the cavity-mediated Raman process via a transfer lock scheme is presented, which is the main focus of the work done in the course of this master's thesis.

## 2.5. Trapped-Ion Quantum Network Protocols

Two approaches to building a quantum network based on cavity-enhanced trapped-ion nodes will now be presented. One approach is based on the direct transfer of a quantum state via state mapping from an atom onto a photon and vice versa. Such a protocol can be considered deterministic over short distances [14]. Over longer distances photon loss leads to a decrease of success probability of the protocol. A second model is based on a coincidence detection of two photons, entangled with two remote ions, after interference at a polarizing beam splitter (PBS) [15]. In this scheme, two remote ions are probabilistically projected into an entangled state [22]. This pair of entangled nodes can then be used as a resource for the teleportation of quantum information. Even though this protocol is probabilistic, the successful cases are heralded.

---

<sup>4</sup>If there is a photon in the cavity, the reverse process can take place where the photon is annihilated, denoted by  $\hat{a}$ , and the drive laser takes the atom back to  $|g_1\rangle$ . When the photon stays in the cavity for a long enough time it is possible to observe Rabi oscillations.

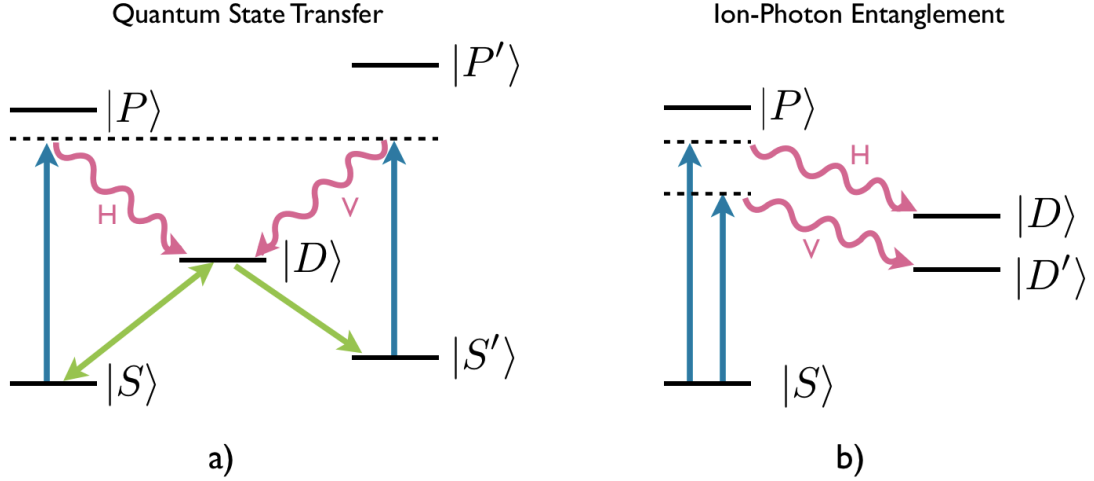


**Figure 2.10.:** a) Quantum state transfer: 1. Preparation of the ion in a superposition of  $|S\rangle$  and  $|S'\rangle$  via two 729 nm laser pulses (green) 2. Off-resonant coupling to  $|P\rangle$  and  $|P'\rangle$  via a bichromatic Raman field (blue) 3. Decay to the  $|D\rangle$  state, where a horizontally (H) or vertically (V) polarized photon is emitted (pink). b) Ion-Photon Entanglement: 1. Off-resonant coupling of the states  $|S\rangle$  and  $|P\rangle$  via a bichromatic Raman field (blue) 2. Decay to the  $|D\rangle$  and  $|D'\rangle$  state, where a horizontally (H) or vertically (V) polarized photon is emitted (pink).

### 2.5.1. Quantum State Transfer From an Ion to a Photon

In section 2.4.2, the deterministic generation of a single photon via a cavity-mediated Raman process was presented. When the ion is initially in state  $|g_1\rangle$ , the drive laser couples the ion on the  $|g_1\rangle \leftrightarrow |e\rangle$  transition and the ion couples to the cavity on the  $|e\rangle \leftrightarrow |g_2\rangle$  transition, which triggers the generation of a photon into the cavity mode. In the case that the ion is initially in the  $|g_2\rangle$  state, the ion does not couple to the drive laser and no photon emission is triggered. Therefore, when preparing a superposition of  $|g_1\rangle$  and  $|g_2\rangle$ , the cavity-mediated Raman process maps this superposition onto a superposition of having  $|0\rangle$  and  $|1\rangle$  photons in the cavity. The flying qubit is therefore encoded in the photon number states  $|0\rangle$  and  $|1\rangle$ . The photon then leaves the cavity through a partially transmissive cavity mirror and can be sent through an optical fiber channel to another ion-cavity system, where the photon can be absorbed and its quantum state can be mapped onto the other ion in the reverse process. However, photon losses in the channel are mistakenly counted as photon state  $|0\rangle$ , reducing the transfer fidelity, which describes the overlap between the initial ion and final photon state. A more robust approach is based on encoding the flying qubit in two different states of a single photon, e.g. two orthogonal polarization states.

In [14], mapping of the quantum state encoded in a trapped-ion qubit onto the polarization state of a photon qubit, was experimentally realized. The authors were able to achieve transfer fidelities of 92%. In the protocol described in the paper, which is illustrated in figure 2.10a, a superposition of the electronic states  $|S\rangle = |4^2S_{1/2}, m_j = -1/2\rangle$  and  $|S'\rangle = |4^2S_{1/2}, m_j = +1/2\rangle$  of the ion is first prepared, using a laser on the 729 nm qubit transition in a two-stage process.

## 2. Quantum Networks

Via a bichromatic cavity-mediated Raman process, the superposition state is mapped onto a superposition of photon polarization states  $|H\rangle$  and  $|V\rangle$

$$(\cos(\theta/2)|S\rangle + e^{i\phi}\cos(\theta/2)|S'\rangle) \otimes |0\rangle \longrightarrow |D\rangle \otimes (\cos(\theta/2)|H\rangle + e^{i\phi}\cos(\theta/2)|V\rangle) \quad (2.43)$$

where the superposition's phase and amplitude is preserved and no information remains in the ion after the mapping process. Here,  $\phi$  is the phase of the laser which prepares the superposition of the two states  $|S\rangle$  and  $|S'\rangle$ , and  $\theta$  can be chosen by controlling how long this laser interacts with the ion for. The mapping process is implemented by driving two Raman transitions which couple the states  $|S\rangle$  and  $|S'\rangle$  to the same final state  $|D\rangle = |3^2D_{5/2}, m_j = +1/2\rangle$  via two intermediate states  $|P\rangle = |4^2P_{3/2}, m_j = -1/2\rangle$  and  $|P'\rangle = |4^2P_{3/2}, m_j = +1/2\rangle$ . Specifically, the Raman laser field is bichromatic, where the frequency difference is given by the energy difference between  $|S\rangle$  and  $|S'\rangle$ . An initial state  $|S\rangle$  ( $|S'\rangle$ ) results in the emission of a horizontally (vertically) polarized single photon, when projected into the optical cavity direction (perpendicular to the quantization axis set by the applied DC magnetic field).

### 2.5.2. Ion-Photon Entanglement and Remote Ion-Ion Entanglement

In [15] the experimental realization of entanglement between a trapped  $^{40}\text{Ca}^+$  ion qubit and photon qubit is presented. The authors were able to create entangled states with fidelities of  $97.4(2)\%$ <sup>5</sup>, which describe the overlap between the generated state and a maximally-entangled Bell state. In this protocol the ion is first prepared in the state  $|S\rangle = |4^2S_{1/2}, m_j = -1/2\rangle$ . Then, a bichromatic Raman and cavity field couples the ground state simultaneously to the two states  $|D\rangle = |3^2D_{5/2}, m_j = -3/2\rangle$  and  $|D'\rangle = |3^2D_{5/2}, m_j = -5/2\rangle$  via the intermediate state  $|P\rangle = |4^2P_{3/2}, m_j = -3/2\rangle$ . Here, the frequency difference between the two Raman fields corresponds to the energy difference between  $|D\rangle$  and  $|D'\rangle$ . If the final state of the transition is  $|D\rangle$  ( $|D'\rangle$ ) a horizontally (vertically) polarized photon is emitted into the cavity, as shown in figure 2.10b. The state created via the protocol is given by

$$|S\rangle \otimes |0\rangle \longrightarrow (\cos(\theta/2)|DH\rangle + e^{i\phi}\cos(\theta/2)|D'V\rangle) \quad (2.44)$$

where  $\theta$  is determined by the ratio of coupling strengths of the two Raman transitions and  $\phi$  is related to the relative phase of the Raman fields.

Such an ion-photon entangled state can then be used to produce remote ion-ion entanglement between two nodes in a quantum network. The states of two ions in two different traps, each entangled with a photon, can be written as:

$$\begin{aligned} |\Psi_1\rangle &= \alpha_1|D_1H_1\rangle + \beta_1|D'_1V_1\rangle \\ |\Psi_2\rangle &= \alpha_2|D_2H_2\rangle + \beta_2|D'_2V_2\rangle \end{aligned} \quad (2.45)$$

As shown in figure 2.11, the two photons are overlapped at a PBS, which e.g. transmits horizontally polarized and reflects vertically polarized photons. The total system state before the PBS is described by a product state

$$\begin{aligned} |\Psi_1\Psi_2\rangle &= \alpha_1\alpha_2|D_1H_1D_2H_2\rangle + \alpha_1\beta_2|D_1H_1D'_2V_2\rangle + \\ &\quad \beta_1\alpha_2|D'_1V_1D_2H_2\rangle + \beta_1\beta_2|D'_1V_1D'_2V_2\rangle. \end{aligned} \quad (2.46)$$

<sup>5</sup>The classical threshold is at 50%.

## 2. Quantum Networks

Placing one photodetector at each of the output ports of the PBS provides the possibility to measure either one photon at each detector or two photons at one of the detectors. In the case of detecting a photon at each output port, it is not possible to know if either both photons were transmitted or both were reflected at the PBS, such that only the first and last term in eq. 2.46 contribute. The two remote ions are then projected into an entangled state

$$|\Psi\rangle = \frac{1}{\sqrt{|\alpha_1\alpha_2|^2 + |\beta_1\beta_2|^2}}(\alpha_1\alpha_2|D_1D_2\rangle + \beta_1\beta_2|D'_1D'_2\rangle). \quad (2.47)$$

In the other case, when one photon is transmitted and one is reflected, such that both photons emerge in the same output path of the PBS, information about which photon came from where is available and the ions are simply projected into a product state. Therefore, this scheme is probabilistic, where a coincidence detection after the PBS heralds the success of the protocol. In order for this protocol to work, there must be no way of knowing which photodetector click came from which photon source.

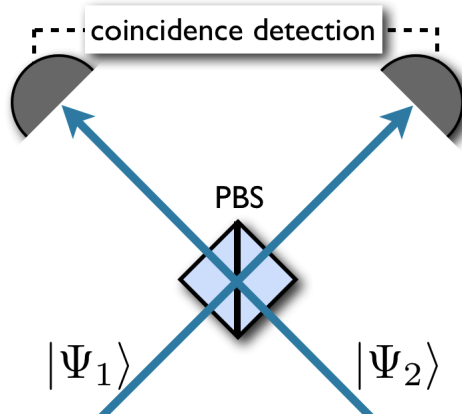


**Figure 2.11.:** The coincidence detection of two photons after the PBS projects two remote ions into an entangled state.

# 3. Lasers and Laser Locking

## 3.1. Basic Principles of Laser Operation

The frequency-stabilization of a cavity-mediated Raman process via a transfer lock scheme, which is presented in detail in chapter 4, is based on the frequency-stabilization of two lasers. In order to provide the necessary theory background, this chapter is concerned with the basic mechanisms behind the operation of a laser, schemes to frequency-stabilize a laser to an appropriate reference and approaches to characterize the frequency-stability of a locked laser system.

In this first section, the operation principles of diode lasers and titanium sapphire (Ti:Sa) lasers are introduced, as these two types of lasers are used in the course of this thesis to implement a transfer lock. Two spectral characteristics of a laser, which are important in quantum information experiments, are the linewidth and drift of a laser. Noise processes which affect these parameters are also presented in this section.

### 3.1.1. General Principles

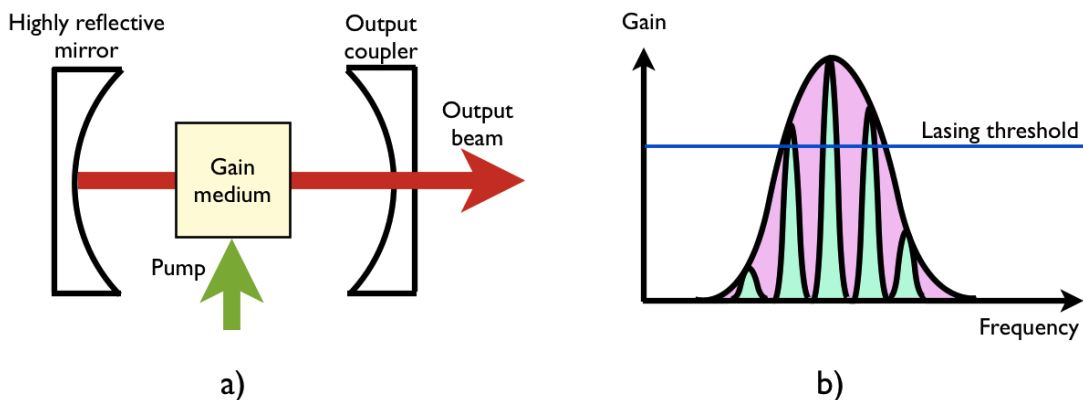


**Figure 3.1.:** a) Basic principle of laser operation: A gain medium inside the laser cavity is pumped (green) which results in population inversion. Laser light (red) is transmitted through a partially transmissive output-coupler mirror of the laser cavity. b) The gain profile of a laser is illustrated in pink. The modes of the laser cavity are shown in green. Modes which exceed the lasing threshold (blue line) can start lasing.

The light emitted by a laser exhibits high intensity, and high temporal and spatial coherence, which manifests in monochromaticity and strong spatial confinement [46]. The principle of a laser is based on the stimulated emission of photons, which requires three components: a gain medium, a pump and an optical cavity, as presented in figure 3.1a.

### 3. Lasers and Laser Locking

Photons are generated via spontaneous emission in a gain medium when an emitter, e.g. an atom, transitions from an excited state to a lower lying energy state. By adding energy to the system, the pump generates population inversion in the gain medium, which means that over 50 % of the emitters are in the excited state. The pumping process can e.g. be optical, typical for solid-state lasers, or via electrical current, often used in diode lasers. When population inversion is achieved, a spontaneously emitted photon can stimulate the emission of another photon which has the same frequency, direction, phase and polarization as the first, by triggering the de-excitation of an emitter in the gain medium. An optical cavity acts as a filter, where inside only modes satisfying the resonance condition interfere constructively and are thus amplified. The reflected photons can trigger the emission of other coherent photons, which leads to a chain reaction.

Which cavity mode starts to lase, depends on its position within the gain profile of the laser, as shown in figure 3.1b. The gain profile describes the radiation amplification as a function of the frequency, and its center frequency and shape is determined by the properties of the gain medium. A limited number of cavity modes possess the required intensity to be able to start lasing, such that the laser output is dominated by stimulated emission. The lasing threshold is surpassed when the gain exceeds the sum of all losses per cavity roundtrip, the most dominant of which are absorption and scattering of light as well as transmission at the laser cavity mirrors. Modes which are further away from the center of the gain profile often don't emerge with enough power to be amplified.

Single-mode operation can be achieved by frequency selective feedback, as presented in section 3.2.3, or by inserting an intracavity filter, e.g. an etalon (basically another cavity) [47]. One of the mirrors of the laser cavity is used as an output coupler, where some fraction of the light resonating inside the cavity is transmitted. Lasers are operated either in a continuous way (cw for continuous wave) or produce short, e.g.  $< 10^{-13}$  s [48], intense pulses. The work in this thesis is mainly concerned with cw lasers, except section 3.3.2, where the theory of frequency combs, based on pulsed lasers, is briefly presented.

#### 3.1.2. Diode Laser

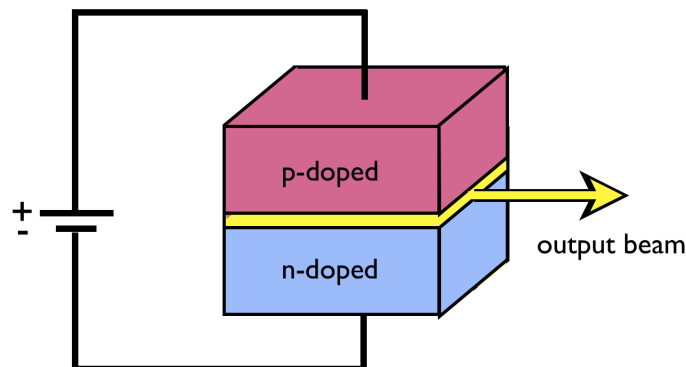


**Figure 3.2.:** Basic principle of a laser diode: A forward-biased p-n junction is shown, where in between the p- and n-doped materials a depletion region forms. When the voltage applied across the junction is sufficiently high, laser light (yellow) is emitted from the depletion region (active layer). The left and right side of this junction is polished to form a laser cavity.

### 3. Lasers and Laser Locking

A laser diode consists of a forward-biased junction between positively- (p-) and negatively- (n-)doped semiconductor materials [46], as illustrated in figure 3.2. Once a voltage is applied across the diode, electrons and holes are injected from opposite sites into a depletion region between the two differently-doped regions. Electrons are injected from the n-doped material and holes are injected from the p-doped material. Holes in the valence band recombine with electrons from the conduction band in the “active layer” which results in the emission of photons. These photons are approximately monoenergetic and centered around a frequency which corresponds to the bandgap energy. If the bias voltage, and thus the corresponding “injection current”, is sufficiently high, the electron concentration in the conduction band exceeds the electron concentration in the valence band, such that population inversion is achieved. The sides of a laser diode are polished to form an optical cavity, with one highly- and one partially-reflective surface. Photons are reflected many times, stimulate the recombination of electron-hole pairs in the active layer and lasing can occur.

#### 3.1.3. Titanium Sapphire Laser

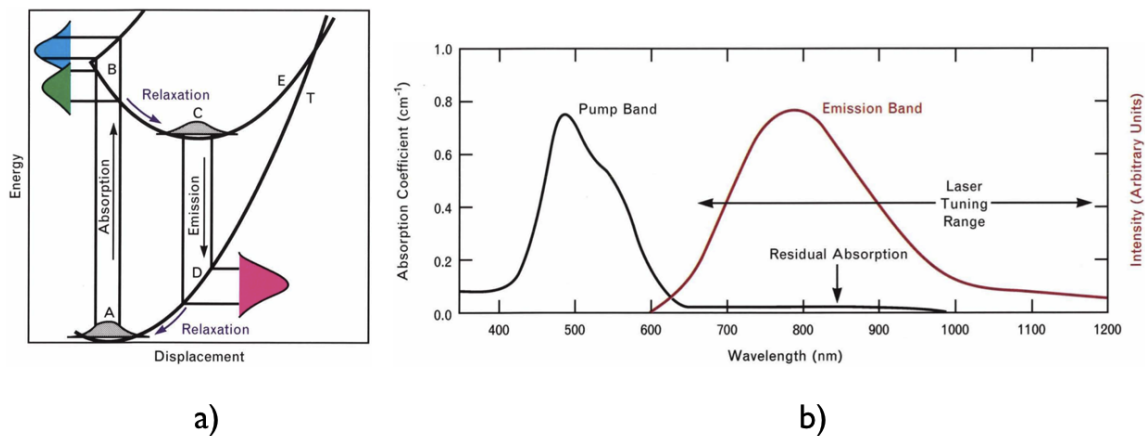


**Figure 3.3.:** a) Transitions involved in the lasing process of a Ti:Sa laser: A green laser takes the population from A to B (electronic transition), which is followed by the emission of phonons while the titanium ion displaces its position to C. An electronic transition from C to D occurs, where a photon in the red is emitted. This is followed by another emission of phonons such that the population returns to A. b) Absorption band (black) and emission band (red) of a Ti:Sa laser: The bands are well separated which avoids self-absorption. The wide tuning range of the laser is defined by the emission band. Images taken from [48].

Ti:Sa lasers are solid-state lasers, which can emit at multi-Watt cw powers and are among the most widely tunable lasers available [48]. The gain medium consists of a sapphire ( $\text{Al}_2\text{O}_3$ ) crystal which is doped with titanium ions ( $\text{Ti}^{3+}$ ), substituting for aluminium. The lasing transition involves two electronic levels of the  $\text{Ti}^{3+}$  ion. Population inversion is achieved by pumping the gain medium optically with a green laser. Once the titanium ion is pumped to the excited state, it displaces its position with respect to the oxygen atoms in the crystal lattice to be able to minimize the system energy. The displacement of the titanium ion is accompanied by the emission of phonons. Next, the titanium

### 3. Lasers and Laser Locking

ion undergoes an electronic transition from the excited state to a high vibrationally-excited level of the electronic ground state. As a result, a Stokes-shifted photon with longer wavelength, in the red, is emitted. The ion then quickly relaxes to the vibronic ground state by emitting phonons, which leaves the final state of the photon transition basically unpopulated, making it easy to achieve population inversion. These processes are illustrated in figure 3.3a. The possibility to populate many vibronic states gives rise to broad absorption and emission spectra, as shown in figure 3.3b. The broad emission spectrum allows for the wide tuning range of the Ti:Sa laser. The output wavelength can be tuned e.g. by rotating a birefringent filter inside the laser cavity, which introduces a wavelength-dependent loss [47]. Due to the well-separated absorption and emission bands, there is very little self absorption, which allows for high output powers.

#### 3.1.4. Laser Linewidth and Drift

The linewidth  $\Delta\nu$  of a single-mode cw laser is typically defined as the full width at half-maximum (FWHM) of the laser's optical spectrum. The minimum possible FWHM linewidth, derived by Schawlow and Townes is given by [49]

$$\Delta\nu = \frac{4\pi h f (\delta\nu)^2}{P_{\text{out}}} \quad (3.1)$$

where  $f$  is the center frequency of the laser light,  $P_{\text{out}}$  is the laser output power and  $\delta\nu$  is FWHM linewidth of the laser cavity. The Schawlow-Townes linewidth is derived under the assumption that only spontaneous emission, which introduces phase noise into the laser mode, contributes to the laser linewidth. In reality, this limit is difficult to reach as there are many noise sources which contribute to a laser's linewidth. Such noise sources include e.g. temperature fluctuations, vibrations and pressure fluctuations, which can e.g. affect the length of the laser cavity or shift the gain profile, which changes the wavelength of the light on respective timescales associated with the nature of the noise.

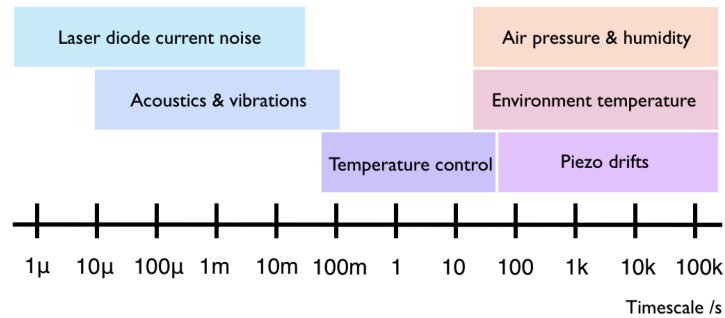


**Figure 3.4.:** Noise processes that affect lasers in the lab with their characteristic timescales based on information provided in [50].

In figure 3.4, some important noise processes affecting the frequency-stability of lasers in the lab are visualized, with characteristic timescales [50]. A measurement of a laser spectrum, which is discussed in section 3.3, is done within a certain measurement time, usually from a few hundred microseconds to seconds long. Fast noise processes like high frequency acoustic vibrations happen on a faster timescale, such that the measured

spectrum of the laser is broadened. Slow noise processes, like temperature changes in the lab lead to drifts of the laser wavelength between individual measurements. A linewidth measurement should therefore always be stated in combination with the timescale of measurement, as the result depends strongly on it. Even though there exist many noise sources that broaden the linewidth of a laser, narrow linewidths can still be achieved by actively stabilizing the laser to a reference, which is discussed in section 3.2.

## 3.2. Frequency-Stabilization of a Laser

Stabilizing a laser to a frequency reference allows its linewidth to be narrowed and its drift rate to be compensated (to a certain extent). This section focuses on the three components, which are required for laser stabilization: A frequency reference, a locking scheme, and feedback elements to control the frequency of the laser.

### 3.2.1. An Optical Cavity as a Frequency Reference

The frequency-stabilization of a laser is often implemented via a locking scheme which employs a well-isolated and self-stable optical cavity as a frequency reference. A cavity acts as a filter and transmits light only at certain wavelengths corresponding to the longitudinal modes of the cavity, which satisfy the resonance condition (eq. 2.31). Temperature-controlled optical cavities with ULE (ultra-low expansion glass) mirror spacers placed in vacuum provide very high short-term length stability, as the cavity is well isolated from acoustic noise, temperature fluctuations and air pressure fluctuations, which can result in changes of the optical path length of the cavity and thus changes of the resonance frequency.

By using a control loop, where an error signal is derived from the cavity resonance signal, feedback can be applied to the laser to keep it locked to the cavity resonance. However, aging-related drifts of the reference-cavity limit the long-term stability of such a laser lock. As a result, a laser stabilized to a reference-cavity will drift along with the cavity.

#### Cavity Modes and Stability

A stability criterion for a two-mirror cavity derived from ray optics, which describes the ability for light to be confined, is given by [46]

$$0 \leq g_1 g_2 \leq 1 \quad (3.2)$$

where  $g_1$  and  $g_2$  are the stability parameters for the two cavity mirrors which can be calculated as

$$g_i = 1 - \frac{L}{r_{c,i}}. \quad (3.3)$$

Here  $r_{c,i}$  is the radius of curvature of mirror  $i$ . Planar-mirror cavities, where the radii of curvature approach infinity, are on the edge of the stability regime and display a high sensitivity to misalignment. Therefore, at least one of the mirrors of a cavity is typically

### 3. Lasers and Laser Locking

curved, which provides a more stable configuration for the confinement of light, less sensitive to beam misalignment, under the geometrical conditions introduced by 3.3.

The modes of a cavity are the solutions to the paraxial Helmholtz equation under the boundary conditions imposed by the cavity mirrors [46]. The curvature of the wavefront of the cavity mode at both mirrors has to match the mirror curvatures, in order for the light field to be able to self-consistently exist inside the optical cavity. The simplest solution is the Gaussian beam. The electric field of a Gaussian beam at a radial distance  $\rho$  from the center axis and axial distance  $z$  from the beam focus, as shown in figure 3.5a, is given by

$$E(\rho, z) = A_0 \frac{w_0}{w(z)} e^{-\frac{\rho^2}{w^2(z)}} e^{-ikz - \frac{ik\rho^2}{2r_c(z)} + i\zeta(z)}. \quad (3.4)$$

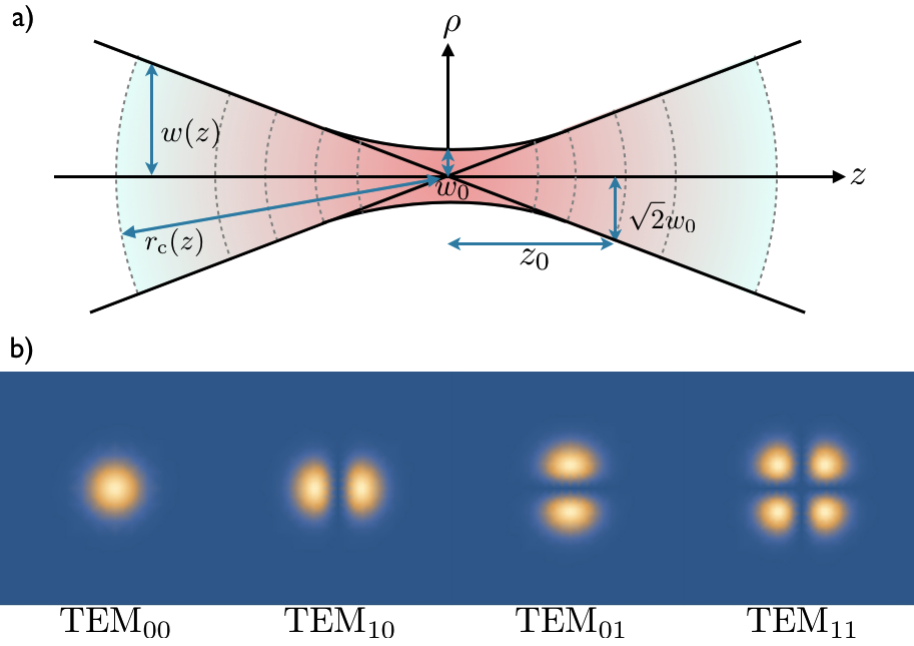


**Figure 3.5.:** a) Electric field distribution of a Gaussian beam ( $\text{TEM}_{00}$ ) along the radial ( $\rho$ ) and axial ( $z$ ) direction. The radial intensity profile is a Gaussian distribution with width  $2w(z)$ . b) Radial intensity distribution of the Gaussian beam and higher order Hermite-Gaussian modes.

The beam radius, which is defined as the radius where the radial intensity drops to  $1/e^2$  of the value at  $\rho = 0$ , is given by

$$w(z) = w_0 \sqrt{1 + \left(\frac{z}{z_0}\right)^2} \quad (3.5)$$

where  $w_0$  is the beam waist, the smallest beam radius at the focus, and

$$z_0 = \frac{\pi w_0^2}{\lambda} \quad (3.6)$$

is the Rayleigh range, which describes the distance from the focus where the beam radius has increased by a factor of  $\sqrt{2}$ . The beam waist

$$w_0 = \sqrt{\frac{L\lambda}{\pi}} \sqrt[4]{\frac{g_1 g_2 (1 - g_1 g_2)}{(g_1 + g_2 - 2g_1 g_2)^2}} \quad (3.7)$$

### 3. Lasers and Laser Locking

and the beam radius  $w_1$  and  $w_2$  at cavity mirror 1 and 2

$$\begin{aligned} w_1 &= \sqrt{\frac{L\lambda}{\pi}} \sqrt[4]{\frac{g_2}{g_1(1-g_1g_2)}} \\ w_2 &= \sqrt{\frac{L\lambda}{\pi}} \sqrt[4]{\frac{g_1}{g_2(1-g_1g_2)}}. \end{aligned} \quad (3.8)$$

can be expressed as a function of the stability parameters of the two mirrors [51]. The radius of curvature of the beam is given by

$$r_c(z) = z \left( 1 + \left( \frac{z_0}{z} \right)^2 \right) \quad (3.9)$$

which approaches infinity at the focus. The Gouy phase

$$\zeta(z) = \arctan \left( \frac{z}{z_0} \right) \quad (3.10)$$

describes the phase retardation that a Gaussian beam acquires relative to a plane wave with the same optical frequency. The resonance frequencies of the Gaussian modes with longitudinal mode index  $q$  are given by

$$\nu_q = q\nu_{\text{FSR}} + \frac{1}{\pi}\nu_{\text{FSR}} \arccos(\sqrt{g_1g_2}) \quad (3.11)$$

where the term  $\arccos(\sqrt{g_1g_2})$  is equal to the total Gouy phase shift along the cavity length [51]. This result is derived from the condition that the round trip phase shift must equal an integer multiple of  $2\pi$ , to allow for constructive interference.

The Gaussian beam is not the only solution to the paraxial Helmholtz equation, which can exist in a cavity. Higher-order modes are described by Hermite-Gaussian beams, which, in comparison to Gaussian beams, have a more complicated radial intensity distribution, as presented in figure 3.5b. Considering the transverse mode indices  $m$  and  $n$ , the resonance frequencies for the fundamental Gaussian mode, where  $m, n = 0$ , and higher order Hermite-Gaussian modes, where  $m + n > 0$ , are given by

$$\nu_{qmn} = q\nu_{\text{FSR}} + \frac{1}{\pi}\nu_{\text{FSR}}(m + n + 1) \arccos(\sqrt{g_1g_2}). \quad (3.12)$$

Higher order modes experience a phase shift per round trip, that is larger by a factor of  $(m + n + 1)$  in comparison with the fundamental Gaussian mode. As a result, the frequencies of these modes are higher. Modes which have different longitudinal mode indices  $q$  but the same transverse mode indices, display the same intensity distribution. Therefore, the longitudinal mode index  $q$  is often omitted as it is not important and the possible modes of a cavity are described as  $\text{TEM}_{mn}$ , where TEM stands for transverse electromagnetic.

A free-propagating laser beam can also be described by a Gaussian mode. When coupling laser light into a cavity, the Gaussian beam profile of the laser is matched to the cavity mode, defined by the mirrors. This is done either by having the cavity select the fraction of the light that matches the cavity mode, or by using one or more lenses to improve the

### 3. Lasers and Laser Locking

matching. Such mode matching techniques increase the power resonating in a specific mode while suppressing others. When the mirror properties of the cavity are known, such that the waist of the cavity mode can be calculated, the required focal length  $f$  of a single lens to match the waist of the laser to the cavity waist can be calculated via

$$f = \frac{\pi w_0 w_f}{\lambda} \quad (3.13)$$

where  $w_0$  ( $w_f$ ) is the beam waist before (after) passing the lens [51].

#### Transmission/Reflection Profile of an Optical Cavity

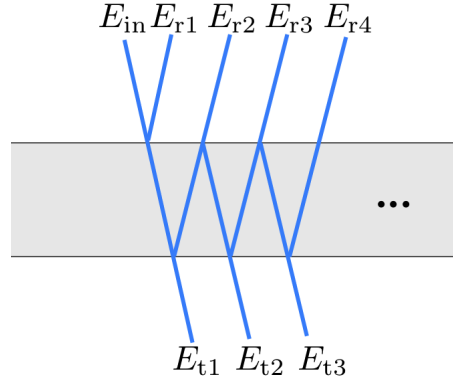


**Figure 3.6.:** Light beams (blue) transmitted and reflected at a cavity with plano-parallel mirrors (grey): The beams are drawn at an angle to visualize the contribution of the individual beams to the total reflected and transmitted beam.

To derive the transmitted and reflected intensity profiles of a cavity as a function of the frequency of the light, it is sufficient to investigate the simple case of two identical plano-parallel mirrors, as illustrated in figure 3.6, and an incident plane wave (illustrated as a beam) of amplitude  $E_0$ , frequency  $\omega$  and wave number  $k$ :

$$E_{\text{in}} = E_0 e^{i(kx - \omega t)} \quad (3.14)$$

When a wave is reflected at an interface between two regions of different index of refraction, e.g. at a mirror, it experiences a phase shift of  $\pi$ . The transmission (reflection) coefficient  $t^2 = T$  ( $r^2 = R$ ) characterizes what fraction of incident light power is transmitted (reflected) at the mirror. The first reflected beam

$$E_{r1} = E_{\text{in}} r e^{i\pi} \quad (3.15)$$

does not enter the cavity. The other reflected beams correspond to light leaking out of the cavity and obtain an additional phase shift  $2kL$  from passing through the cavity of length  $L$  twice.

$$\begin{aligned} E_{r2} &= E_{\text{in}} t^2 r e^{i2kL} \\ E_{r3} &= E_{\text{in}} t^2 r^3 e^{i4kL} \\ &\dots \\ \text{for } n \neq 1 : E_{rn} &= E_{\text{in}} t^2 r^{2n-3} e^{i(2n-2)kL} \end{aligned} \quad (3.16)$$

### 3. Lasers and Laser Locking

The total reflected light can be described by

$$E_r = -rE_{\text{in}} + E_{\text{in}}t^2re^{i2kL} \sum_{j=2}^n (r^2e^{i2kL})^{j-2} \quad (3.17)$$

where the sum can be rewritten as

$$\sum_{j=2}^n (r^2e^{i2kL})^{j-2} = \sum_{j=0}^{n-2} (r^2e^{i2kL})^j \quad (3.18)$$

and eq. 3.17 can be further simplified to

$$E_r = -E_{\text{in}}r + E_{\text{in}}t^2re^{i2kL} \frac{1}{1 - r^2e^{i2kL}} \quad (3.19)$$

by letting  $n \rightarrow \infty$  and using the equation for a geometric series

$$\sum_{j=0}^{\infty} x^j = \frac{1}{1 - x}. \quad (3.20)$$

Neglecting mirror losses ( $t^2 = 1 - r^2$ ), the ratio of reflected to incident wave, i.e. the cavity reflection coefficient, can be written as as

$$\mathcal{R} = \frac{E_r}{E_{\text{in}}} = \frac{r(e^{i2kL} - 1)}{1 - r^2e^{i2kL}} = \frac{r(e^{i\frac{\omega}{\nu_{\text{FSR}}}} - 1)}{1 - r^2e^{i\frac{\omega}{\nu_{\text{FSR}}}}} \quad (3.21)$$

where  $\nu_{\text{FSR}}$  is the free spectral range, the frequency spacing of the longitudinal cavity modes. The ratio of reflected intensity to incident intensity is then given by:

$$\frac{I_r}{I_{\text{in}}} = |\mathcal{R}|^2 = \frac{\mathcal{F} \sin(kL)^2}{1 + \mathcal{F} \sin(kL)^2} \quad (3.22)$$

where

$$\mathcal{F} = \frac{4r^2}{(1 - r^2)^2} \quad (3.23)$$

is the coefficient of finesse. For  $kL \ll 1$ , this expression can be approximated near resonance as

$$\frac{I_r}{I_{\text{in}}} \approx \frac{\mathcal{F}(kL)^2}{1 + \mathcal{F}(kL)^2} \quad (3.24)$$

which corresponds to a dip, the shape of a Lorentzian profile.

Analogously, the Lorentzian transmission profile can be derived

$$\frac{I_t}{I_{\text{in}}} = \frac{1}{1 + \mathcal{F} \sin(kL)^2} \approx \frac{1}{1 + \mathcal{F}(kL)^2}. \quad (3.25)$$

The modes in transmission are shown in figure 3.7, as a function of frequency. When including losses, which result e.g. from light scattering and absorption, with loss coefficient  $l^2 = L$  in the calculation, where now  $R + T + L = 1$ , the maximum intensity of the

### 3. Lasers and Laser Locking

mode in transmission is reduced by a factor  $T^2/(1-R)^2$  [52]. The depth of the mode in reflection is also reduced by that factor.

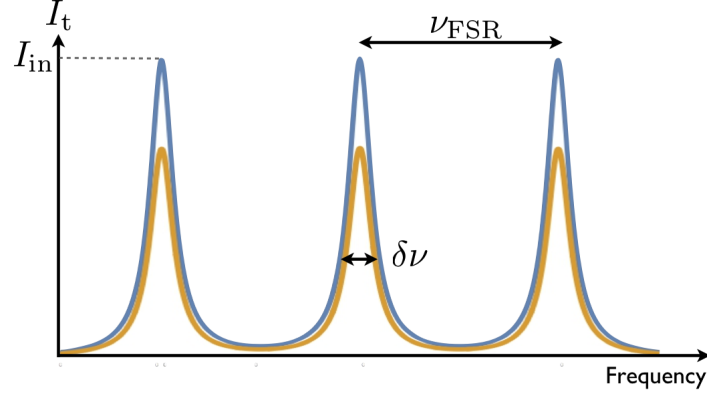


**Figure 3.7.:** Transmitted intensity profile for a cavity with two identical mirrors: The modes repeat at multiples of the free spectral range  $\nu_{\text{FSR}}$ . The blue curve represents the transmission profile of a cavity without losses, where the maximum of transmitted intensity is equal to  $I_{\text{in}}$ . Mirror losses are considered for the orange curve, where the height of the mode, compared to the blue curve, decreases by a factor  $T^2/(1-R)^2$ .

#### Finesse

The cavity FWHM linewidth  $\delta\nu$  can be written as the ratio of the free spectral range to the finesse  $F$ , which characterizes how long a photon is stored inside an optical cavity before it leaks out:

$$\delta\nu = \frac{\nu_{\text{FSR}}}{F} = \frac{c}{2LF} \quad (3.26)$$

One approach to determine the finesse is via a cavity ringdown measurement. Here, a laser on cavity resonance is rapidly switched off and light which is stored in the cavity decays in an exponential manner

$$I(t) = I_0 e^{-\frac{t}{\tau}} \quad (3.27)$$

where the time constant  $\tau$  is inversely proportional to the cavity decay rate  $\kappa$  and related to the finesse via

$$\tau = \frac{1}{\kappa} = \frac{FL}{\pi c}. \quad (3.28)$$

Given that the mirror transmission coefficients  $T_1$  and  $T_2$  and the finesse of a cavity are known, an estimation of the mirror losses can be made by relating the finesse to the sum of the total round trip losses in the cavity via [52]

$$F \approx \frac{2\pi}{T_1 + T_2 + L_1 + L_2} \quad (3.29)$$

which is valid for high-finesse cavities, where mirror losses are small.

### 3.2.2. Pound-Drever-Hall Laser Locking Scheme

When a laser is approximately on resonance with a cavity mode, a change in laser frequency results in a change in transmitted and reflected light intensity. To frequency-stabilize the laser, one can apply feedback to the laser to keep the intensity of the light in transmission or reflection at a constant value. One simple option is to lock to the side of a cavity transmission fringe, where the intensity gradient is highest. However, an error signal derived from the cavity reflection rather than transmission has two advantages. First, when deriving an error signal from the cavity transmission, one is limited by the response time of the cavity, as photons are stored inside for some amount of time. Laser frequency fluctuations that happen on a timescale faster than this storage time cannot be detected in transmission and corrected for. Second, locking to the center of the cavity reflection, which is ideally zero, if the cavity has no losses and identical mirrors, allows for the decoupling of laser intensity fluctuations from frequency fluctuations. However, an error signal which is antisymmetric with respect to the cavity resonance is required, to be able to determine in which direction the laser frequency has to be corrected. One property of the reflected beam, which has a different sign above and below cavity resonance, is the phase of the light. The Pound-Drever-Hall (PDH) laser locking scheme, which is one of the most widely-used techniques to frequency-stabilize a laser, provides the opportunity to extract the phase of the reflected beam from a photodiode signal. Since the phase cannot be measured directly, it is measured via a heterodyne method, where the relative phase between the carrier beam and two sidebands, which are opposite in phase, is determined. The sidebands can be generated via phase modulation of the laser light, e.g. with an electro-optic modulator (EOM). For the PDH scheme, the modulation frequency should be much higher than the cavity linewidth, such that the sidebands are completely reflected when the carrier is approximately on resonance with the cavity mode. Light which is reflected at the cavity, then consists of the sidebands and, when off-resonant, the phase-shifted carrier. Exactly on resonance, the reflected signal is zero as the carrier is completely transmitted and the sidebands interfere destructively. Off resonance, the interference between the carrier and the sidebands results in an intensity change of the reflected signal. This intensity change contains information about the amount and sign of the detuning of the laser from the cavity resonance. The reflected signal, measured with a photodetector, is mixed with a local oscillator to demodulate the signal and produce an error signal close to DC. In the following, an expression for the PDH error signal is derived, based on [53].

The electric field of incident light with amplitude  $E_0$  and frequency  $\omega$

$$E_{\text{in}} = E_0 e^{i\omega t} \quad (3.30)$$

is modified to

$$E_{\text{mod}} = E_0 e^{i(\omega t + \beta \sin(\Omega_m t))} \quad (3.31)$$

when sinusoidally phase-modulating the light at frequency  $\Omega_m$ , where  $\beta$  is the modulation depth. For small  $\beta$ , the expression can be expanded in Bessel functions

$$E_{\text{mod}} \approx E_0 (J_0(\beta) e^{i\omega t} + J_1(\beta) e^{i(\omega + \Omega_m)t} - J_1(\beta) e^{i(\omega - \Omega_m)t}) \quad (3.32)$$

where the three terms correspond to the electric field associated with the carrier and the two sidebands detuned by  $\pm\Omega_m$  from the carrier, as shown in figure 3.8a. The electric

### 3. Lasers and Laser Locking

field of this beam after being reflected at a cavity is given by

$$E_r = E_0(\mathcal{R}(\omega)J_0(\beta)e^{i\omega t} + \mathcal{R}(\omega + \Omega_m)J_1(\beta)e^{i(\omega+\Omega_m)t} - \mathcal{R}(\omega - \Omega_m)J_1(\beta)e^{i(\omega-\Omega_m)t}) \quad (3.33)$$

which can be derived from eq. 3.32 by taking the cavity reflection coefficients, from eq. 3.21 for the carrier and sidebands into account. The reflected power, which is measured by a photodetector, is given by

$$\begin{aligned} P_r = |E_r|^2 = P_c|\mathcal{R}(\omega)|^2 + P_s[|\mathcal{R}(\omega + \Omega_m)|^2 + |\mathcal{R}(\omega - \Omega_m)|^2] \\ + 2\sqrt{P_c P_s}[\Re(\xi) \cos(\Omega_m t) + \Im(\xi) \sin(\Omega_m t)] \\ + (2\Omega_m \text{ terms}) \end{aligned} \quad (3.34)$$

where  $P_c = J_0^2(\beta)|E_0|^2$  and  $P_s = J_1^2(\beta)|E_0|^2$  is the power in the carrier and sideband, respectively,  $\Re$  and  $\Im$  denote the real and imaginary part, respectively, and

$$\xi = \mathcal{R}(\omega)\mathcal{R}^*(\omega + \Omega_m) - \mathcal{R}^*(\omega)\mathcal{R}(\omega - \Omega_m) \quad (3.35)$$

which contains information about the interference between the carrier and sidebands. We are therefore interested in extracting terms oscillating at  $\Omega_m$  in eq. 3.34. In the case of fast modulation, where  $\Omega_m \gg \delta\nu$ , the reflection coefficients of the sidebands can be approximated by  $-1$ , as the sidebands are completely reflected when the carrier is on or close to cavity resonance. The term  $\xi$  is then purely imaginary and the cosine term in eq. 3.34 drops out. Next, a mixer multiplies the signal from the photodetector with a local oscillator signal of frequency  $\Omega_m$ <sup>1</sup>. The mixer output then contains the sum and difference frequencies of the two input signals, which means that the signal of interest does not oscillate at  $\Omega_m$  anymore but is converted to a DC signal. Other components of the signal, that still oscillate, can then be filtered away via a low pass filter and the PDH error signal

$$\epsilon = -2\sqrt{P_c P_s}\Im(\xi) \quad (3.36)$$

is obtained. An error signal for an optimized phase between photodiode signal and local oscillator is shown in figure 3.8b.

Near cavity resonance, the signal can be approximated by a linear function with slope

$$D = -\frac{8\sqrt{P_c P_s}}{\delta\nu}. \quad (3.37)$$

The slope is steeper the smaller the cavity linewidth is and also depends on the power in the carrier and sidebands. For a fixed incident power, the steepest slope can be achieved when the ratio of the power in the sideband to the carrier is

$$\frac{P_s}{P_c} = 0.42 \quad (3.38)$$

which corresponds to a modulation depth of  $\beta = 1.08$ .

---

<sup>1</sup>The phase between photodiode signal and local oscillator has to be carefully adjusted to provide an optimized error signal for locking.

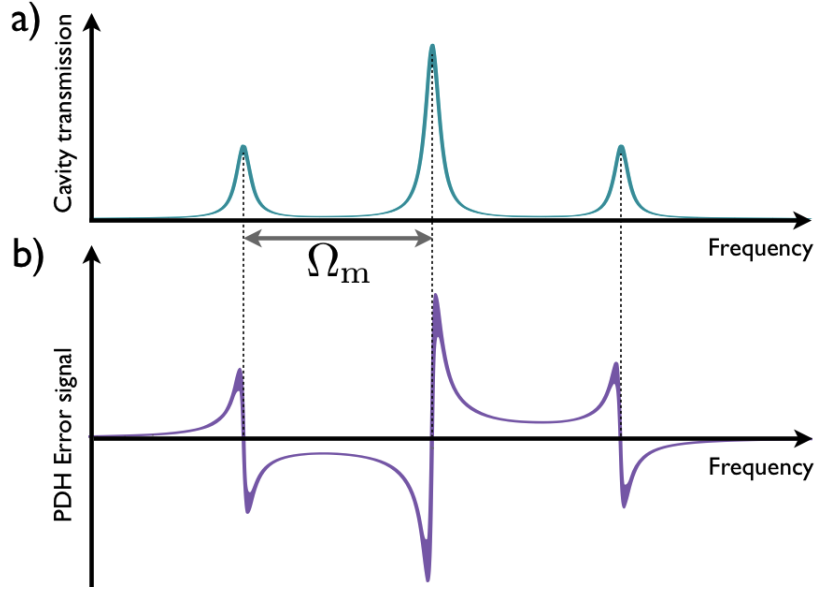


**Figure 3.8.:** a) Transmitted intensity profile with sidebands at modulation frequency  $\Omega_m$ . The height of the peaks corresponds to the power in the carrier  $P_c$  and sidebands  $P_s$ . b) PDH error signal for an optimized phase between reflected photodiode signal and local oscillator. The maximum height of the error signal is given by  $2\sqrt{P_c P_s}$ .

The linear central part of the error signal corresponds to the locking range. The PDH error signal is sent to the input of a controller, e.g. a Proportional-Integral-Derivative (PID) controller [54], which modifies the error signal and provides, if the control parameters are set correctly, an optimized output signal for locking. The output signal is then sent to a feedback element, as presented in section 3.2.3, which controls the frequency of the laser to keep it locked to the cavity resonance. The PDH scheme is often used to stabilize the frequency of a laser as well as narrow its linewidth. By applying very fast feedback, the control loop can counteract noise processes which broaden the linewidth of the laser to achieve narrow laser linewidths on a timescale of seconds. Based on experience in our group, laser linewidths a factor of 100 to 1000 times smaller than the reference-cavity linewidth can be achieved. On the other hand, the PDH scheme can also be used to stabilize the length of a cavity with a stable laser as a frequency reference, as required for the cavity-mediated Raman process.

### Residual Amplitude Modulation

Residual amplitude modulation (RAM) [55] can degrade the stability of a laser locked via the PDH scheme. The dominant contribution to RAM is typically caused by a misalignment between the polarization of the light with one of the principal axes of the birefringent crystal inside the EOM used for the phase modulation process. The polarization is thus rotated at the modulation frequency  $\Omega_m$ , as different polarization components experience different phase shifts. After polarization filtering optics, this polarization rotation is converted to an amplitude modulation of the laser beam. As a result of this RAM, the modulation sidebands can become unequal in magnitude or not exactly opposite in phase, which can prevent the cancellation of the sidebands on

### 3. Lasers and Laser Locking

resonance. A DC offset of the error signal after the mixer is obtained which is fed back to the laser frequency via the lock. The birefringence in the crystal is temperature dependent, which can mean that temperature changes in the lab can lead to changes in RAM and therefore in the DC offset of the PDH error signal. The laser's locking point is thus drifting along with temperature. There exist approaches to reduce RAM resulting from the phase modulation process, like temperature-stabilizing EOMs used in locking setups. Also, it is beneficial to use an EOM which contains two crystals in a "compensation configuration" [56]. The two crystals are rotated 90 degrees with respect to each other, such that temperature dependent birefringence changes in the first crystal are compensated by anti-correlated birefringence changes in the second crystal. Another scheme is based on generating an error signal not with a local oscillator of frequency  $\Omega_m$ , but rather to use  $3\Omega_m$ , which suppresses the relative offset due to RAM by a factor of 20, compared to the regular PDH scheme [57]. It is also possible for RAM to be induced by unwanted etalon effects, which describe the generation of standing waves between optical components. To avoid such etalons, optical components should be anti-reflection coated and optical isolators, through which light can only pass in one direction, should be installed in the beam path.

#### 3.2.3. Feedback Elements of Lasers

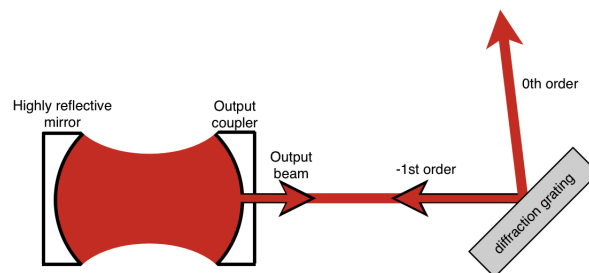


**Figure 3.9.:** ECDL in Littrow configuration: The light diffracted ( $-1$ st order) at the grating is sent back into the laser. Essentially the grating acts as another mirror, which forms another cavity with the first (highly reflective) mirror. The  $0$ th diffraction order is used as the new output beam to be sent to the experiment.

Typically, lasers can be tuned over a certain wavelength range, which is limited by the bandwidth of the laser's gain profile or coatings of the laser cavity mirrors. Most lasers provide appropriate inputs to control feedback elements inside the laser, which change the frequency of the laser output. Sending the output signal from a PID-controller into such a feedback port of the laser allows the laser frequency to be stabilized. The bandwidth of a feedback element corresponds to the timescale over which the frequency can possibly be stabilized.

Some lasers contain cavities with a movable cavity mirror, which is mounted onto a piezo, and the laser frequency can be stabilized by feeding back to this mirror. Here, the bandwidth is limited by how fast the mirror can be moved with the piezo. Other options for feedback elements with a higher bandwidth, which are commonly used in our group, are intracavity EOMs, which change the optical path length inside the laser cavity, or

### 3. Lasers and Laser Locking

acousto-optic modulators (AOMs) at the output of the laser, which frequency shift the emitted laser light.

Diode lasers can be stabilized by feeding back to a diffraction grating and the injection current of the diode. A diffraction grating is placed outside of the laser cavity, in an extended-cavity diode laser (ECDL) configuration, as shown in figure 3.9. Such a grating allows for a frequency-selective feedback to the laser cavity, which forces the diode into single mode operation and also allows for wavelength tuning by controlling the angle of the grating. The diffraction at the grating can be described via the equation

$$n\lambda = d(\sin(\theta) + \sin(\theta')) \quad (3.39)$$

where  $n$  is the order of diffraction,  $d$  is the grating constant and  $\theta$  ( $\theta'$ ) is the angle of incidence (diffraction) of the beam with respect to the grating normal. The grating is adjusted to a position such that the  $-1$ st order of diffraction of light of a specific wavelength is fed back into the laser cavity. As a result, the emission of more photons at the specific wavelength is stimulated, which also enables modes that are not in the center of the gain profile to start lasing. The diffraction grating is usually mounted onto a piezo to be able to control the frequency with high precision. Injection current feedback provides faster frequency control. The mechanism here is that a change in current density in the diode results in a temperature and refractive index change, which in turn changes the frequency of the emitted light [58].

### 3.3. Characterization of a Stabilized Laser System

Unfortunately, it is not possible to measure optical frequencies in the hundreds of THz range directly, as even the fastest photodetectors are in the tens of GHz range. Therefore, the characterization of the frequency-stability of a laser relies on schemes where the linewidth and drift rate can be determined, without measuring the absolute laser frequency.

In this section, three schemes are presented which allow the linewidth and/or drift of a laser to be determined. First, the linewidth of a locked laser or locked cavity can be estimated based on an analysis of the power spectrum of the PDH error signal. This technique will be used in section 7.1.2 to determine to what fraction of its linewidth (set by its mirror properties) a cavity is locked to.

Second, a frequency beat measurement with a reference laser provides the possibility to (down-)convert optical frequencies to e.g. the radio frequency range. The reference laser should have a well-known linewidth, which is ideally less than the linewidth of the laser to be studied, and a well-known drift rate. Then, it is possible from a frequency beat measurement to determine information about the linewidth and drift rate of the laser of interest. This technique will be used in chapter 6 to determine the linewidths and drift rates of the lasers which are stabilized in the course of this thesis.

Third, the drift of a laser can be determined by performing Ramsey experiments with an atomic frequency reference. This scheme is also used in chapter 6 to be able to keep track of the drift of the reference laser during the frequency beat measurements.

### 3.3.1. Linewidth Estimation Based on the Spectrum of the PDH Error Signal

In the case of a laser, locked via the PDH locking scheme, the power spectral density (PSD) of the electrical error signal can be used to investigate the lineshape of the locked laser. According to Fourier analysis, a time-domain error signal can be decomposed into discrete frequencies and the PSD describes the distribution of power among those frequencies. Noise processes which affect the line shape of a locked laser can also be illustrated via a PSD, proportional to the PSD of the electrical error signal, and the linewidth of the laser is related to the shape of this PSD. The PSD of the locked error signal can be converted to frequency units by using the slope of the PDH error signal as a conversion factor from voltage deviation, measured with an oscilloscope, to frequency deviation. Schemes to estimate the laser linewidth from such a PSD are now presented.

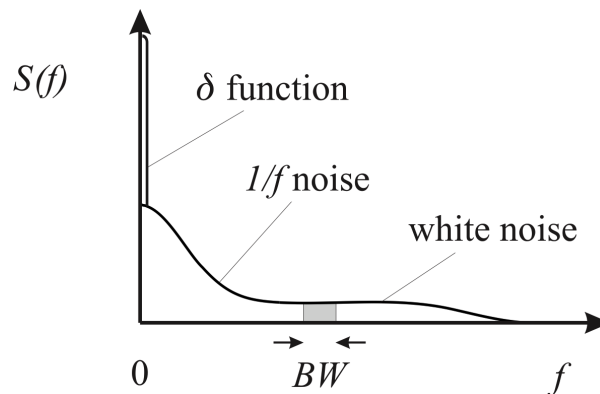


**Figure 3.10.:** Example of a PSD  $S(f)$  with three regimes:  $S(f)$  describes the power in each frequency band of bandwidth  $BW$ . Image taken from [59]

The PSD of frequency fluctuations  $S(f)$  for a laser can often be accurately modeled by a superposition of independent noise contributions [59], which can appear in the PDH error signal of the locked laser. Typically,  $S(f)$  shows three dominant regimes, which are illustrated in figure 3.10. First, near  $f = 0$  Hz a non-vanishing mean, i.e. a DC offset of the time-domain error signal, results in a delta function in the spectrum. Second, at higher frequencies a  $1/f$  dependence can be observed, which can be caused by technical noise, and in diode lasers is also caused by fluctuations of the charge carriers in the semiconductor (flicker frequency noise). Third, in the white noise regime,  $S(f)$  is no longer dependent on frequency and (due to energy conservation) it goes to zero eventually. Additionally, random walk frequency noise can appear in the spectrum, which has a  $1/f^2$  dependence, and is caused by disturbances from the environment, like temperature fluctuations and vibrations, as well as flicker phase noise and white phase noise (dependent on  $f$  and  $f^2$ ).

The PSD can be extracted from a time-domain signal via a Fourier transform. For a sampled signal  $x[n] = x(t = nT)$  ( $T$  is the sampling period), the relation between the Fast Fourier Transform (FFT) and PSD  $S(f)$  is given by [60]

$$S(f) = \frac{\text{FFT}\{x[n]\}\text{FFT}^*\{x[n]\}}{N^2} \quad (3.40)$$

### 3. Lasers and Laser Locking

where  $N$  is the number of points in the time-domain signal. Note, that the required normalization factor may differ, depending on which FFT algorithm is used. A good way to check this is to apply the FFT on a sine wave with known amplitude  $C$  and see which normalization factor provides the expected result. In a double-sided power spectrum, one should see 2 peaks of height  $C^2/4$ .

Performing an FFT algorithm provides a double-sided spectrum that displays half the energy at positive frequencies and half the energy at corresponding negative frequencies. The spectrum is therefore symmetrical around DC, where only the positive frequency part, the single sided spectrum, is usually given, to avoid redundancy. To obtain the single-sided spectrum, the power values corresponding to positive frequencies have to be multiplied by 2.

When performing an FFT on a time-domain signal, the frequency range and resolution of the spectrum depend on the sampling rate and the number of points measured. In a single-sided spectrum, the number of frequencies is  $N/2$ . The range of frequencies goes up to  $F_s/2$ , where  $F_s$  is the sampling frequency, i.e.  $N$  divided by the total time the time-domain signal was recorded for. The frequency resolution is  $\Delta_f = F_s/N$ . The FFT can also be thought of as a set of parallel filters of bandwidth  $\Delta_f$ , centered at each frequency.

#### Rectangular Noise Spectrum

Now two approaches to extracting the laser linewidth from  $S(f)$  are presented. First, the case of a rectangular noise spectrum (e.g. low pass filtered white frequency noise) is considered, based on a paper by Elliot et al. [61]. Here, the authors discuss the relation between the PSD of a laser and its linewidth and line shape. For a rectangular noise spectrum, the PSD has a constant value  $S_0$  up to a corner frequency  $B$  and is equal to 0 at higher frequencies. In general, the line shape of a laser can be described by a Voigt profile, which is a convolution of a Lorentzian and Gaussian distribution. If the PSD of a laser shows  $S_0/B \ll 1$  ( $S_0/B \gg 1$ ), the line shape of the laser can be approximated by a Lorentzian (Gaussian).

If the laser line shape can be approximated by a Lorentzian, then the laser linewidth is given by

$$\Delta_{\text{FWHM}} = \pi S_0 \quad (3.41)$$

where  $S_0$  can be estimated from a measured noise spectrum via

$$S_0 = \frac{D^2 V_{\text{RMS}}^2}{B}. \quad (3.42)$$

Here,  $D$  is the slope of the PDH error signal. The RMS value of a signal in the frequency domain can be found via Parseval's theorem [62]

$$V_{\text{RMS}} = \sqrt{\sum_m S(f)}. \quad (3.43)$$

The sum can be exchanged for an integral of the PSD over discrete frequencies  $m$  up to the cutoff frequency  $B$ .

### 3. Lasers and Laser Locking

If the laser line shape can be approximated by a Gaussian, the laser linewidth is given by:

$$\Delta_{\text{FWHM}} = 2\sqrt{2 \ln 2} DV_{\text{RMS}} \quad (3.44)$$

In summary, the PSD can be separated into two different regimes, which affect the line shape of a laser in a different way. In the case of  $S_0/B \ll 1$  the spectrum is constant over a wide frequency range (white noise). The associated line shape is a Lorentzian. In the other case, the contribution at low frequencies is large, which corresponds to a Gaussian lineshape. The Gaussian can be thought of as a Lorentzian randomly moving around a central frequency [59]. Consequently, the part which contributes to a broadening of the linewidth can be found at low frequencies in the PSD.

#### Arbitrary Noise Spectrum

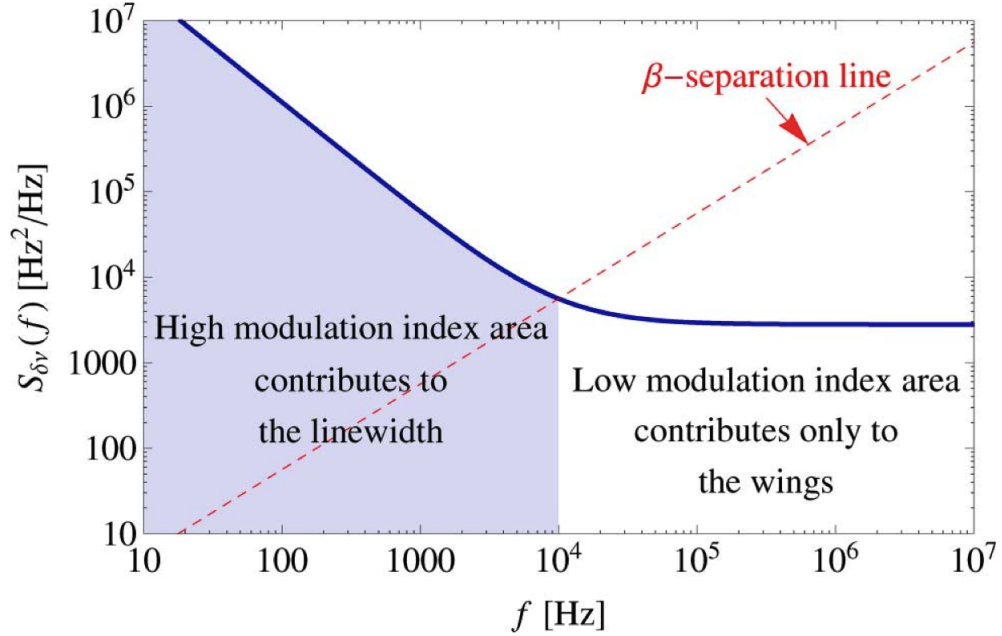


**Figure 3.11.:** Typical laser frequency noise spectrum showing frequency flicker noise ( $S(f) \propto 1/f$ ) at low frequencies and white noise ( $S(f) = \text{const.}$ ) at higher frequencies: Noise in the high modulation index regime contributes to the linewidth of the laser, whereas noise in the low modulation index area contributes only to the wings of the lineshape. Image taken from [63].

In reality, the shape of a laser's noise spectrum is not rectangular. An approach to extract the line shape and linewidth of a laser from an arbitrarily-shaped PSD is presented in [63]. Similar to before, the key here is to make a distinction between the two regimes of the PSD, which affect the lineshape in a different way. In this paper, the first regime is defined as  $S(f) > 8 \ln(2)f/\pi^2$ . Noise in this regime contributes to the laser linewidth, resulting in a Gaussian line shape. In the second regime, where  $S(f) < 8 \ln(2)f/\pi^2$  the noise contributes only to the wings of the line shape, but not the linewidth. This can also be understood in terms of frequency modulation theory. The laser can be thought of being

### 3. Lasers and Laser Locking

frequency modulated with different modulation indices<sup>2</sup> at each of the frequencies in the spectrum. In the first regime where  $S(f) > 8 \ln(2)f/\pi^2$ , the noise power is high compared to its Fourier frequency, which corresponds to a slow modulation with a high modulation index. In the second regime, the modulation is too fast (with small modulation index) to broaden the laser linewidth. The line separating the two regimes is referred to as the  $\beta$ -separation line. In figure 3.11 a schematic PSD and  $\beta$ -separation line is shown. One can see low frequency noise in the high modulation index part and white noise in the low modulation index part of the PSD. The laser linewidth can be approximated by

$$\Delta_{\text{FWHM}} = \sqrt{8 \ln(2)A} \quad (3.45)$$

where  $A$  is the total area between the PSD and the  $\beta$ -separation line, as given by the equation

$$A = \int_{1/T_0}^{\infty} H(S(f) - 8 \ln(2)f/\pi^2) S(f) df \quad (3.46)$$

where  $H(x)$  is the Heaviside function which is 0 for  $x < 0$  and 1 otherwise, and  $1/T_0 = F_s/N$  is the lowest measurable Fourier frequency.

In conclusion, the linewidth of a locked laser or locked cavity can be estimated via an analysis of the error signal spectrum. However, those approaches have a few flaws: First, the result relies heavily on an accurate measurement of the PDH error signal slope, which is not easy to determine when the error signal is very noisy. Second, these schemes don't account for the possibility that the reference-cavity or reference laser might be unstable. Third, in the case that there are peaks in the power spectral density of the error signal, these techniques provide wrong results as the peaks correspond to sidebands on the laser rather than this noise contributing to the linewidth (unless the peaks are at low frequencies - within the linewidth). Fourth, a linewidth result can be obtained that is too narrow due to systematic errors, e.g. contamination of the error signal due to ground loops or fiber noise. The servo system acts to correct these fluctuations which then don't show up in the locked error signal. But since they don't come from actual frequency fluctuations of the laser, the correction of the PID-controller will actually broaden the laser linewidth. Therefore, the error signal spectrum does not always provide an accurate representation of the actual frequency-stability of a locked laser or cavity.

#### 3.3.2. Frequency Beat Measurement

An approach to measuring the linewidth of a laser, that avoids many of the aforementioned limitations is to do a frequency beat measurement. When two lasers are superimposed on a photodetector, a beat note, i.e. a signal oscillating at the difference frequency, can be observed [46]. The electric field of the two lasers can be written as

$$E(t) = \sqrt{I_1} e^{i\omega_1 t} + \sqrt{I_2} e^{i\omega_2 t} \quad (3.47)$$

and the intensity can therefore be written as

$$|E(t)|^2 = I(t) = I_1 + I_2 + 2\sqrt{I_1 I_2} \cos((\omega_2 - \omega_1)t). \quad (3.48)$$

---

<sup>2</sup>The modulation index is defined as the ratio of frequency deviation to modulation frequency. Here it is given by the noise level compared to the corresponding Fourier frequency.

### 3. Lasers and Laser Locking

The beat signal, oscillating at  $\omega_2 - \omega_1$ , is usually chosen to be in the RF range which can be detected by a photodiode and visualized on a spectrum analyzer. By looking at the linewidth of the beat, an upper limit for the linewidths of the individual lasers can be estimated. The linewidth of the beat note will be larger than the linewidths of the individual lasers in the case that the phase noise of the two lasers is not correlated. As discussed earlier, the linewidth of a laser can be approximated by either a Lorentzian or Gaussian distribution. If the beat line shape can be approximated by a Lorentzian distribution, with standard deviation (=FWHM linewidth)  $\sigma_{\text{beat}}$ , the noise of the individual lasers adds up linearly [64]

$$\sigma_{\text{beat}} = \sigma_1 + \sigma_2 \quad (3.49)$$

where  $\sigma_1$  and  $\sigma_2$  are the FWHM linewidths of the individual lasers. In the case that the beat line shape can be approximated by a Gaussian distribution, the noise of the two lasers adds up quadratically [64]

$$\sigma_{\text{beat}}^2 = \sigma_1^2 + \sigma_2^2 \quad (3.50)$$

where the FWHM linewidth for the Gaussian distribution is given by  $2\sqrt{2\ln(2)}\sigma$ . To be able to determine the linewidth of one laser exactly, one can do a three-cornered hat beat measurement involving three independent lasers, i.e. lasers which have no correlations in their noise, where the linewidth of all three lasers is unknown. Or, if three independent lasers at the same wavelength are not available, it is sufficient to perform a beat measurement between two independent lasers, where one laser has a well-known linewidth, ideally less than the linewidth of the laser of interest. Note, the drift of the lasers with respect to each other can be measured by tracking the center of the beat note over some amount of time.

#### Frequency Comb

A beat measurement requires the availability of a reference laser with well-known linewidth and drift rate. One nice tool, which allows beat frequencies to be measured at various wavelengths, is a frequency comb [65]. In the frequency domain, a frequency comb possesses a broad optical spectrum consisting of millions of equally spaced comb teeth, as shown in figure 3.12b. In the time domain, according to Fourier analysis, this corresponds to a train of optical pulses. The frequency spacing of the comb teeth is inversely proportional to the time separation of the pulses.

The principle of operation of a frequency comb is usually based on a mode-locked laser, which can be used to produce short (on the order of femtoseconds) pulses. These pulses are spaced in the time domain by the round trip time of light in the cavity of the mode-locked laser. In a cw laser, the standing wave modes inside the laser cavity oscillate independently, i.e. the phases of the modes are random, which results in constant output power operation. In a mode-locked laser, however, the modes are locked in phase such that they interfere to give short pulses. Each time such an optical pulse hits the output mirror of the laser cavity, a fraction of the light leaks out, which generates a pulse train at the output.

Such a pulse train is shown in figure 3.12a. Each pulse consists of an envelope and carrier signal. From pulse to pulse, the carrier's phase advances with respect to the envelope

### 3. Lasers and Laser Locking

due to a small difference in group and phase velocity inside the laser cavity. Related to this phase shift per pulse  $\Delta\Phi$  is a ‘carrier envelope offset frequency’  $f_o$  of the frequency comb, if the comb teeth are extrapolated back to zero. One can then write the optical comb teeth frequencies  $\nu_n$  as

$$\nu_n = nf_r + f_o \quad (3.51)$$

where  $n$  is an integer and  $f_r$  is the repetition rate of the pulses, which is usually in the RF range. The carrier envelope offset frequency can be written as a function of the repetition rate as [66]

$$f_o \approx \frac{\Delta\Phi}{2\pi} f_r. \quad (3.52)$$

The repetition rate and carrier-envelope offset frequency drift with the laser cavity length, if not actively stabilized. Feedback can be applied to lock them to a frequency standard, e.g. a GPS signal or an optical clock. Due to phase noise present in RF references, the width of the comb teeth is in the MHz range, when locking the comb to an RF reference [65]. By using an optical reference, combined with fast intra-cavity feedback to e.g. an EOM, in our group comb teeth narrowed to approximately 1 Hz on a timescale of seconds can be achieved. Such an optical reference can be implemented by superimposing the comb light with a narrow laser on a photo diode, where the beat frequency between them is used as feedback to be kept constant.

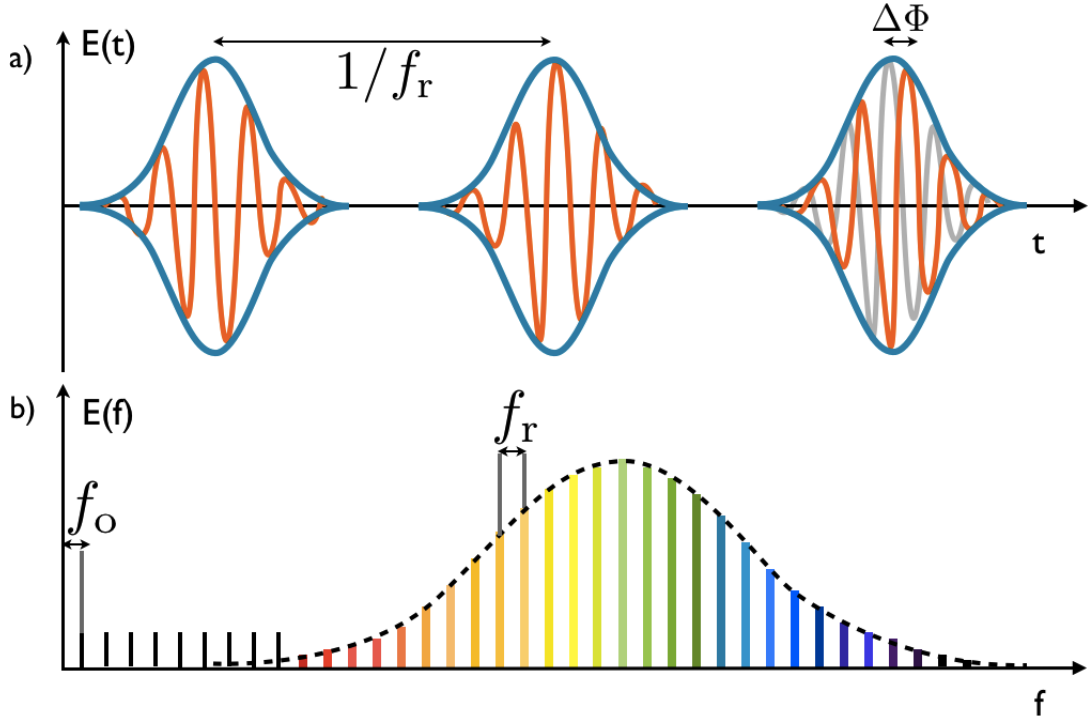


**Figure 3.12.:** a) Time-domain signal at the output of a mode-locked laser: The short pulses consist of an envelope (green) and carrier (orange), where the carrier’s phase advances by  $\Delta\Phi$  with respect to the envelope from pulse to pulse. b) In the frequency domain this pulse train corresponds to a comb, where the spacing of the comb teeth is inversely related to the time separation of the laser pulses.

### 3.3.3. Ramsey Experiment

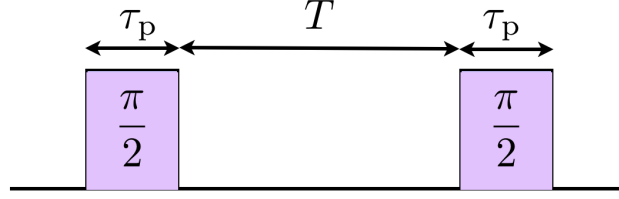


**Figure 3.13.:** Pulse sequence of a Ramsey experiment: For  $^{40}\text{Ca}^+$ , the first  $\pi/2$  pulse (which has a duration of  $\tau_p$ ) prepares the ion in a superposition of  $|S\rangle$  and  $|D\rangle$ . This is followed by a wait time  $T$ , during which the phase of the superposition evolves, before another  $\pi/2$  pulse is applied. After that, the quantum state of the ion is determined via a projective measurements onto one of the states  $|S\rangle$  or  $|D\rangle$ .

When performing a beat measurement involving two lasers, the beat frequency drifts with a rate that corresponds to the relative frequency drift between the two lasers. It is not possible from such a measurement to determine the absolute frequency drift of one of the lasers unless the drift of the second laser is known. A Ramsey experiment provides the possibility to measure the absolute frequency drift of a laser based on the use of an atomic frequency reference, e.g. an electronic transition of a trapped atomic ion [67]. The pulse sequence of a typical Ramsey experiment is illustrated in figure 3.13. In the case of using  $^{40}\text{Ca}^+$ , the trapped ion is initially prepared in the ground state  $|S\rangle$ , one of the  $4^2\text{S}_{1/2}$  Zeeman states. A “ $\pi/2$ ” laser pulse is applied, which prepares the ion in an equal superposition of ground and excited state, e.g.  $\frac{1}{\sqrt{2}}(|S\rangle + |D\rangle)$ , where  $|D\rangle$  is one of the  $3^2\text{D}_{5/2}$  Zeeman states. This is followed by a wait time  $T$  before another  $\pi/2$  pulse is applied. The quantum state is then measured via a projective measurement onto one of the two electronic states. During the wait time, the phase of the atomic superposition evolves at a rate given by the energy difference between ground and excited state.

The ion and the laser can be thought of as two oscillators, which ideally evolve at the same frequency, i.e. the laser keeps track of the phase of the ion. In the ideal case, where the laser is exactly on resonance with the atomic transition, the second  $\pi/2$  pulse will add to the first one for them in total to act as a “ $\pi$  pulse”. Such a  $\pi$  pulse will take the ion to the excited state  $|D\rangle$ . However, if the laser frequency is detuned by  $\delta$  from the atom, the two oscillators are running out of phase with each other. There is then the possibility of ending up in the ground state  $|S\rangle$  when performing a projective measurement after the second  $\pi/2$  pulse. The population in the excited state  $|D\rangle$  is given by [67]

$$\rho_{ee} = \left| \frac{\Omega\tau_p}{2} \right|^2 (\text{sinc}(\delta\tau_p/2))^2 \cos^2\left(\frac{\delta T}{2}\right) \quad (3.53)$$

where  $\Omega$  is the Rabi frequency of the pulses and  $\tau_p$  is the pulse duration. This expression consists of an envelope, the  $\text{sinc}^2$  part, and a fast oscillation, the  $\cos^2$  part, called Ramsey fringes. An example of such a Ramsey signal observed with a trapped  $^{40}\text{Ca}^+$  ion is shown in figure 3.14. The probability of ending up in the excited state after the measurement decreases with detuning until it reaches a first minimum where the  $\cos^2$  part is zero at  $\delta T = \pi$ . Here, the two oscillators are out of phase by  $\pi$ . If the wait time  $T$  is long and

### 3. Lasers and Laser Locking

known, small detunings  $\delta$  between the oscillators can be resolved. The drift of a laser can then be determined by tracking its detuning from the atomic transition frequency via Ramsey experiments. Note that in reality the atomic transition frequency can be sensitive to external fields, e.g. magnetic fields. Here, more sophisticated schemes can distinguish different effects.

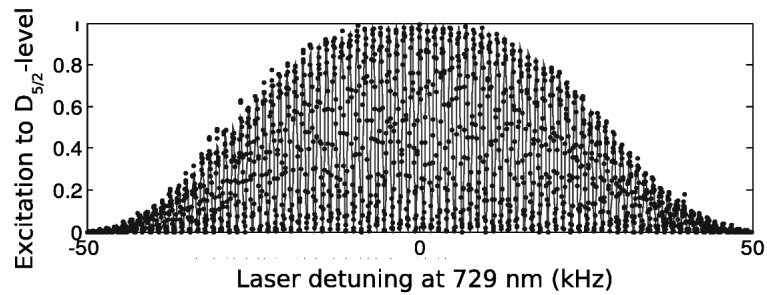


**Figure 3.14.:** Ramsey experiment with  $^{40}\text{Ca}^+$ . Image taken from [68]

## 4. A Transfer Lock for Cavity-Mediated Raman Transitions

As discussed in section 2.4, a cavity-mediated Raman process enables the implementation of a coherent light-matter interface for quantum networking. This process can be realized involving the  $4^2S_{1/2}$ ,  $4^2P_{3/2}$  and  $3^2D_{5/2}$  states in  $^{40}\text{Ca}^+$ , as shown in figure 2.9. A drive laser couples one arm of the Raman transition, from  $4^2S_{1/2}$  to  $4^2P_{3/2}$  and the ion couples to the cavity on the other arm of the Raman transition, from  $4^2P_{3/2}$  to  $3^2D_{5/2}$ , which triggers the generation of a single 854 nm photon.

There are requirements to how frequency-narrow and frequency-stable the two arms of the Raman transition, i.e. the Raman laser and cavity resonance frequency (set by the cavity length), should be. In order to provide this stability, the cavity-mediated Raman process needs to be frequency-stabilized via laser locking. In the following, our approach to implement this frequency-stabilization is presented as well as our experimental goals in terms of linewidths and drift rates.

### 4.1. Our Approach to Frequency-Stabilize the Cavity-Mediated Raman Process and Experimental Goals

The minimum linewidth of the Raman transition is set by the linewidth of the cavity around the ion (“ion-cavity”), which depends on the ion-cavity mirror properties. These will have certain transmissions  $T_1$  and  $T_2$ , as well as losses  $L_1$  and  $L_2$  which are related to the finesse of the ion-cavity via eq. 3.29. The mirror transmissions should be chosen such that photons can be sent out of the ion-cavity at a convenient rate  $\kappa$ , which is related to the finesse via eq. 2.39. The length of the ion-cavity should be short, in our case 2 cm, limited by the extent of the ion trap, such that a large atom-cavity coupling strength  $g$ , which is inversely proportional to the ion-cavity length (eq. 2.40), can be achieved. Given cavity length and finesse, the ion-cavity linewidth can be calculated via eq. 3.26, which we expect to be  $\sim 100$  kHz at 854 nm in our experiment. The length of the ion-cavity should be stabilized to a small fraction of this minimum linewidth, i.e. a few kHz or less.

The stabilization of the ion-cavity length can be achieved by locking it to a stable 785 nm “locking laser” via a PDH scheme. This wavelength is suitable as it is far away from any relevant transitions in  $^{40}\text{Ca}^+$ , which avoids AC Stark shifts, and is still somewhat similar to 854 nm, such that a high finesse coating of the ion-cavity mirrors at both wavelengths is feasible. At 785 nm, we expect the finesse of the ion-cavity to be a bit lower than at 854 nm.

#### 4. A Transfer Lock for Cavity-Mediated Raman Transitions

The 785 nm laser needs to be frequency-stabilized as well, and narrowed to a linewidth of a few kHz or less. This can be achieved by locking it to an external ultrastable reference-cavity, again via a PDH locking scheme. As previously mentioned, when locking a laser via the PDH scheme to a reference-cavity, locked laser linewidths a factor of 100 to 1000 times smaller than the reference-cavity linewidth can typically be achieved. In order to be able to narrow the 785 nm laser's linewidth to a few kHz, the linewidth of the reference-cavity should be around 100 kHz at this wavelength. Moreover, the FSR of the reference-cavity should be reasonably small such that double resonance of the 785 nm laser can be easily achieved between the ion-cavity (7.5 GHz FSR) and reference-cavity. Choosing a 10 cm long reference-cavity and requiring a linewidth of  $\leq 100$  kHz, means that the finesse of the reference-cavity at 785 nm should be  $\geq 15000$ .

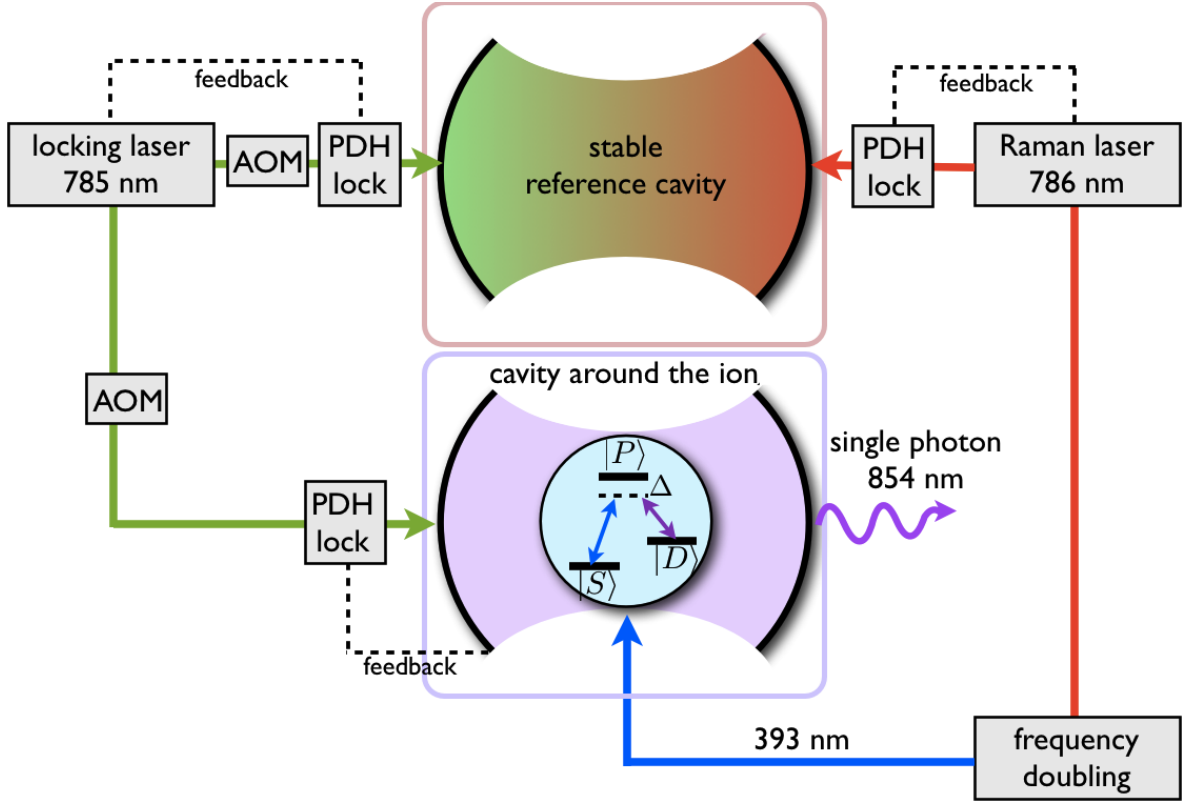


**Figure 4.1.:** Transfer lock scheme to frequency-stabilize the cavity-mediated Raman process: The Raman laser and ion-cavity are locked to one stable reference-cavity. This can be achieved by locking the length of the ion-cavity to a stable 785 nm laser via a PDH scheme. The 785 nm laser is locked to the reference-cavity, again via a PDH scheme. The 393 nm Raman laser light is generated in a frequency doubling process of light from a 786 nm laser where the fundamental is also PDH locked to the reference-cavity. The reason why the Raman laser (fundamental) and cavity locking laser are stabilized to the same reference-cavity, is that it allows the resonance condition of the Raman transition to be maintained over many hours. The AOMs shown in the image allow for obtaining double resonance of the 785 nm laser between the two cavities as well as double resonance in the ion-cavity with the 785 nm locking laser and a 854 nm reference laser. This reference laser (not shown) is used to find the correct detuning of the ion-cavity from the  $4^2P_{3/2} \leftrightarrow 3^2D_{5/2}$  transition.

#### 4. A Transfer Lock for Cavity-Mediated Raman Transitions

Next, the 393 nm Raman laser needs to be narrowed also to a small fraction of the ion-cavity linewidth, i.e. a few kHz or less. The 393 nm Raman laser light can be generated in a frequency doubling process of light from a 786 nm laser where the fundamental at 786 nm is also locked via a PDH locking scheme to a reference-cavity.

There are also requirements to the relative stability of the two arms of the Raman transition. The ion-cavity length and the drive laser frequency have to satisfy the resonance condition of the Raman transition, i.e. the detuning of the ion-cavity from the  $4^2P_{3/2} \longleftrightarrow 3^2D_{5/2}$  transition has to match the detuning of the 393 nm drive laser from the  $4^2S_{1/2} \longleftrightarrow 4^2P_{3/2}$  transition, to ensure complete population transfer. In order to avoid a relative drift between the two arms of the Raman transition, the frequencies of the laser and ion-cavity mode have to be relatively stable, within the linewidth of the Raman transition, such that the Raman condition is maintained on a long timescale. Expected timescales for quantum network experiments are several hours. In order to maintain the Raman transition over many hours, the Raman laser (fundamental) and ion-cavity locking laser are stabilized to the same reference-cavity. Drifts of the reference-cavity affect the Raman laser fundamental and ion-cavity to first order equally<sup>1</sup>, and the Raman condition is maintained. This “transfer lock” technique is already used successfully in another cavity experiment in our group [12].

Moreover, the frequencies of the Raman laser and ion-cavity resonance also have to be absolutely stable. If both arms of the transition drift equally by a large amount, the Raman condition is maintained, but the frequency of the generated photons will change. In quantum network experiments involving another trapped ion node this can be a problem, as the photon frequency should ideally match the frequency of the remote cavity, e.g. in order to be able to be absorbed at the other node. Therefore, the two locked laser systems should drift no more than 1 Hz/s.

In summary, our approach to stabilizing the cavity-mediated Raman process is a transfer lock scheme, which is illustrated in figure 4.1. Based on suitable mirror properties for planned quantum network experiments, the desired linewidth of our ion-cavity is approximately 100 kHz at 854 nm. The locking laser at 785 nm and Raman laser fundamental at 786 nm should be locked to a small fraction of that, i.e. a few kHz or less. The minimum drift rate of the lasers is limited by the drift rate of the ultrastable reference-cavity. In order for the photon frequency not to change too much over the course of many hours during long quantum network experiments, a drift rate of less than 1 Hz/s is desired.

---

<sup>1</sup>The Raman laser drifts a factor of two faster, due to frequency doubling. Furthermore, when the Raman laser fundamental and ion-cavity locking laser are locked to two different modes of the reference-cavity, the modes drift in the same direction but the mode spacing also changes by a small amount with a change in reference-cavity length. Considering our reference-cavity (see section 5.2) with initial length  $L = 10$  cm and stability parameters  $g_1 = 1$  and  $g_2 = 1 - L/0.5$  and two modes at 785 nm and 786 nm, respectively, the change in frequency spacing of these two modes as a result of a change in cavity length can be calculated via eq. 3.11. This change in mode spacing is on the order of 0.02 Hz when the 785 nm mode drifts by 1 Hz and is thus negligible.

# 5. Experimental Setup of the Transfer Lock

In this chapter the experimental setup of our transfer lock is presented. The first part of the chapter is concerned with our ultrastable reference-cavity, the center piece of the transfer lock. The reference-cavity was put inside a vacuum chamber and then the finesse at wavelengths around 785 nm and 729 nm<sup>1</sup> was determined. In the second part of the chapter the locking setup for the two lasers involved in the transfer lock is presented.

## 5.1. Reference-Cavity and Vacuum Chamber Assembly

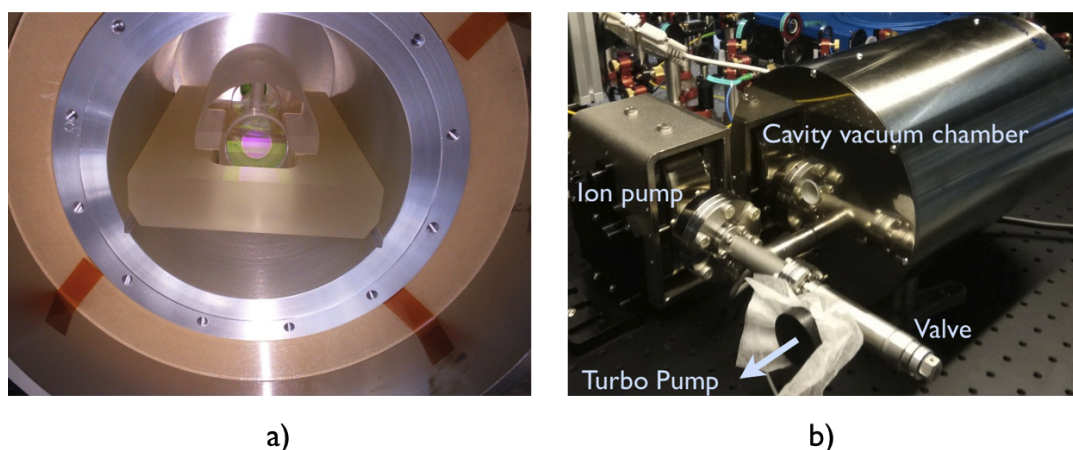


**Figure 5.1.:** a) Reference-cavity on the Zerodur mounting block inside the vacuum chamber with open front flange. b) Vacuum chamber of the reference-cavity connected to a all-metal valve and ion pump.

The reference-cavity for the frequency-stabilization of the cavity-mediated Raman process was supplied by Stable Laser Systems (SLS). The cavity spacer and mirrors are made from ULE and are optically contacted together. The cavity is provided with a vacuum housing with access from both sides, an all-metal valve<sup>2</sup>, an ion pump<sup>3</sup> and temperature controller<sup>4</sup>. As presented in section 3.2.1, a temperature-stabilized ULE cavity in vacuum provides a frequency reference with high short-term stability. Putting a cavity in vacuum

<sup>1</sup>This reference-cavity was additionally coated for 729 nm light, such that it can serve also as a reference to lock a laser on the  $^{40}\text{Ca}^+$  qubit transition.

<sup>2</sup>Kurt J. Lesker Company CR20

<sup>3</sup>GammaVacuum S25

<sup>4</sup>Wavelength Electronics LFI-3751

## 5. Experimental Setup of the Transfer Lock

reduces changes in the optical path length due to pressure and temperature fluctuations and acoustic noise.

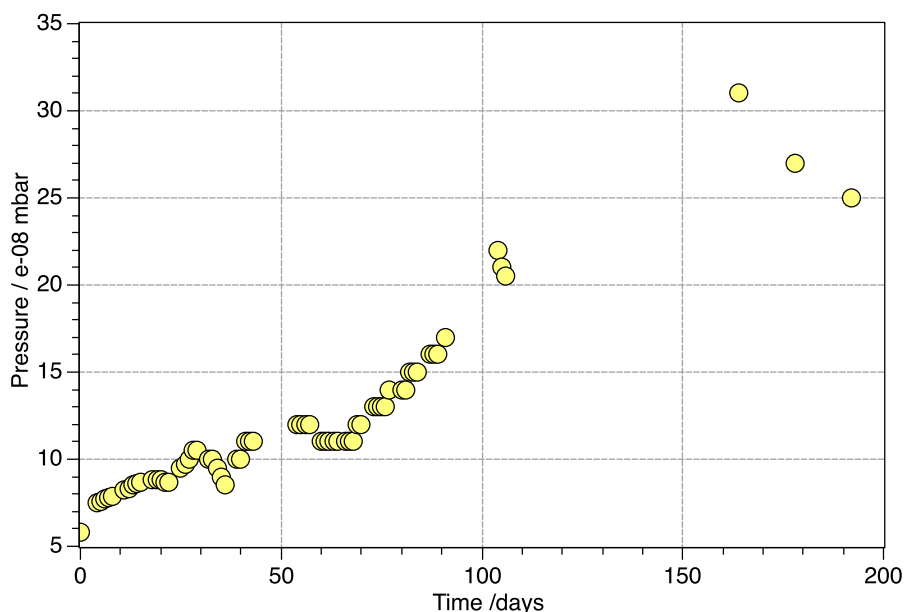


**Figure 5.2.:** Pressure inside the reference-cavity vacuum chamber over a few months: The pressure values were measured by the ion pump, which determines a current related to the pressure in the chamber. Day 0 in this graph represents the day when a leak in the vacuum chamber had formed. The pressure has stabilized in the  $10^{-7}$  mbar range.

Before opening the front flange of the vacuum chamber and inserting the cavity, the chamber was attached via CF flanges to a pump station<sup>5</sup> via the metal valve and to the ion pump, as shown in figure 5.1b (turbo pump not shown). First, the air was pumped out using a regular copper gasket (CF16) when connecting the chamber to the turbo pump to perform a helium leak test. A small leak was found at the viewport connection of the KF front flange of the vacuum chamber, such that the front flange had to be replaced.

When putting a cavity in vacuum, it is recommended that air should be pumped out of the vacuum chamber very slowly to reduce the chance that dust will be stirred up and deposited onto the cavity mirrors, which would reduce the finesse. Therefore, after receiving a new front flange for the chamber, the copper gasket was exchanged with a copper plate with a 0.34 mm diameter hole. Using the regular copper gasket, a pressure in the vacuum chamber of  $8.6(1) \cdot 10^{-6}$  mbar had been achieved after approximately 3 minutes. The same pressure was achieved using the pinhole gasket in approximately 1 hour due to the greatly reduced pumping speed. Next, the cavity was inserted into the chamber, which is shown in figure 5.1a. The cavity rests on four Viton balls on a Zerodur mounting block, which reduces thermal coupling and damps vibrations.

The vacuum chamber was pumped out, first through the pinhole for a few minutes. Then the valve was closed and the pinhole gasket was replaced with a regular gasket. The pump was started again, the valve was reopened and the chamber was pumped out until a pressure of  $2.2(1) \cdot 10^{-7}$  mbar was reached. At this point, the valve was closed and the

<sup>5</sup>Pfeiffer Vacuum TMU 071 P turbo pump

attached ion pump was switched on. The pressure went down continuously over 4 months to  $5.8(1) \cdot 10^{-8}$  mbar. The pressure in the chamber had been going up since then, likely due to the formation of another leak, and has then stabilized, as shown in figure 5.2. The pressure is still in the  $10^{-7}$  mbar range which should suffice for keeping the cavity stable.

## 5.2. Reference-Cavity Characteristics

### 5.2.1. Zero-Crossing Temperature

Since the resonance frequency of a cavity changes with temperature (the ULE material expands and contracts when exposed to temperature changes), it is important to temperature-stabilize the reference-cavity. Around a certain temperature, the ULE glass spacer of the cavity has a near zero linear coefficient of thermal expansion, which describes how much the cavity length changes when the temperature changes. This “zero-crossing” temperature was determined by SLS via a laser frequency beat measurement. Here, they locked a laser to the reference-cavity and changed the cavity temperature while observing the beat frequency with a stable reference laser. The data is shown in figure 5.3. The zero-crossing temperature was measured to be  $(32.7 \pm 1)^\circ\text{C}$ , the temperature at which the minimum of the orange polynomial fit in figure 5.3 occurs. At this temperature the derivative of the beat frequency with respect to temperature becomes zero. The cavity is kept at this zero-crossing point by stabilizing it with a commercial PID-controller in combination with heaters inside the vacuum chamber. In section 6.2 the residual drift rate of the cavity at the zero-crossing temperature is presented, which is  $202(1)$  mHz/s.

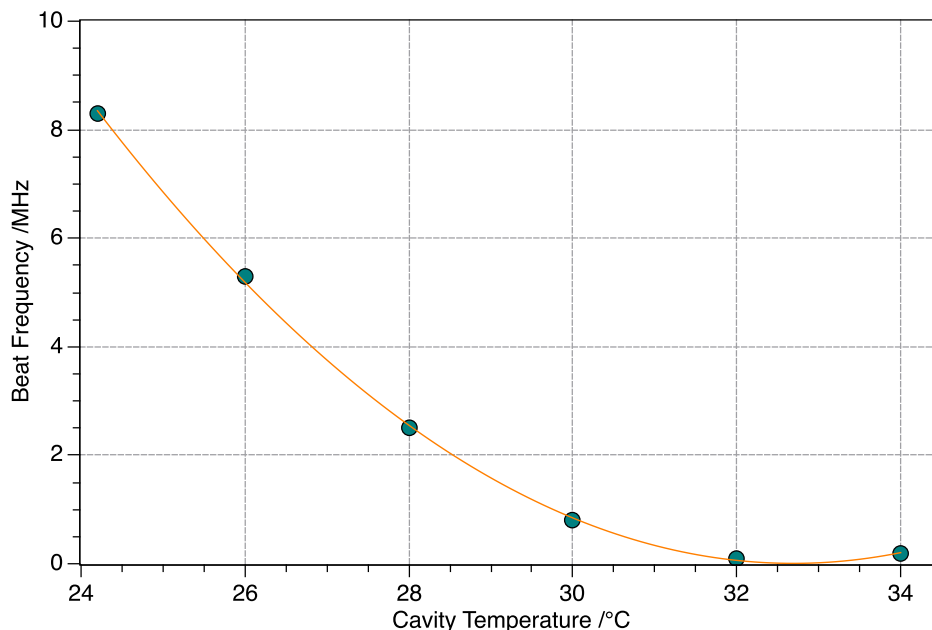


**Figure 5.3.:** Measurement of the beat frequency of a laser locked to our reference-cavity with a stable reference laser, to determine the zero-crossing temperature of the reference-cavity spacer. This data was provided by the manufacturer (SLS).

### 5.2.2. Geometry

The reference-cavity is a horizontal notch cavity with one planar/planar and one concave/planar mirror, which has a radius of curvature of  $r_{c,2} = 50$  cm. The mirrors are optically contacted to a  $L = 10$  cm ULE spacer, as shown in figure 5.4. This configuration, of one flat and one curved mirror, is sometimes referred to as a half-symmetric cavity. A 10 cm mirror spacing corresponds to a free spectral range of 1.5 GHz. In the following, the spatial properties of the Gaussian cavity modes are calculated.

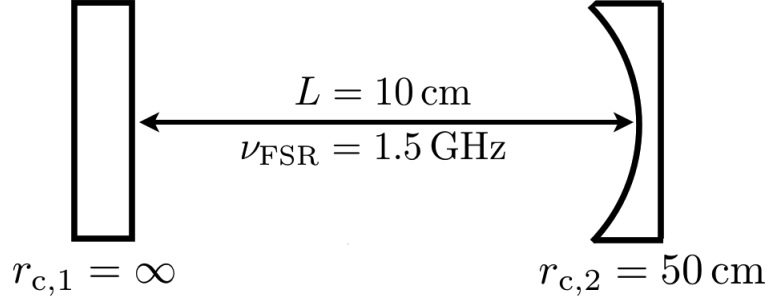


**Figure 5.4.:** Reference-cavity geometry: The cavity consists of a planar/planar and concave planar mirror, with a spacing of  $L = 10$  cm.

The stability parameters for the reference-cavity are  $g_1 = 1$  and  $g_2 = 0.8$  (eq. 3.3). For a half-symmetric cavity the beam radius  $w_1$  at the planar mirror has to be equal to the beam waist  $w_0$  to ensure that the curvature of the wave front, which approaches infinity at the beam waist, matches the mirror's curvature. From equations 3.7 and 3.8, the beam waist and curved mirror beam radius can be calculated. Some Gaussian beam properties of the modes of the reference-cavity at 785 nm and 729 nm are provided in table 5.1.

**Table 5.1.:** Gaussian beam properties of the modes of our reference-cavity at 785 nm and 729 nm.

Wavelength	785 nm	729 nm
Beam waist $w_0 = w_1$	224 $\mu\text{m}$	215 $\mu\text{m}$
Beam radius (at curved mirror) $w_2$	250 $\mu\text{m}$	241 $\mu\text{m}$
Rayleigh range	19.98 cm	20.00 cm

When using a fiber coupler which provides a 1.45 mm collimated beam diameter, the focal length of the lens required to achieve a waist similar to 224  $\mu\text{m}$  can be calculated via equation 3.13. A lens of focal length  $f = 400$  mm e.g. provides a beam waist of 244  $\mu\text{m}$ . Such a lens is used to mode match the laser light to the cavity mode, as presented in the optical setup in section 5.4.1.

The resonance frequencies of the axial and transverse modes of the reference-cavity can be calculated using eq. 3.12. The frequency spacing  $\Delta\nu$  between two adjacent transverse modes is 221 MHz.

### 5.2.3. Mirror Properties

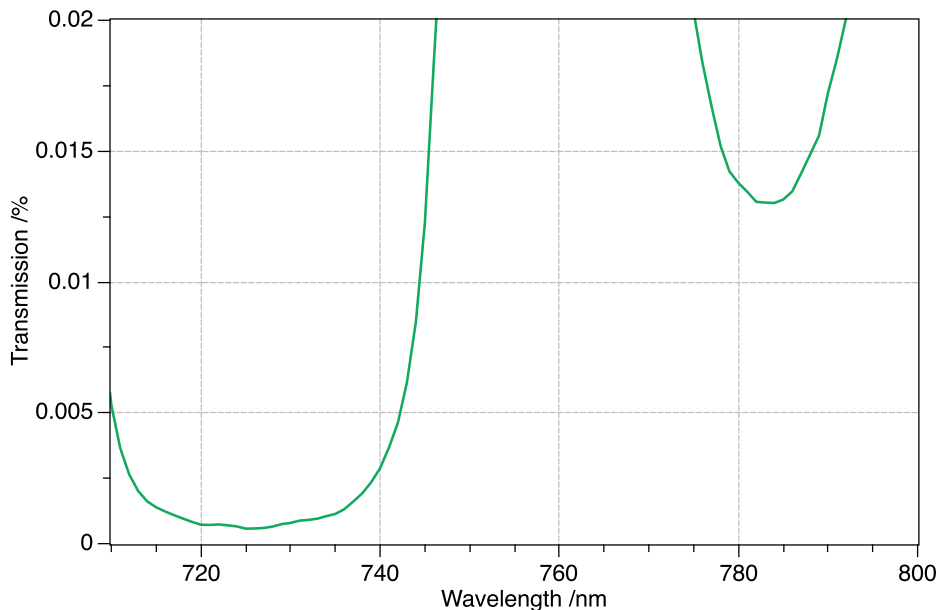


**Figure 5.5.:** Transmission of one of the reference-cavity mirrors as a function of wavelength. This data was provided by the manufacturer (SLS).

The cavity mirror substrates have a super-polished finish and were coated by Advanced Thin Films (ATF) with a high-finesse coating at both 785 nm and 729 nm. The cavity linewidth and thus the finesse limits how well a laser can be locked to the cavity at a certain wavelength using the PDH laser locking scheme. Since our lasers at 785 nm should be locked to a linewidth of a few kHz or less for the transfer lock, a target finesse of 15000-30000<sup>6</sup> was chosen which corresponds to a cavity FWHM linewidth of 50 – 100 kHz. Additionally, the mirrors were coated for 729 nm light because it is convenient to have a high-finesse cavity available to lock a laser on the  $^{40}\text{Ca}^+ |S\rangle \longleftrightarrow |D\rangle$  optical qubit transition wavelength. Since the lifetime of the metastable  $|D\rangle$  state is approximately 1 s, the linewidth of the 729 nm laser should be below 1 Hz. This ensures that the qubit’s coherence is limited by the lifetime of the excited state and not the laser. A target finesse of  $> 200000$  was requested by us at 729 nm which corresponds to a cavity linewidth of  $< 7.5$  kHz. In comparison, the QSim team<sup>7</sup> uses a reference-cavity with a linewidth of 4.8 kHz to achieve a laser linewidth of their Ti:Sa laser of approximately 1 Hz on a timescale of seconds at 729 nm [69].

The mirror transmission spectrum for our reference-cavity mirrors in figure 5.5 was measured by SLS. According to their measurements, at 785 nm a transmission of 132 ppm was achieved and at 729 nm a transmission of 8 ppm was achieved.

<sup>6</sup>Here, an upper limit was chosen as it might be tricky to lock a laser to a very narrow reference-cavity, because then also on very short timescales the laser linewidth is broader than the cavity linewidth. Sometimes, in such a case a two-stage stabilization process is necessary, where the laser is first locked to a medium-finesse cavity, and then to a high-finesse cavity.

<sup>7</sup>The QSim team is another team in our group, which works on quantum simulations. Their experiments is located in the same lab at IQOQI (lab 1) as our experiment.

## 5. Experimental Setup of the Transfer Lock

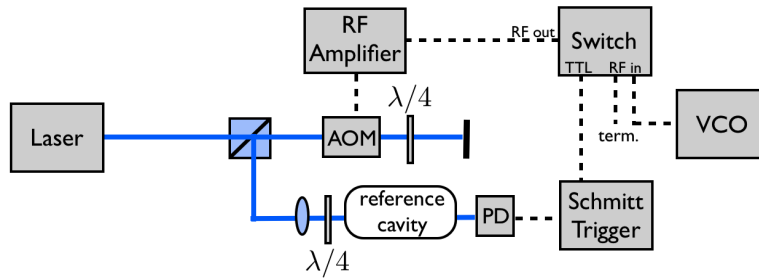


**Figure 5.6.:** Setup for the cavity ringdown measurements: The laser light is sent to the reference-cavity after being diffracted at an AOM in double pass configuration. This AOM is supplied with an RF signal from an RF amplifier in combination with a voltage-controlled oscillator (VCO). The photodiode (PD) detects the light transmitted at the cavity. Once the light in transmission exceeds a threshold, the Schmitt trigger switches from the VCO connected switch input to a terminated input (term.) which results in no RF signal arriving at the RF amplifier anymore.

To determine the finesse, the cavity ringdown method, which was discussed in section 3.2.1, was used. The ringdown setup is illustrated in figure 5.6. Here, laser light diffracted at an AOM in double pass configuration is sent to the reference-cavity. The laser frequency is scanned over the resonance of a  $TEM_{00}$  cavity mode (by applying a triangle voltage to move a mirror inside the laser cavity) and once the transmitted light, detected by a photodiode, exceeds a certain threshold, the light is rapidly switched off (on a timescale of approximately  $0.5 \mu s$ ). This switch was achieved via a Schmitt trigger, connected to the photodiode. The Schmitt trigger switches off the RF signal going to the AOM and as a result light is not diffracted anymore. The light which is stored in the cavity then leaks out in an exponentially decaying manner according to eq. 3.27, where the time constant of the decay is related to the finesse via eq. 3.28. An example for such a ringdown signal of our reference-cavity is shown in figure 5.7 at a wavelength of 726 nm.

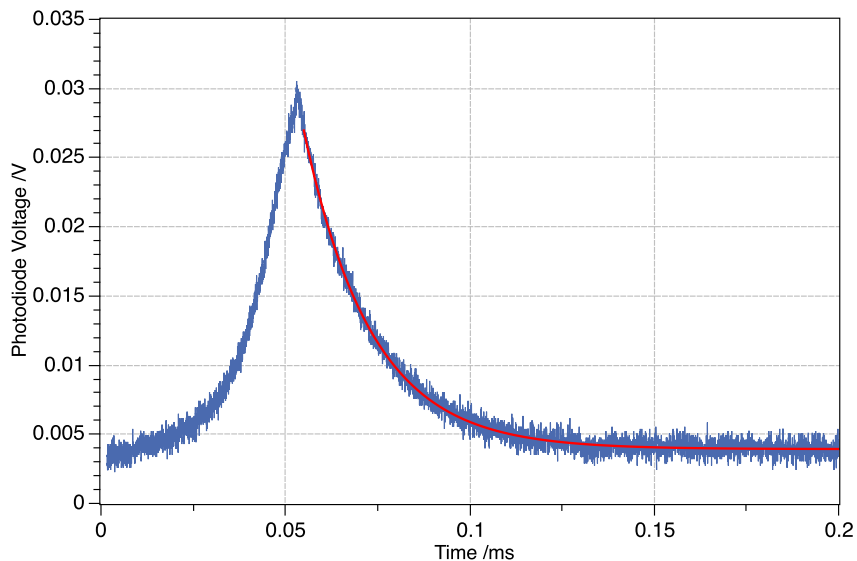


**Figure 5.7.:** Reference-cavity decay at approximately 726 nm. The red line corresponds to an exponential fit of the form  $I(t) = I_0 e^{-(t-t_0)/\tau} + c$ , where the decay constant  $\tau$  can be related to the finesse.

## 5. Experimental Setup of the Transfer Lock

**Table 5.2.:** Mirror transmission, finesse and cavity linewidth at approximately the wavelengths of interest: The wavelength of the cavity locking laser at 785 nm, the wavelength of the fundamental of the 393 nm Raman laser at 786 nm and the wavelength of the qubit transition at 729 nm.

Wavelength /nm	784.8	785.8	728.9
Transmission /ppm	$\sim 132$	$\sim 135$	$\sim 8$
Finesse	22600(500)	21300(300)	161000(2000)
Cavity linewidth /kHz	66(2)	70(1)	9.3(1)

The finesse of the reference-cavity at various wavelengths was measured via cavity ring-down measurements using a widely tunable Ti:Sa laser. The finesse results around 785 nm and 729 nm are shown in figure 5.8 and 5.9 and the results close to wavelengths of interest are given in table 5.2. The error bars result mainly from the error when fitting an exponential decay function to the oscilloscope data as well as the uncertainty in cavity length (an uncertainty of 100  $\mu\text{m}$  was assumed). At 784.8 nm a finesse of 22600(500) was achieved and SLS promised a finesse between 15000 and 30000, which means that the target was met. At 728.9 nm a finesse of 161000(2000) was achieved and the target of  $>200000$  was not met. Given the mirror transmission in figure 5.5, assuming  $T_1 = T_2$ , eq. 3.29, which relates the finesse  $F$  to the sum of total roundtrip losses  $T_1 + T_2 + L_1 + L_2$  in the cavity, can be used to estimate mirror losses  $L_1 + L_2$ . The results are  $(L_1 + L_2) \approx 15$  ppm at 785 nm and  $(L_1 + L_2) \approx 25$  ppm at 729 nm. Assuming wavelength-independent mirror losses, it is then possible to calculate an expected finesse curve using eq. 3.29 based on the transmission curve from figure 5.5, which is shown as the orange curve in figure 5.8 and 5.9. The data and theory curves are shifted with respect to each other. We believe that the measurements carried out by ATF/SLS are off by approximately 5 nm. Our wavemeter was confirmed to not be inaccurate by more than a few 100 MHz by comparing it with the QSim team's wavemeter, calibrated with an ion. Josef Schupp from our team has also seen shifts in the coating data from ATF when characterizing prospective mirrors for our ion-cavity.

## 5. Experimental Setup of the Transfer Lock

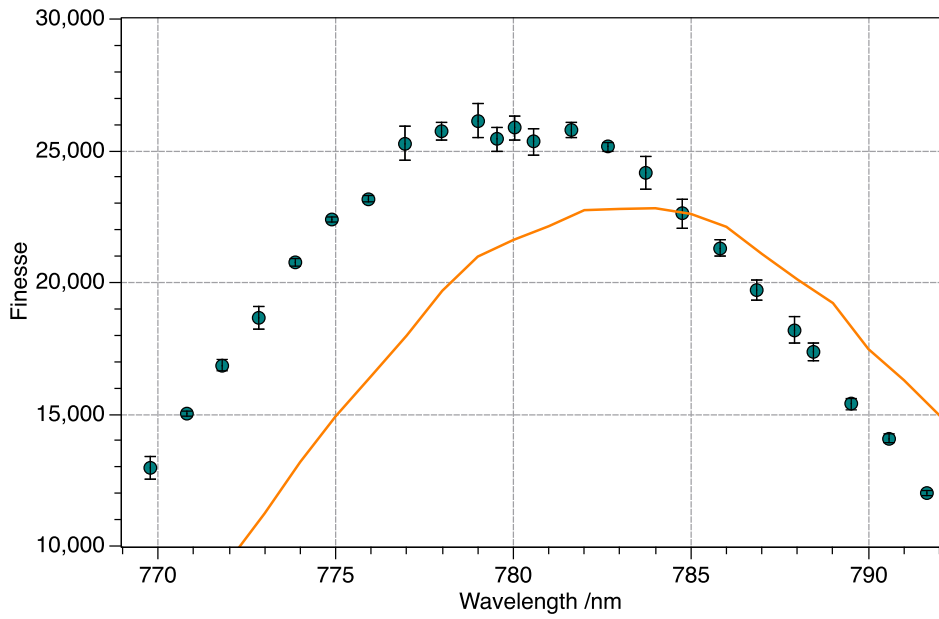


**Figure 5.8.:** Finesse of our reference-cavity around 785 nm: The cavity ringdown signal was measured with an oscilloscope (Teledyne Lecroy Wavesurfer 3024) at different wavelength values. The finesse values at these wavelengths (green points) were determined from the time constant of the cavity decay via eq. 3.28. The finesse error bars result from the uncertainty when fitting an exponential decay to the ringdown data as well as the uncertainty in reference-cavity length. The orange curve represents an expected finesse curve based on the mirror transmission data from figure 5.5 and eq. 3.29.

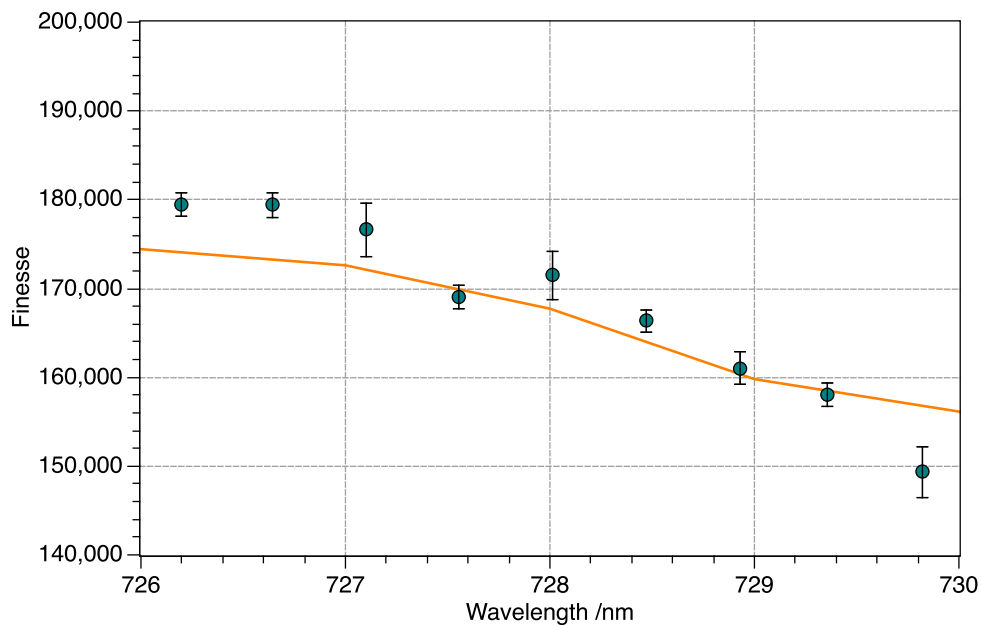


**Figure 5.9.:** Finesse of our reference-cavity around 729 nm.

## 5.3. Lasers

### 5.3.1. Ion-Cavity Locking Laser

A Toptica DL pro diode laser at 785 nm is used as the laser which locks the length of the ion-cavity in the transfer lock. It is controlled via a digital DLC pro laser controller. Toptica specifies the free running linewidth as 100 kHz over  $5 \mu\text{s}$ , which results from the frequency-selective feedback via the ECDL grating. The grating can be coarsely tuned via a screw and fine-tuned via adjusting the voltage to the piezo on which the grating is mounted. The total tuning range of the laser is specified to be approximately 40 nm with a mode-hop-free tuning range between 20 and 50 GHz. The maximum output power was measured by us with a powermeter to be around 120 mW at 785 nm. When locking the diode laser, feedback can be applied to the grating piezo, to compensate slow drifts, and to the injection current to narrow the laser linewidth.

### 5.3.2. Raman Laser

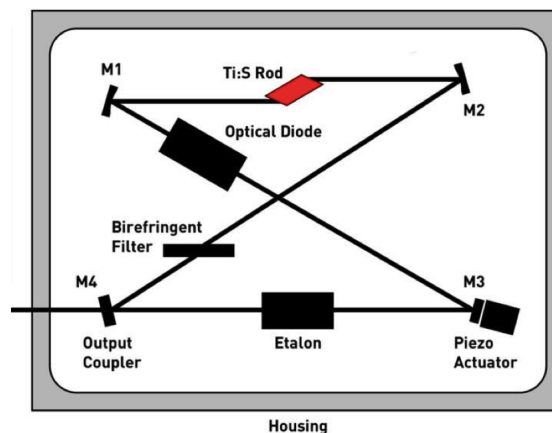


**Figure 5.10.:** Msquared Ti:Sa laser bow-tie cavity: The cavity consists of four mirrors M1 to M4, where one mirror (M3) is mounted on a dual-stack piezo and thus movable. The cavity contains the Ti:Sa crystal (red), an optical diode, a birefringent filter and an etalon. Image taken from [47]

For the 393 nm Raman laser, an MSquared Solstis-1600-PSX-R Ti:Sa laser is used, where the fundamental is tuned to 786 nm. In combination with an MSquared ECD-X external cavity resonant doubler accessory module, the light is frequency doubled to 393 nm. The tuning range of the fundamental is specified as 725 – 875 nm, limited by the coating of the cavity mirrors. Therefore, the MSquared Ti:Sa laser can also be tuned and locked to the  $^{40}\text{Ca}^+$  qubit transition frequency at 729 nm. The laser can be controlled via the ICE-Bloc (Instrument Control by Ethernet) and a computer user interface. The free running linewidth of the laser is specified as  $< 100 \text{ kHz}$  over  $100 \mu\text{s}$ . The long term drift is strongly dependent on lab conditions (temperature, pressure) but a typical value, according to MSquared, for the free running frequency drift is 100 MHz/hr. The laser is

## 5. Experimental Setup of the Transfer Lock

optically pumped via a Lighthouse Photonics Sprout laser operating at 532 nm with a power of 8 W. This results in a maximum output power in the infrared of roughly 2.5 W and in the blue 1 W (measured by us with a powermeter). The laser cavity is in a bow-tie configuration, as shown in figure 5.10, which contains the Ti:Sa crystal, an optical diode and three frequency-selective elements: a birefringent filter, an etalon and a movable cavity mirror. A coarse wavelength adjustment can be made by rotating the birefringent filter. The etalon allows for single-mode operation, as it introduces a spectral loss that is a much more narrow function of frequency than the spectral loss introduced by the birefringent filter. The etalon spacing can be adjusted via the computer interface, which results in the laser oscillating on one specific longitudinal mode of the bow-tie cavity. The etalon can then be locked to this longitudinal mode by dithering the etalon spacing at a frequency of 19 kHz. One of the mirrors (M3, figure 5.10) inside the laser cavity is mounted on a dual stack piezo, which allows for fast and slow feedback, with a bandwidth of up to  $\sim 100$  kHz (limited by a strong resonance of the piezo), for frequency-stabilization of the laser and linewidth narrowing.

### 5.4. Optical and Electronic Setup of the Transfer Lock

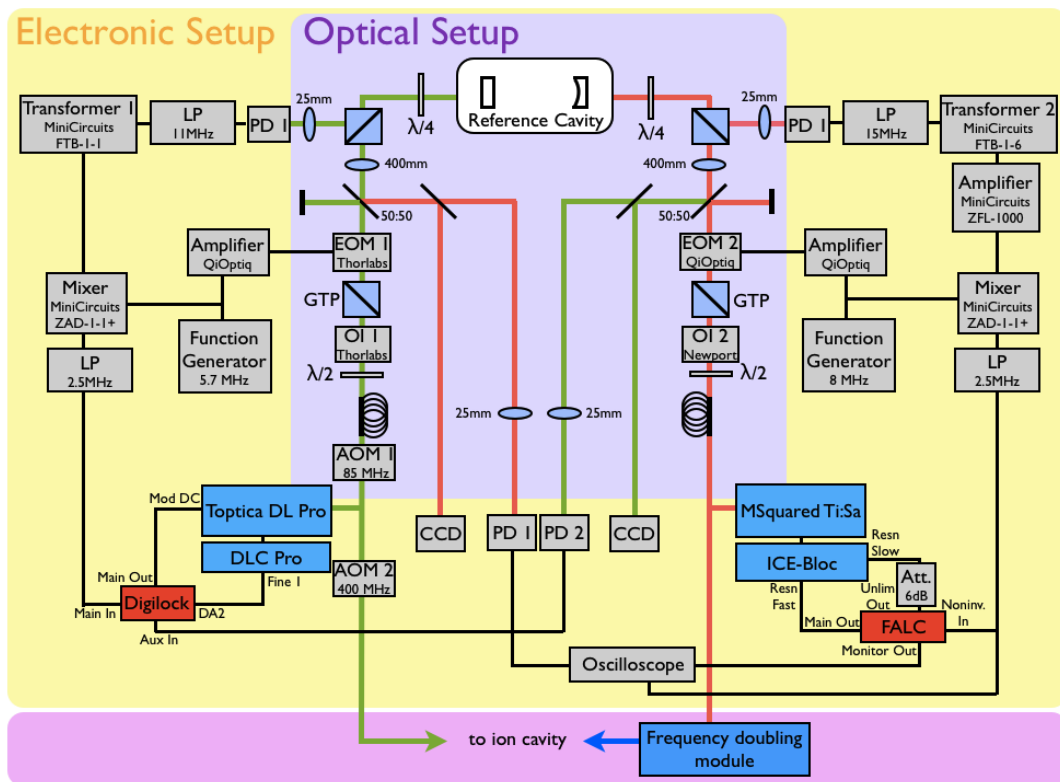


**Figure 5.11.:** Optical (purple) and electronic (yellow) setup of the MSquared Ti:Sa and diode laser locks: The light (orange, green) from the two lasers (blue) is sent through the optical setup. The electronic setup is used to lock the two lasers to the reference-cavity from two opposite sides. The following abbreviations are used in the figure: optical isolator (OI), Glan Thompson Polarizer (GTP), electro-optic modulator (EOM), photodiode (PD) and low pass filter (LP). The pink part of the image shows the future path to the experiment.

## 5. Experimental Setup of the Transfer Lock

### 5.4.1. Optical Setup

Shown in purple in figure 5.11 and in figure 5.12 is the optical setup of the transfer lock. The light from the two lasers enters the reference-cavity from opposite sides. In each case, the light first goes through a fiber<sup>8</sup> (1.45 mm output coupler<sup>9</sup>), through a  $\lambda/2$ -plate<sup>10</sup>, an optical isolator<sup>11</sup> and a Glan Thompson polarizer (GTP)<sup>12</sup>. The GTP, which provides linearly polarized light with high purity, in combination with the  $\lambda/2$ -plate can be used to adjust the intensity of the light going to the cavity (tens of  $\mu\text{W}$ ). The optical isolator reduces etalon effects and avoids light being reflected back into the laser<sup>13</sup>. The GTP is adjusted such that the light polarization is matched as well as possible to the crystal axis of the EOM to reduce RAM (as presented in section 3.2.2). Two different EOMs are used in the path of the diode laser (EOM 1<sup>14</sup>) and MSquared Ti:Sa laser (EOM 2<sup>15</sup>). After going through the EOM, the light passes a 50:50 beam splitter, the lens<sup>16</sup> for mode matching to the cavity<sup>17</sup>, a polarizing beam splitter (PBS), and finally a  $\lambda/4$ -plate, which changes the light polarization from linear to circular. The light which is reflected by the cavity passes the  $\lambda/4$ -plate again which changes the polarization back to linear, but now orthogonal to the initial linear polarization. This light is then reflected at the PBS and detected by a fast photodiode<sup>18</sup> for laser locking. The light which is transmitted by the cavity is converted back to the initial linear polarization via the  $\lambda/4$ -plate on the other side, passes the PBS and is reflected onto a photodiode<sup>19</sup> and CCD camera<sup>20</sup> via a 50:50 beam splitter.

### 5.4.2. Electronic Setup

For phase modulation, the EOMs are driven with the signal from a function generator<sup>21</sup> at 5.7 MHz and 8 MHz (EOM 1 and EOM 2, respectively). The signal is amplified<sup>22</sup>, where the frequency range over which the signal can be amplified has a bandwidth of 7

---

<sup>8</sup>Thorlabs P3-780PM-FC-2 (FC/APC, PM at 780 nm, length 2 m)

<sup>9</sup>Schäfer+Kirchhoff fiber collimator 60FC-M8-10, AR coated 630 – 980 nm

<sup>10</sup>CeNing waveplates (zero order, AR coated at 780 nm)

<sup>11</sup>For diode laser: Thorlabs IO-3D-780-VLP (isolation 34 – 40 dB, operating range 760 – 800 nm), for Ti:Sa laser Newport ISO-04-780-LP (isolation 30 – 38 dB, center wavelength 780 nm, tunable 720 – 840 nm)

<sup>12</sup>Thorlabs GTH5M-B (AR coated 650 – 1050 nm)

<sup>13</sup>The diode laser already has a 60 dB optical isolator installed, but the MSquared Ti:Sa does not contain an isolator to avoid light being reflected back into the laser.

<sup>14</sup>Thorlabs EO-PM-NR-C1

<sup>15</sup>QiOptiq PM-C-BB

<sup>16</sup>Thorlabs LA1172-B, focal length  $f = 400$  mm, AR coated 650 – 1050 nm

<sup>17</sup>Usually a laser is locked to a  $\text{TEM}_{00}$  mode of the cavity. The PDH error signal slope is proportional to the power in the mode and the  $\text{TEM}_{00}$  mode typically appears higher than other modes in the spectrum. This is due to local defects in the coating, where the  $\text{TEM}_{00}$  with the smallest spot size on the mirrors displays the lowest losses.

<sup>18</sup>Thorlabs PDA10A-EC (200 – 1100nm, 150 MHz bandwidth)

<sup>19</sup>Ti:Sa laser path: Thorlabs PDA10A-EC (200 – 1100nm, 150 MHz bandwidth), diode laser path: PDA36A-EC (350 – 1100nm, 10 MHz bandwidth, switchable gain)

<sup>20</sup>Conrad CMOS 700TVL

<sup>21</sup>SRS DS345

<sup>22</sup>QiOptiq SIN-Amplifier

## 5. Experimental Setup of the Transfer Lock

MHz. The amplifiers used here don't provide the possibility to adjust the phase of the signal, which is necessary to optimize the PDH error signal. However, since the frequency can be changed, it is always possible to find a frequency for which the phase is roughly optimized. The signal from the function generator is additionally sent to a mixer<sup>23</sup> to generate the PDH error signal. The other input of the mixer is connected to the fast photodiode which detects the light reflected at the cavity. This photodiode signal is first low pass filtered<sup>24</sup> to reduce noise at high frequencies and passes a transformer<sup>25</sup> to avoid ground loops. In the case of the MSquared Ti:Sa laser, the photodiode signal is also amplified with an amplifier<sup>26</sup> which in turn amplifies the PDH error signal at the output of the mixer improving the S/N ratio<sup>27</sup>. For both laser locks, the output of the mixer has to be low-pass filtered to recover the form of the PDH error signal as shown in figure 3.8b. The error signals of the diode laser at 785 nm and MSquared Ti:Sa laser at 785 nm and 729 nm are shown in appendix A. These error signals are fed into the input of the respective PID-controllers.

A Toptica Digilock110 module is used for PID-control of the diode laser. The Digilock contains three controllers: A fast digital PID-controller and an analog P-controller, for fast feedback to the injection current, and another digital PID-controller to compensate slow drifts, where feedback is applied to the diffraction grating of the ECDL. The fast feedback branch has a bandwidth of 10 MHz.

A Toptica FALC110, which is a very fast (45 MHz bandwidth) analog controller, is used for PID-control to lock the MSquared Ti:Sa laser. The FALC110 also has two outputs. Both controller output signals are sent to mirror M3 inside the laser cavity, via the ICE-Bloc, which is mounted on the dual-stack piezo. When locking the lasers to the reference-cavity, the PID-parameters are optimized such that fluctuations in the error signal are minimized and the transmission of light at the cavity is maximized.

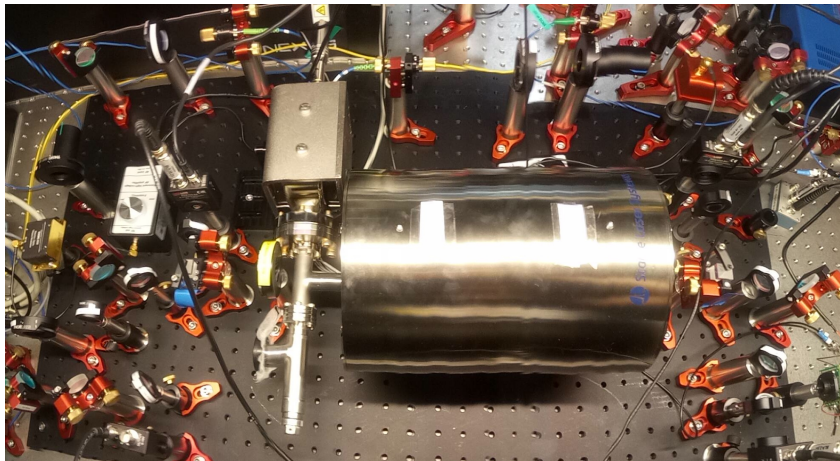


**Figure 5.12.:** Photograph of the optical setup: The centerpiece is the reference-cavity vacuum chamber with the attached ion pump. The optics for PDH locking of two lasers to the cavity from two sides are shown.

<sup>23</sup>MiniCircuits ZAD-1-1+

<sup>24</sup>MiniCircuits filters

<sup>25</sup>MiniCircuits FTB-1-1 (diode laser) and FTB-1-6 (MSquared laser)

<sup>26</sup>MiniCircuits ZFL-1000

<sup>27</sup>This can be done internally in the locking module used for the diode laser.

## 6. Characterization of the Frequency-Stability of the Locked Lasers

As discussed in section 3.3.2, performing a frequency beat measurement allows the linewidth of a laser and drift with respect to a second laser to be measured. This technique is now used to characterize the diode laser and MSquared Ti:Sa laser, locked to our reference-cavity. To be able to observe a beat note, the following conditions have to be met: The spatial distributions and polarizations of the two light fields involved in the beat measurement must not be orthogonal and the beat frequency must lie within the bandwidth of the photo detector, which is typically between a few MHz up to tens of GHz. Since there is no other narrow 785 nm lasers in our lab (lab 1 at IQOQI) available, such that the frequency difference between the lasers is sufficiently small, one idea is to lock the diode laser and MSquared Ti:Sa laser to two adjacent modes of our reference-cavity at 785 nm and beat them with each other<sup>1</sup>. However, the linewidth of the beat can be less than the sum or quadratic sum of the individual laser linewidths, if the phase noise of the two lasers is partially correlated. Since the two lasers are locked to the same cavity, any contribution of the cavity to the laser linewidth drops out in a beat between them. Therefore, such a measurement is not conclusive as it may not represent the actual linewidths of the lasers.

A solution is to use the frequency comb in the adjacent lab 2. This frequency comb (Menlo Systems FC1500) is based on a mode-locked Erbium-doped fiber ring laser. The repetition rate and carrier envelope offset can either be locked to a GPS-based 10 MHz frequency reference based on a quartz oscillator, which results in comb teeth in the MHz range (FWHM), or optically locked to the narrow (1 Hz) QSim 729 nm laser in lab 1, itself locked to a ULE reference-cavity, with a drift rate of 63 mHz/s [69] [70]. By measuring a beat signal between the QSim laser and the frequency comb with a fast photodiode, and then using this signal as a reference to feedback to an EOM inside the cavity of the mode-locked laser, the comb teeth can be narrowed to a few Hz FWHM.

Using this frequency comb, it was possible to measure the linewidths of the diode laser and MSquared Ti:Sa laser at 785 nm, as well as the drift rates, which is presented in this chapter. The goal is to verify linewidths of both lasers of less than 10 kHz at 785 nm and drift rates of less than 1 Hz/s. Moreover, the MSquared Ti:Sa laser was locked to the reference-cavity at 729 nm and the laser linewidth was measured in a beat measurement

---

<sup>1</sup>Eventually, the Raman laser (Ti:Sa) will operate at 786 nm, as this corresponds to the fundamental of the 393 nm light, required for the Raman process. However, since the linewidth of the reference-cavity at 785 nm and 786 nm is very similar, i.e. approximately 66(2) kHz and 70(1) kHz, respectively, the laser linewidth result at 785 nm should be representative of the result which can be achieved at 786 nm.

with the QSim 729 nm laser, which is also presented in the following.

## 6.1. Linewidths of the Lasers

### 6.1.1. MSquared Ti:Sa Laser and Diode Laser at 785 nm

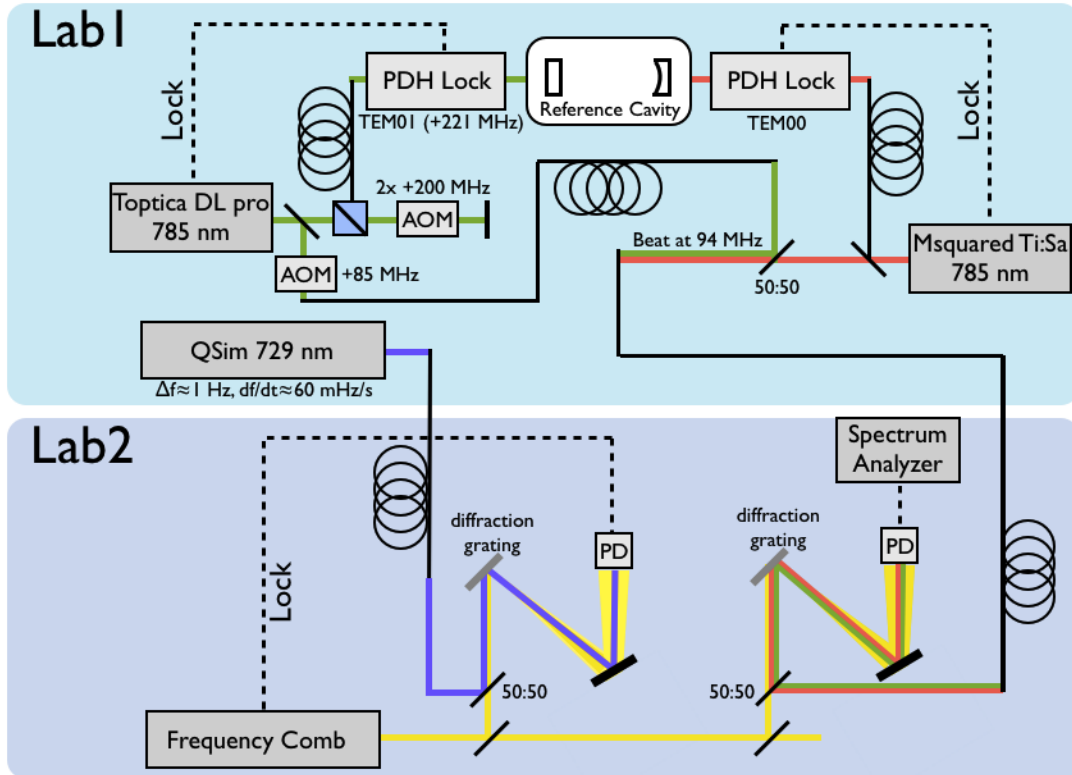


**Figure 6.1.:** Setup for the linewidth measurements: The diode laser and MSquared Ti:Sa laser are tuned to 785 nm and locked to two adjacent modes (TEM<sub>10</sub> and TEM<sub>00</sub>, respectively) of the reference-cavity. By shifting the light from the diode laser with AOMs, a beat frequency at 94 MHz between the diode laser and MSquared Ti:Sa laser is obtained. Both lasers are sent through a 20 m long fiber to the adjacent lab 2. Light from the QSim 729 nm laser is also sent to lab 2 through a different fiber (20 m, fiber-noise cancelled). The frequency comb is optically locked to the QSim 729 nm laser to narrow the comb teeth to Hz level. Here, the frequency beat between the QSim laser and comb is detected with a fast photodiode (PD) and used as feedback to be kept constant. The light from the diode laser and MSquared Ti:Sa laser is superimposed with the light from the frequency comb on a second photodiode. Before measuring the beat signals with the photodiodes, the light is diffracted at a diffraction grating, such that the photodiodes don't get oversaturated. The photodiode detecting the beats between the comb, diode laser and MSquared Ti:Sa laser is connected to a spectrum analyzer to investigate the linewidths of the beats signals.

The linewidths of the MSquared Ti:Sa laser and diode laser at 785 nm were determined via a frequency beat measurement with the frequency comb. The setup for the linewidth measurements is shown in figure 6.1.

## 6. Characterization of the Frequency-Stability of the Locked Lasers

In lab 1, the diode laser and MSquared Ti:Sa laser are locked to a TEM<sub>01</sub> and TEM<sub>00</sub> mode of our reference-cavity, respectively. The frequency of the TEM<sub>01</sub> mode is 221 MHz higher than the frequency of the TEM<sub>00</sub> mode. By using a double-pass AOM at  $2 \times 200 \text{ MHz}^2$  in the diode laser path to the reference-cavity and another single pass AOM at  $85 \text{ MHz}^3$  in the path to where the diode laser and MSquared Ti:Sa laser are overlapped on a 50:50 beam splitter, the beat frequency can be shifted to 94 MHz. Both lasers are coupled into one 20 m long fiber which goes to lab 2. Additionally, the light from the QSim 729 nm laser is sent through a different fiber to lab 2 (20 m, fiber-noise cancelled). In lab 2, the light from the diode laser and MSquared Ti:Sa laser is overlapped with light from the frequency comb on a fast photodiode<sup>4</sup>. This photodiode is connected to a spectrum analyzer<sup>5</sup> to measure the frequency beats between the MSquared Ti:Sa laser, diode laser and frequency comb.

To narrow the comb teeth to approximately 1 Hz on a timescale of a few seconds, the repetition rate and carrier envelope offset frequency of the frequency comb have to be optically locked. This is achieved by superimposing comb light with light from the narrow QSim 729 nm laser on a second photodiode, where the beat signal between the QSim laser and comb is used as a reference for the optical lock. As a result, the comb teeth are much more narrow than the linewidths of the MSquared Ti:Sa laser and diode laser are expected to be.

The measured linewidth results are now presented. In order to be able to compare the different beat linewidths, the same sweep time of 1.2 s and resolution bandwidth of 100 Hz was used for all of the measurements. The average of 10 consecutive sweeps was used, such that the linewidths shown correspond to linewidths of the lasers over a timescale of 12 s.

**Table 6.1.:** Linewidths of the beat signals involving the respective laser pairs.

Beat	FWHM Linewidth
diode laser and MSquared Ti:Sa laser	101(2) Hz
MSquared Ti:Sa laser and frequency comb	87(1) Hz
diode laser and frequency comb	180(3) Hz

Figure 6.2 shows the beat between the MSquared Ti:Sa laser and diode laser. The FWHM linewidth of the Lorentzian fit is 101(2) Hz. One can see 1.9 kHz sidebands resulting from a mechanical resonance of the MSquared Ti:Sa laser, which are approximately 15 dB below the carrier<sup>6</sup>. Figure 6.3 shows the beat between the MSquared Ti:Sa laser and frequency comb. The linewidth of the Lorentzian fit is 87(1) Hz. Again, one can see the 1.9 kHz resonances, which are approximately 15 dB suppressed. Turning up the gain of the fast

<sup>2</sup>Gooch & Housego 3200-124

<sup>3</sup>Gooch & Housego 3080-125

<sup>4</sup>MenloSystems APD110, wavelength range 400 – 1000 nm, frequency range 1 – 800 MHz

<sup>5</sup>Rohde & Schwartz FSP (Resolution bandwidth 1 Hz to 10 MHz, frequency range 9 kHz to 3 GHz)

<sup>6</sup>Zooming out further, see appendix B, one can also see the MSquared Ti:Sa laser’s etalon dither frequency at 19 kHz, more than 20 dB below the carrier and servo bumps of the diode laser at approximately 400 kHz.

## 6. Characterization of the Frequency-Stability of the Locked Lasers

feedback branch of the MSquared Ti:Sa laser too high showed a resonance at 67 kHz, likely a resonance of the fast piezo. Figure 6.4 shows the beat between the diode laser and comb. The linewidth of the Lorentzian fit is 180(3) Hz. The S/N ratio for this beat is the worst out of all of them due to the limited light power available. Table 6.1 shows an overview of the measured beat linewidths over a timescale of 12 s. The fact that the line shapes are Lorentzian rather than Gaussian indicates that white frequency noise plays a dominant role and low frequency noise sources, moving the Lorentzian around a center frequency, which creates a Gaussian lineshape, contribute less.

Under the reasonable assumption, that the MSquared Ti:Sa laser and diode laser linewidths are much broader than the linewidth of the comb teeth, it can be estimated that the beat linewidth between the diode laser and comb (MSquared Ti:Sa laser and comb) is approximately equal to the linewidth of the diode laser (MSquared Ti:Sa laser). The fact that the individual laser linewidths of the diode laser and MSquared laser don't add up to the beat linewidth between the two lasers indicates, that the noise of the two lasers is partially correlated. Such a correlation can result from instabilities of the reference-cavity length, which affect both the diode laser and MSquared laser, locked to the reference-cavity, equally. Another source for correlated laser noise is fiber noise. Since the diode laser and MSquared Ti:Sa laser are sent through the same fiber, fiber noise will affect the two lasers equally.

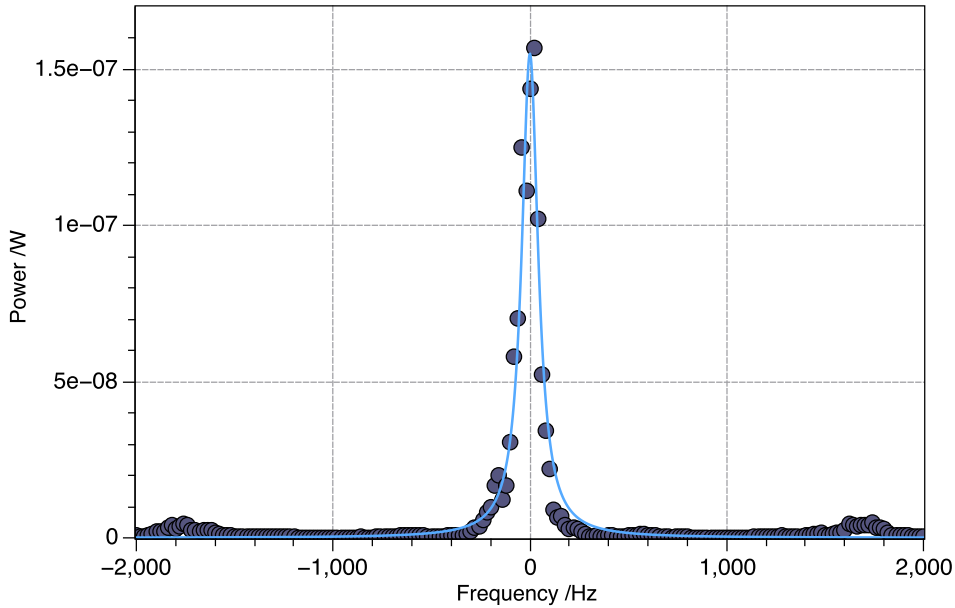


**Figure 6.2.:** Beat between MSquared Ti:Sa laser and diode laser measured over a timescale of 12 s (average of 10 consecutive measurements) and a resolution bandwidth of 100 Hz with a Lorentzian fit (blue, FWHM linewidth of 101(2) Hz): The MSquared Ti:Sa laser was locked to our reference-cavity ( $TEM_{00}$ ) using a FALC110 PID-controller. The diode laser was locked to the same reference-cavity to the adjacent  $TEM_{01}$  mode, using a Digilock110. Small sidebands at 1.9 kHz are visible due to a mechanical resonance of the MSquared Ti:Sa laser.

## 6. Characterization of the Frequency-Stability of the Locked Lasers

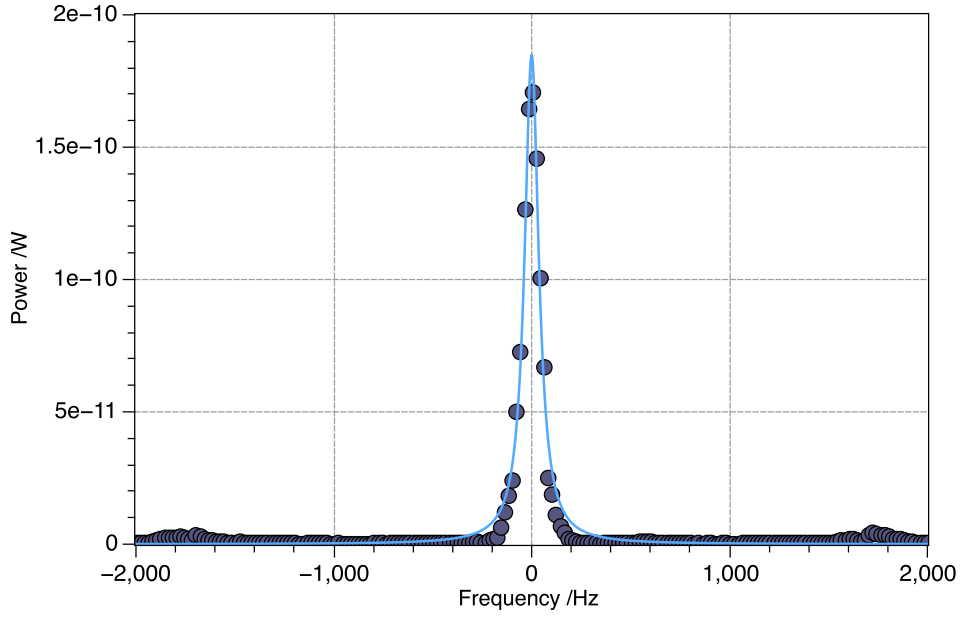


**Figure 6.3.:** Beat between MSquared Ti:Sa laser and frequency comb measured over a timescale of 12 s (average of 10 consecutive measurements) and a resolution bandwidth of 100 Hz with a Lorentzian fit (blue, FWHM linewidth of 87(1) Hz): The frequency comb was optically locked to the narrow QSim 729 nm laser, resulting in a comb teeth linewidth of a few Hz.

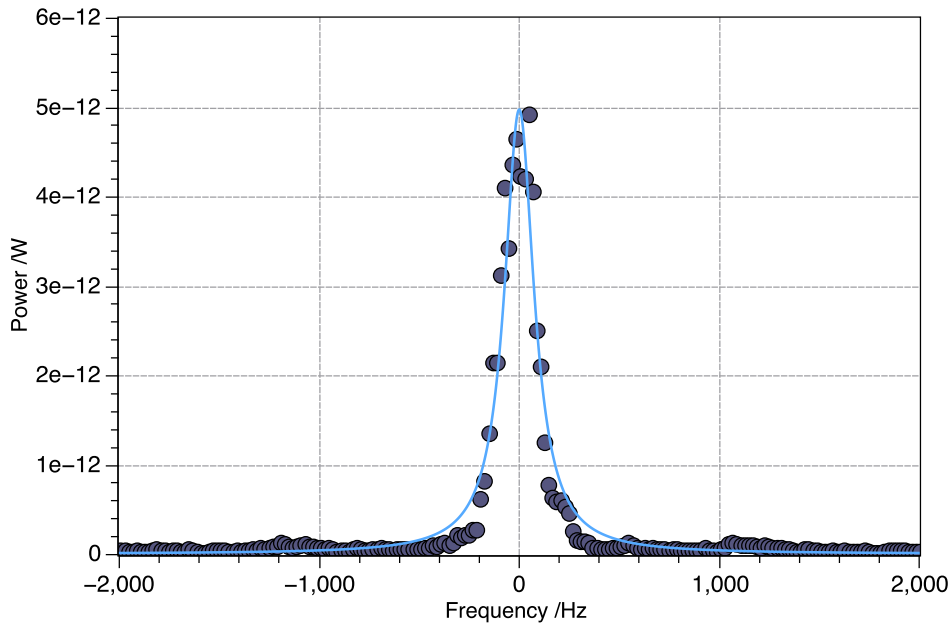


**Figure 6.4.:** Beat between frequency comb and diode laser measured over a timescale of 12 s (average of 10 consecutive measurements) and a resolution bandwidth of 100 Hz with a Lorentzian fit (blue, FWHM linewidth of 180(3) Hz): Here, the S/N ratio was worse compared to the previous measurements due to the limited light power available. There are small sidebands visible at 1.1 kHz, whose origin could not be determined.

## 6. Characterization of the Frequency-Stability of the Locked Lasers

In conclusion, the goal was to narrow the diode laser and MSquared Ti:Sa laser to linewidths of a few kHz or less. This goal was achieved for both laser systems. In the experiment, the narrow diode laser will act as a stable reference to lock the length of the cavity around the ion to a small fraction of its linewidth set by the mirror properties. The Raman laser linewidth is also locked to within the linewidth of the Raman transition which ensures a coherent transfer of population during a cavity-mediate Raman process.

### 6.1.2. MSquared Ti:Sa Laser at 729 nm

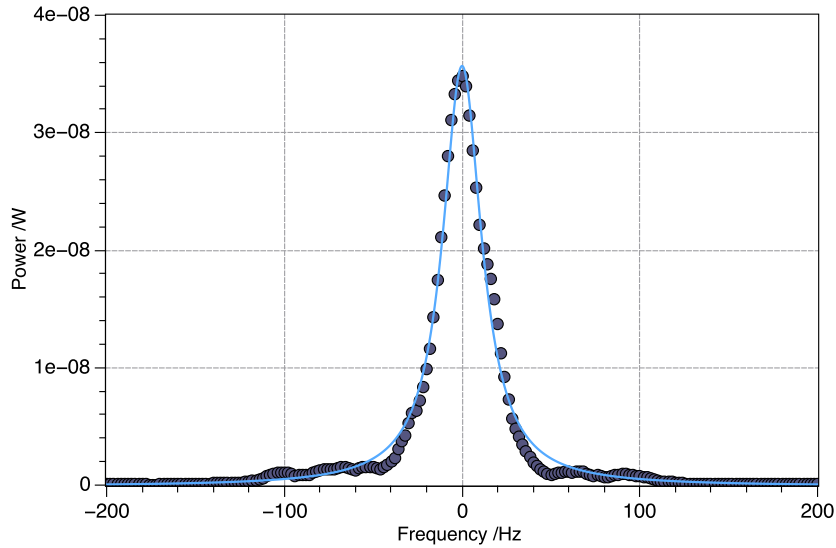


**Figure 6.5.:** Beat signal between our MSquared Ti:Sa laser locked at 729 nm and QSim laser measured over a timescale of 11.5 s (average of 10 consecutive measurements), with a resolution bandwidth of 30 Hz with a Lorentzian fit (blue, FWHM linewidth of 26.7(2) Hz): Our MSquared Ti:Sa was locked to a TEM<sub>00</sub> mode of our reference-cavity using a FALC110 PID-controller. The noise around the carrier is likely fiber noise.

To characterize how well the MSquared Ti:Sa laser can be locked to the reference-cavity at 729 nm, a frequency beat measurement with the QSim 729 nm laser was performed. These measurements were performed in lab 1, where the light from the QSim 729 nm laser was sent through a 10 m long fiber<sup>7</sup>. The result is shown in figure 6.5. The FWHM linewidth of the Lorentzian fit is 26.7(2) Hz over a timescale of 11.5 s. When turning up the gain of the fast feedback branch too high, a 105 kHz resonances can be observed in the lock, which corresponds to a resonance of the fast piezo of the Ti:Sa. This resonance can only be observed in the 729 nm lock, not in the 785 nm lock. The difference between the locks is that for the 729 nm lock, where very fast feedback is required due to the narrow cavity linewidth and correspondingly steep PDH error signal slope, a D-controller had to be used, which was not necessary for the 785 nm lock. A D-controller extends the feedback bandwidth of the laser lock, such that here this resonance frequency of the piezo could be reached. Here, the limitation in terms of linewidth of our MSquared

<sup>7</sup>No fiber-noise cancellation was implemented here which can mean that the linewidth of the QSim laser is broadened due to fiber noise

## 6. Characterization of the Frequency-Stability of the Locked Lasers

Ti:Sa laser is probably the bandwidth of the feedback elements of the laser. With faster feedback elements, e.g. using an AOM or EOM, it should be possible to narrow the laser linewidth to  $\sim 1$  Hz FWHM on a timescale of seconds, which was achieved in another team in our group with the same type of laser [64]. Furthermore, shielding the cavity better from acoustic noise and vibrations by putting it in an acoustically isolated box sitting on sorbothane pads can also improve the locked laser stability.

### 6.2. Drifts of the Lasers

Now the drifts of the diode laser and MSquared Ti:Sa laser, which are locked to the reference-cavity at 785 nm, are determined. As discussed earlier, when performing a frequency beat measurement involving two lasers, only the relative drift between them can be measured by tracking the beat frequency over time. If the amount and direction of the drift of one of the lasers is known, then the absolute drift of the second laser can be determined. In the previous section, the frequency comb was locked to the QSim 729 nm laser, to narrow the comb teeth to Hz level. In that setup, the frequency comb drifts along with the QSim laser<sup>8</sup>. Since the frequency drift of the QSim 729 nm laser can be monitored via Ramsey experiments with a trapped  $^{40}\text{Ca}^+$  ion, the frequency comb would serve as an appropriate reference, with a well-known drift rate, for a drift measurement with the diode laser or MSquared Ti:Sa laser. However, the optical frequency comb lock is not suitable for measurements on a long timescale, as it is very sensitive to acoustic noise in the lab. Since narrow comb teeth, the main reason for using the optical lock, are not required for the drift measurement, the repetition rate and carrier envelope offset of the frequency comb are now locked to the 10 MHz GPS frequency reference, which results in a stable lock on a timescale of hours. To still be able to keep track of the drift of the comb, a beat measurement between the QSim 729 nm laser and comb is performed, where the drift of the QSim 729 nm laser is monitored via Ramsey experiments with a trapped  $^{40}\text{Ca}^+$  ion. As a result, the drift of the comb can be monitored via an ion as a frequency reference, without having the comb optically locked and thus avoiding instability-related problems during the long drift measurements.

The drifts of the diode laser and MSquared Ti:Sa laser were determined by tracking the beat between the MSquared Ti:Sa laser and diode laser and the beat between the MSquared Ti:Sa laser and the frequency comb, which has a well-known drift.

The setup for the drift measurement is similar to the previous setup from figure 6.1. As already stated, one difference is that the frequency comb is locked to the 10 MHz GPS signal. Furthermore, in contrast to before, where the photodiode detecting the beat between the diode laser, MSquared Ti:Sa laser and frequency comb, was connected to the spectrum analyzer, now the photodiode signal is split and sent to inputs of the frequency counter<sup>9</sup>, which is part of the comb electronics. Appropriate bandpass filters are chosen such that the S/N ratio is improved sufficiently for the counter to detect the

---

<sup>8</sup>In principle, the drift of the 729 nm laser, which results from aging-related drifts of the QSim reference-cavity (63 mHz/s), can be compensated with AOMs. But this was not done for any of the measurements performed in the course of this thesis.

<sup>9</sup>The counter works up to 60 MHz so the beat between MSquared Ti:Sa laser and diode laser at 94 MHz was mixed down to 39 MHz with a Rhode & Schwarz SMC100A.

## 6. Characterization of the Frequency-Stability of the Locked Lasers

beat frequency accurately. To ensure that the frequency counter works properly, the photodiode signals are further split and sent to two inputs of the counter, where one input is attenuated by 10 dB. If the two frequency curves match, the S/N ratio is good enough. The frequency counter is referenced to the same 10 MHz GPS reference as the comb and records a frequency value every second.

The QSim 729 nm laser is additionally used in Ramsey experiments to determine its absolute drift with a  $^{40}\text{Ca}^+$  ion in a linear Paul trap in lab 2 as a reference. Ramsey experiments in two different atomic transitions allow the laser-atom frequency difference to be distinguished from changes in the local magnetic field [69]. The three beats, which are tracked to determine the drift of the lasers, are at 19 MHz (QSim and comb), 30 MHz (comb and MSquared) and 39 MHz (MSquared and diode laser). The positions of the three lasers with respect to the frequency comb are shown in figure 6.6. The repetition rate of the comb and therefore the spacing of the comb teeth is 250 MHz.

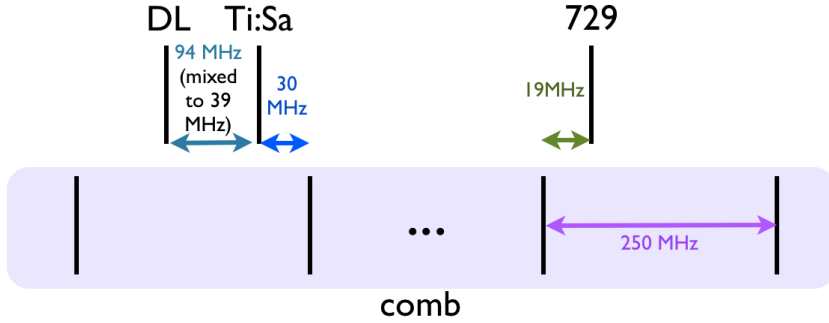


**Figure 6.6.:** Positions of the three lasers with respect to the comb during the drift measurements: Here, DL is the diode laser, Ti:Sa the MSquared laser, and 729 the QSim laser.

The three beat signals tracked over the course of a few hours with the frequency counter and the drift of the QSim 729 nm laser measured via Ramsey experiments are provided in appendix C.

The absolute drifts of the MSquared Ti:Sa laser and diode laser, which are locked to the reference-cavity, are obtained by subtracting the different beat and Ramsey curves: The drift of the comb is determined by subtracting the beat between comb and Qsim laser from the drift of the Qsim laser (measured with Ramsey experiments). Then the drift of the MSquared Ti:Sa laser is calculated by subtracting the beat between MSquared laser and comb from the drift of the comb. Finally, the drift of the diode laser is found by subtracting the beat between MSquared laser and diode laser from the drift of the MSquared laser.

The absolute drifts of the MSquared Ti:Sa laser and diode laser are shown in figure 6.7. The drift of the MSquared laser is approximately linear, which means that this drift likely corresponds to the aging-related drift of the reference-cavity. A linear fit  $0.202(1)t - 49(4)$  can be applied to the MSquared Ti:Sa laser data, which shows that the reference-cavity drifts at a rate of 202(1) mHz/s which is less than the goal of 1 Hz/s.

The diode laser shows additional drifts on the timescale of the lab air conditioning cycle. After examining the optical setup of the laser locks with a heat gun, it turned out that these drifts are caused by the Thorlabs EOM that was used to modulate sidebands for locking onto the diode laser. This EOM, in contrast to the QiOptiq EOM, used in the

## 6. Characterization of the Frequency-Stability of the Locked Lasers

MSquared Ti:Sa laser locking path, has only one crystal inside. It is thus much more sensitive to temperature changes in the lab which leads to a change in RAM and therefore the DC offset of the PDH error signal. The frequency of the diode laser then follows this change in the DC offset. The Thorlabs EOM has since been replaced with another QiOptiq EOM. Once the temperature related drifts are removed from the green trace in figure 6.7, the same linear drift rate as for the red line should be achieved. This is further evidence that this linear drift is due to the aging-related drift of the common cavity. Such a cavity drift usually decreases with time [58]. Since the reference-cavity was less than a year old when these measurements were taken, it is expected that the drift rate will decrease in the future.

In the context of quantum network experiments with a remote cavity-enhanced trapped-ion node, a drift rate of the laser systems of approximately 200 mHz/s (720 Hz/hr) represents a satisfactory result. When the ion-cavity locking laser and Raman laser fundamental drift at this rate, the locked ion-cavity drifts at 720 Hz/hr and the 393 nm Raman laser drifts at 1440 Hz/hr, a factor of two faster due to frequency doubling. This means that after approximately 140 hours, which is much longer than our experiments will be, the frequency difference between the Raman laser and cavity resonance frequency will be as much as the expected ion-cavity linewidth (100 kHz). After 70 hours, the linewidths of the Raman laser and cavity will start to become resolved such that the Raman condition is not maintained any longer. After 140 hours, the frequency of the photons generated in the cavity-mediated Raman process will have drifted by one ion-cavity linewidth and may not match the remote cavity frequency anymore.

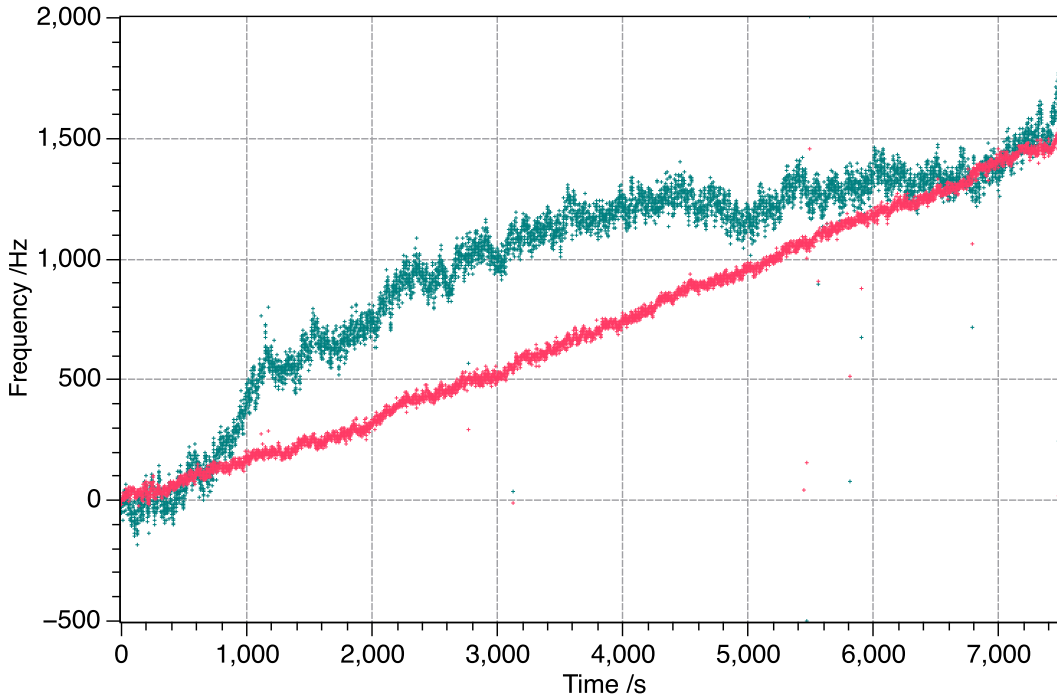


**Figure 6.7.:** Absolute frequency drifts of the MSquared Ti:Sa laser (red) and diode (green): The data points that don't follow the curve are cycle slips of the frequency counter, which occur when someone knocks the optical table the laser is located. The frequency of the diode laser shows an increased instability compared to the MSquared due to a higher temperature sensitivity of the EOM used in the diode laser locking path.

## 7. Application of the Stabilized Laser Systems

The main goal for the stabilized laser systems, i.e. the MSquared Ti:Sa laser at 786 nm and the diode laser at 785 nm, is that they will be used in a transfer lock to implement a cavity-mediated Raman process. Unfortunately, since our experiment is still under construction, it was not possible to test the transfer lock with a cavity-enhanced trapped-ion system. At the end of this master's thesis, the ion-cavity has yet to be put inside our vacuum chamber where the ion trap has already been successfully installed. However, a test ion-cavity, similar to the one that will eventually be put in vacuum, was built and setup in air. Locking such a test ion-cavity allows the process of locking a cavity to a stable laser to be practiced. Important characteristics of the ion-cavity structure can be learned from this, e.g. resonances which are driven via the feedback loop during locking. Such resonances and their effect on the lock can then be investigated which allows us to think about solutions to these problems prior to putting an ion-cavity in vacuum.

A second goal, which was not the main focus of this work, was to lock the MSquared Ti:Sa laser to the reference-cavity at 729 nm, the transition wavelength of the optical qubit in  $^{40}\text{Ca}^+$ . Since we had an ion trap available at the end of this master's thesis, it was possible to use the laser locked at 729 nm to manipulate a trapped  $^{40}\text{Ca}^+$  ion and observe Rabi flops.

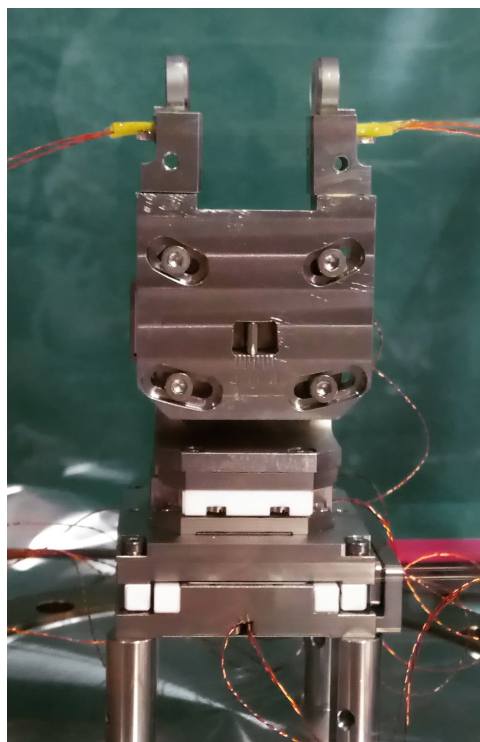


**Figure 7.1.:** Test ion-cavity: The test-cavity is setup in air. The mirror spacing and height can be controlled via piezos.

### 7.1. Test Ion-Cavity Lock at 785 nm

#### 7.1.1. Test Ion-Cavity Properties

The test ion-cavity, which is shown in figure 7.1, was assembled by Josef Schupp. The cavity is glued onto a U-structure, where each cavity mirror is glued on top of shear piezos, which allow motion of the mirrors along the cavity axis. The cavity-U structure is mounted on x,y,z translation stages for nano positioning of the cavity mode, eventually

## 7. Application of the Stabilized Laser Systems

with respect to trapped ions at the cavity focus. The test ion-cavity has a mirror spacing of  $L = 2$  cm, such that our ion trap fits between the mirrors, and is in the near concentric regime [12]. The test-cavity mirrors were coated by ATF.

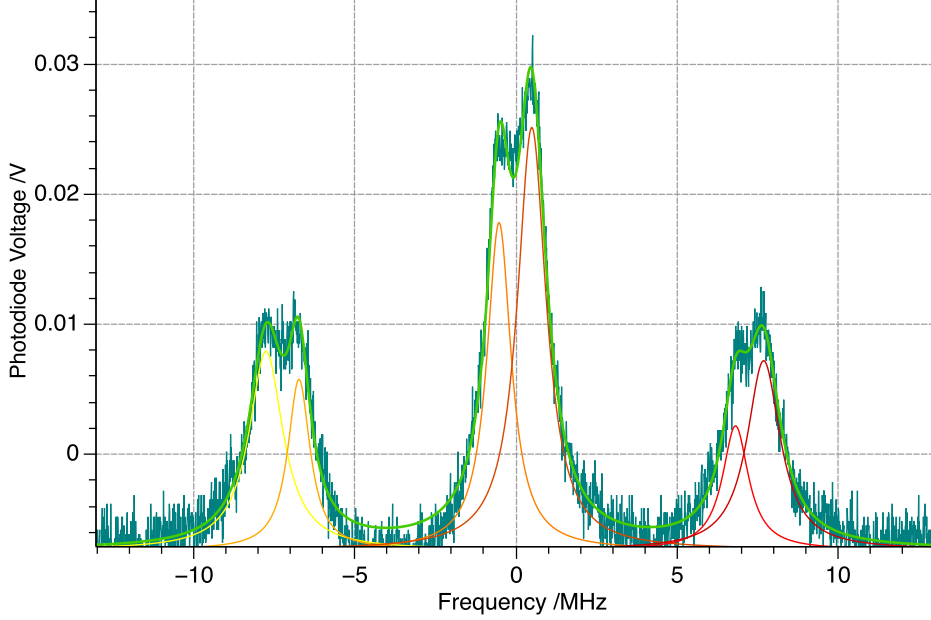


**Figure 7.2.:** Transmitted intensity at the test-cavity: The test-cavity length was scanned by applying a triangle voltage to one of the mirror piezos. When scanning over the resonance of a  $\text{TEM}_{00}$  mode and the sidebands in 50 ms, the displayed signal (dark green) was observed on an oscilloscope. The time axis of the oscilloscope was converted to the frequency axis shown here by relating the sideband time-distance to the known EOM modulation frequency 7.4 MHz. Six individual Lorentzian curves (yellow, orange and red lines) were fitted to the birefringent signal. The individual fits add up to give the light-green six-peak Lorentzian fit.

First, the test ion-cavity mirror properties were characterized at 785 nm. Light from the MSquared Ti:Sa laser locked to the reference-cavity at 785 nm was phase-modulated with an EOM to put sidebands on it. This light was then sent into the test ion-cavity. The test ion-cavity length was scanned by applying a triangle voltage to one of the piezos under a cavity mirror. A DC voltage from an HV converter was applied to the other mirror, to find the resonance of a  $\text{TEM}_{00}$  mode of the test-cavity. The cavity resonance as well as the sidebands resulting from the phase modulation process were observed when detecting the light transmitted at the test-cavity with a photodiode. This is shown in figure 7.2. One can see six peaks instead of the expected three, one carrier and two sidebands, due to the cavity being birefringent. The birefringence of the mirrors results from gluing related stress on the mirrors. Six Lorentzian fits were matched to the data points in figure 7.2 to determine the position and linewidths of the peaks. The time axis of the oscilloscope was converted to frequency units, by relating the average distance between the carriers and corresponding sidebands to the known EOM modulation frequency of 7.4 MHz. Then, the linewidth of the cavity was calculated in units of frequency. The average cavity linewidth of one polarization mode is 1.08(8) MHz at 785 nm. We were hoping to achieve a result in the range of 100 kHz at this wavelength. The finesse is therefore much lower than requested by us.

## 7. Application of the Stabilized Laser Systems

These test-cavity mirrors are not suitable to be used for the final cavity, which will go inside the vacuum chamber with the ion trap, to implement the cavity-mediated Raman process, for the following reasons. First, birefringent mirrors result in undesirable effects when encoding a flying qubit in two orthogonal polarization states of a photon, as presented in section 2.5. For example, in this case entanglement with the frequency degree of freedom is not avoided. Due to the energy splitting between the polarization states in superposition, e.g. when preparing a photon state  $1/\sqrt{2}(|H\rangle + |V\rangle)$ , the phase of the superposition state rotates in time, where after a certain time a state orthogonal to the initial state is created. This results in the fidelity being a sinusoidal function of time. In principle, this effect can be calibrated, but this becomes difficult if the birefringence is very large. Therefore, it is generally better to have near-degenerate polarization modes, which then presents no restriction. For the final ion-cavity mirrors, great care during the gluing process needs to be taken such that birefringence is minimized as much as possible. Second, the test-cavity linewidth at 785 nm, which depends on the properties of the mirror coatings, is 1.08(8) MHz, much broader than desired. This limits how well the test-cavity can be locked to the reference laser. In principle, it would be possible to tune the laser to a different wavelength where the finesse of the test-cavity is higher. However, the mirror losses at 854 nm (measured by Josef Schupp) are also significantly higher than requested. As a result, no mirrors from this coating run can be used for the final ion-cavity.

### 7.1.2. Test Ion-Cavity Lock Characterization

The test ion-cavity was locked in air using the setup shown in figure 7.3. First, the MSquared Ti:Sa laser<sup>1</sup> was locked at 785 nm to a TEM<sub>00</sub> mode of the reference-cavity. The light of the locked laser was then used as a stable reference to lock the test ion-cavity via a PDH locking scheme to a TEM<sub>00</sub> mode<sup>2</sup>. Since the FSR of the test ion-cavity is large at 7.5 GHz, double resonance of the reference-cavity and test ion-cavity could only be achieved for certain longitudinal modes of the reference-cavity.

The PDH error signal of the test ion-cavity is shown in figure 7.4. Due to the birefringence of the cavity, the error signal shows a curve in the middle of the slope. Therefore the cavity should not be locked to the center of the error signal but an offset should be added, such that the cavity can be locked to one polarisation mode, i.e. a part of the error signal that is linear. The sideband frequency was again used to convert time to frequency units.

---

<sup>1</sup>Eventually the diode laser will be used to lock the ion-cavity. However, for this test we used the MSquared laser as we expected the locking of the test ion-cavity in air to be challenging and wanted to have the option of tuning the locking laser to various different wavelengths where the finesse of the test ion-cavity is different, in the case that we didn't succeed at 785 nm.

<sup>2</sup>For the cavity-mediated Raman process with a trapped ion, the e.g. TEM<sub>01</sub> mode should be chosen as it has an intensity minimum along the ion string, which reduces AC Stark shifts.

## 7. Application of the Stabilized Laser Systems

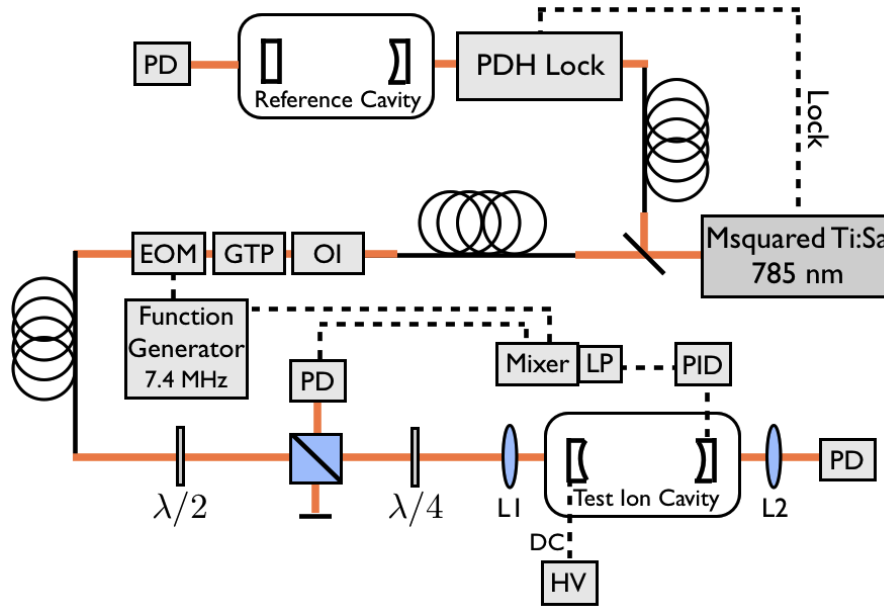


**Figure 7.3.:** Setup of the test ion-cavity lock: The MSquared Ti:Sa laser is locked to our reference-cavity at 785 nm via a PDH locking scheme. This light is then used as a stable reference to lock the length of the test ion-cavity in air using again a PDH scheme. Feedback for the test ion-cavity lock goes to one of the mirror piezos. A high DC voltage is applied to the other piezo to find the resonance of a  $TEM_{00}$  mode of the test ion-cavity. The focal length of lenses L1 and L2 is  $f = 50$  mm.

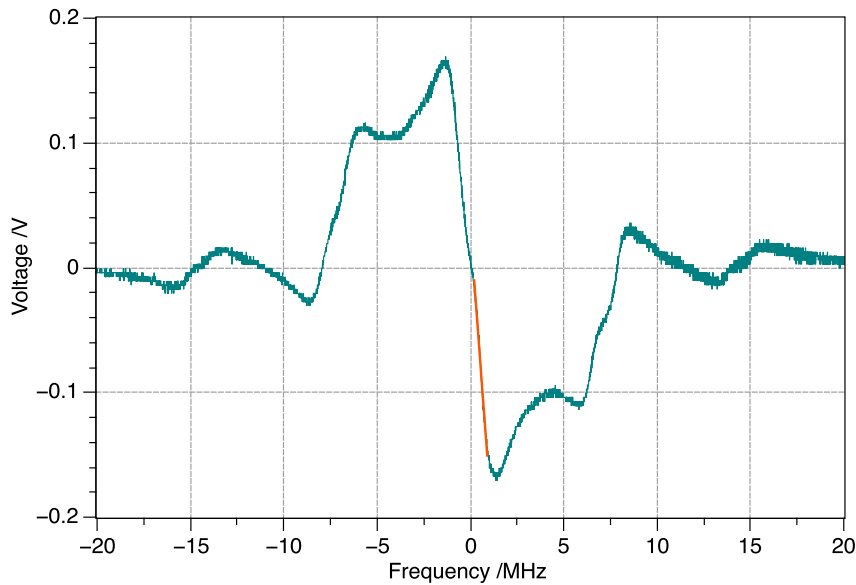


**Figure 7.4.:** Test ion-cavity error signal: The PDH error signal (green) was measured by having the MSquared Ti:Sa laser locked to a  $TEM_{00}$  mode of the reference-cavity at 785 nm and then scanning the length of the test ion-cavity over the resonance of a  $TEM_{00}$  mode via applying a triangle voltage to one of the piezos. The time axis of the oscilloscope, was converted to the frequency axis shown here by relating the sideband time-distance to the known EOM modulation frequency 7.4 MHz. The orange line represents a linear fit to the error signal slope, which is used to determine the error signal's PSD in frequency units.

### Resonances of the Test Ion-Cavity Structure

To lock the test-cavity to the laser, feedback was applied to one mirror piezo using an SRS sim960 PID-controller, while a DC voltage was applied to the other piezo to find the resonance of a TEM<sub>00</sub> mode. Here, only the I-controller could be used as the lock became unstable immediately when switching on the P-gain due to the the P-controller driving resonances of the cavity-U structure. To investigate these resonances, white noise was applied to the second piezo on top of the DC voltage, while having the cavity locked with the I-controller. The locked error signal of the test ion-cavity with white noise applied is shown in figure 7.5. There are resonances visible in the spectrum, which are on the order of the resonances predicted by finite element simulations of the ion-cavity structure carried out by Josef Schupp in Comsol. The most prominent ones are at multiples of approximately 7 kHz and 8 kHz. Even though these could not be identified as specific modes in Josef Schupp's simulations, we believe that they correspond to shear modes of the U-structure, where the test-cavity mirrors oscillate out of phase which changes the test-cavity length. Modes, where the test-cavity mirrors oscillate in phase should not show up in the error signal spectrum.

Using filters in the feedback path, i.e. filter the signal going from the PID-controller to the piezo, should avoid driving such resonances via the feedback loop and provide the possibility to improve the lock. In the following, the feedback signal is filtered with different low pass filters to suppress driving these resonances. For each filter the PID-parameters are optimized and the influence of the filters on the locked linewidth of the test ion-cavity is investigated.

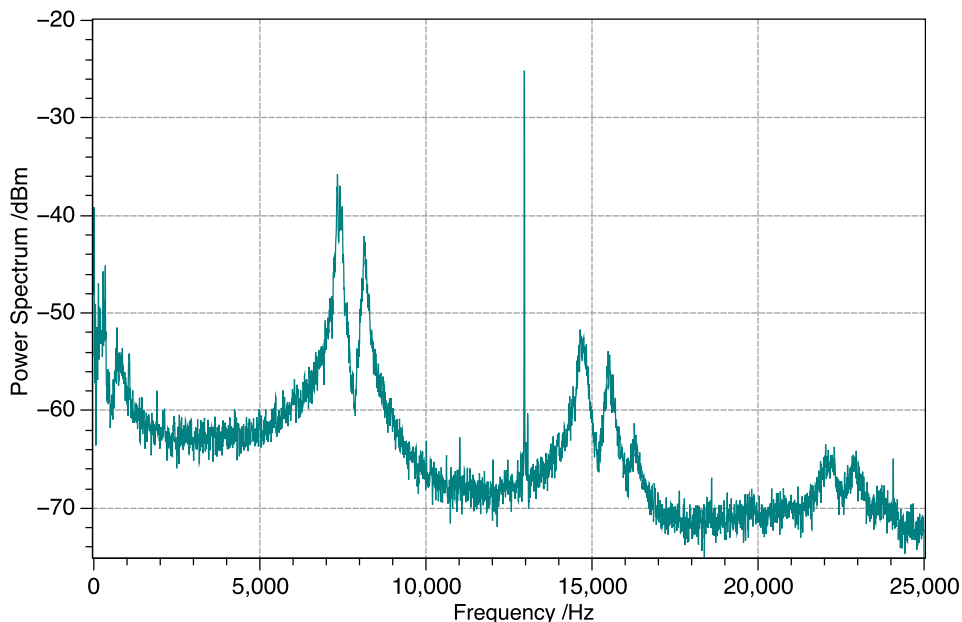


**Figure 7.5.:** Resonances of the test ion-cavity structure: This spectrum was measured with the FFT function of an oscilloscope and the average over 10 points is shown.

## Locked Linewidth

To determine to what fraction of its linewidth (1.08(8) MHz, set by the mirror properties at 785 nm) the cavity is locked to, the locked error signal spectrum was analyzed and the linewidth was determined via the scheme presented in section 3.3.1 for an arbitrary noise spectrum. First, the cavity was locked and the time-domain error signal was recorded over 200 ms with a sample number of 10000 points, using an oscilloscope. By applying an FFT algorithm and using eq. 3.40, the PSD in units of  $V^2/\text{Hz}$  was calculated from the measured data points. The PSD was converted to units of  $\text{Hz}^2/\text{Hz}$  by multiplying it with  $1/D^2$ , where  $D$  is the slope of the error signal. A linear fit (red) was matched to the lower part of the error signal slope in figure 7.4, to obtain the conversion factor  $D$  in units  $V/\text{Hz}$ .

The area between the PSD and  $\beta$ -separation line is related to the linewidth via eq. 3.46. The power spectrum was analyzed for different low pass filters (1, 2 and 5 kHz) in the feedback path. Without the filters it was impossible to switch on the P-gain of the controller and only the I-controller could be used to lock the cavity and maintain a stable lock. Using any of the filters allowed the P-gain to be switched on. As a result, low frequency noise in the PSD could be reduced.

Table 7.1 shows a comparison of the linewidths obtained with the  $\beta$ -separation line method when using different low-pass filters. The linewidth improves with the 5 kHz and 2 kHz filter, compared to the lock without filter, because the use of the P-gain reduces low frequency noise. When using the 1 kHz filter, the linewidth becomes worse again, likely because the feedback bandwidth is reduced too much by the filter. Eventually a more sophisticated filter scheme should be implemented, e.g. a notch filter which only suppresses selected frequencies corresponding to the resonance frequencies of the structure and transmits all other frequencies with little attenuation. In this way, the feedback bandwidth can be exploited as well as possible, while the driving of resonances is avoided.

**Table 7.1.:** Linewidth results of the test ion-cavity lock using different low pass filters in the feedback path. The errors in the linewidths result from the uncertainty in the error signal slope.

Filter	Linewidth	Fraction of cavity linewidth (1.08(8) MHz)
-	192(6) kHz	0.18(1)
5 kHz	133(4) kHz	0.12(1)
2 kHz	97(3) kHz	0.090(7)
1 kHz	103(3) kHz	0.095(8)

Figure 7.6 shows the PSD, averaged over 10 points, and  $\beta$ -separation line for the lock with the 2 kHz filter, for which the best linewidth result was achieved. There is still a resonance at 7 kHz visible, which had been eliminated when using the 5 kHz filter. Likely, the gain was a bit too high here. However, the noise at lower frequencies was reduced sufficiently, to provide the best linewidth result. There are also some peaks at higher frequencies in the spectrum (approximately at 13, 18.5 and 20 kHz), which do not disappear when using a filter. They don't correspond to resonances driven by the PID-controller but are related to some electronic or acoustic noise in the lab. Their origin

could not be determined. When the ion-cavity is placed in vacuum it should be shielded better from acoustic noise.

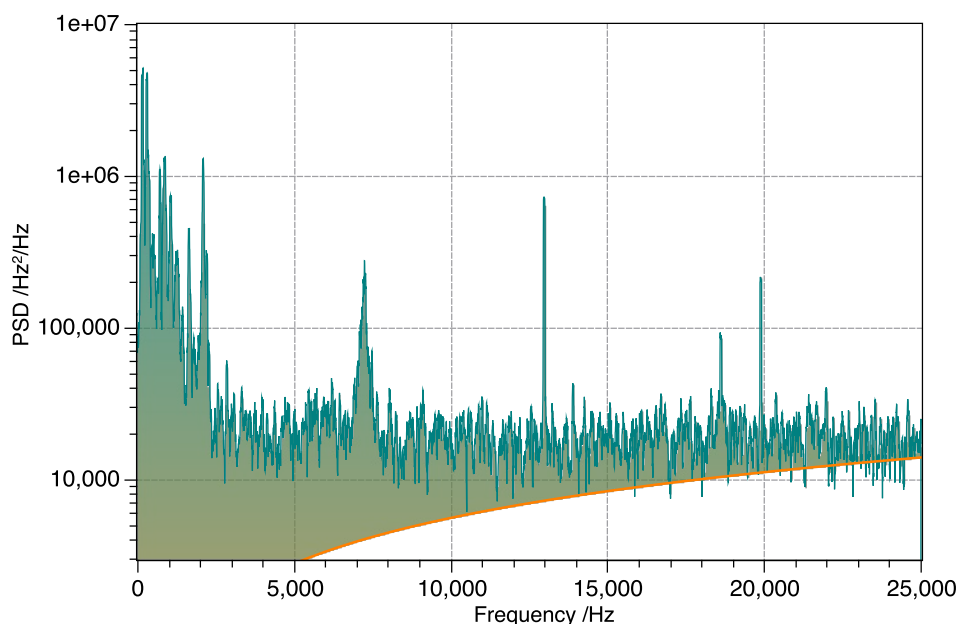


**Figure 7.6.:** PSD of the test-cavity error signal with 2kHz filter (green): The frequency resolution of the FFT is 5 Hz and the curve is averaged over 10 points. The orange line represents the  $\beta$ -separation line. The shaded area between the PSD and  $\beta$ -separation line is related to the locked linewidth of the cavity via eq. 3.46.

## 7.2. Manipulation of a Trapped $^{40}\text{Ca}^+$ Ion on the 729 nm Qubit Transition

The locked MSquared Ti:Sa laser was used to manipulate trapped  $^{40}\text{Ca}^+$  ions on the optical qubit transition in our new ion trap. When taking these measurements, the MSquared Ti:Sa was locked to our reference-cavity at 729 nm with the Digilock110 PID-controller as the FALC110 was broken <sup>3</sup>. The ion is Doppler cooled and prepared in one of the  $4^2\text{S}_{1/2} m_j$  Zeeman states state via optical pumping. The MSquared Ti:Sa laser is frequency-shifted with AOMs to the resonance of the  $4^2\text{S}_{1/2} \longleftrightarrow 3^2\text{D}_{5/2}$  transition. The laser light is switched on for a certain amount of time, before the probability for the ion to be in the excited  $3^2\text{D}_{5/2}$  state is measured via electron shelving. This is repeated 100 times for different pulse lengths of the laser. The mean excitation as a function of the pulse length is shown in figure 7.7. Rabi oscillations can be observed, which decay rather fast with a decay rate of 2500(100) per s. To improve this result, the ion should be sideband cooled to the motional ground state. In the case of an ion, which is not sufficiently cooled, the ion displays a wide thermal distribution of motional states in the

<sup>3</sup>Even though the Digilock110 has a lower bandwidth than the FALC110, the linewidth of the MSquared Ti:Sa laser locked to the reference-cavity at 729 nm for optimized PID-parameters should be the same when using either of the two PID-controllers because the limitation is not the controller bandwidth but the bandwidth of the feedback elements inside the laser.

## 7. Application of the Stabilized Laser Systems

trap, which couple to the laser with different coupling strengths [71]. This, in turn, damps out Rabi oscillations.

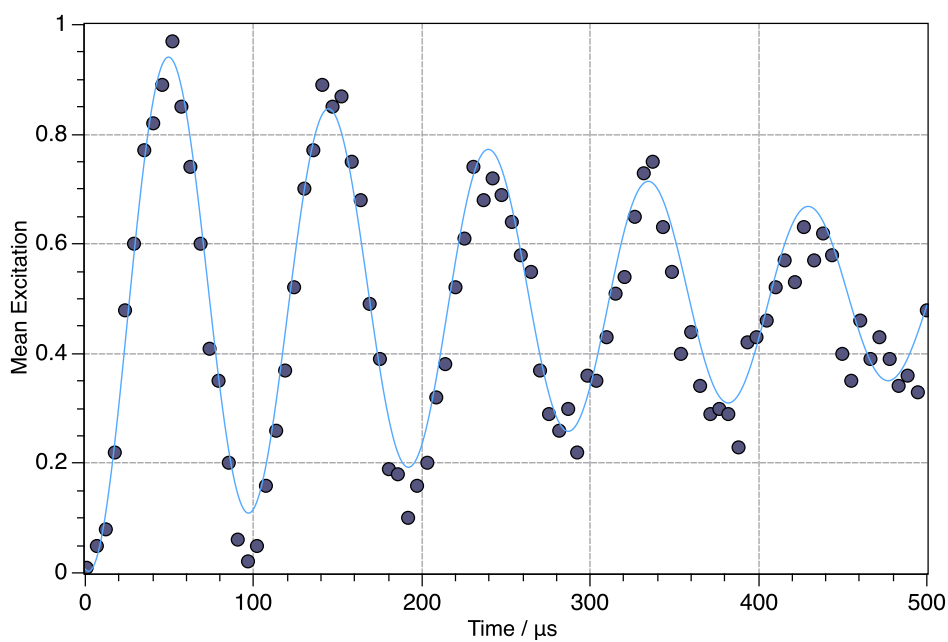


**Figure 7.7.:** Rabi flops of a trapped  $^{40}\text{Ca}^+$  ion: The grey data points represent the mean excitation as a function of the pulse length. An exponentially decaying sinusoidal fit function (blue) was matched to the data points, to determine the decay rate of the Rabi oscillations.

## 8. Conclusion and Outlook

The goal of this master's thesis was to stabilize two laser systems to linewidths of less than 10 kHz and drift rates of less than 1 Hz/s, which was achieved. These locked lasers will be used to frequency-stabilize a cavity-mediated Raman process via a transfer lock approach. Such a process allows for the deterministic generation of single 854 nm photons from a trapped  $^{40}\text{Ca}^+$  ion, such that a coherent light-matter interface for trapped-ion quantum networks can be implemented.

In the course of this thesis, an ultrastable reference-cavity was put in vacuum. The cavity's finesse around 785 nm and 729 nm was determined via ringdown measurements. A diode laser and Ti:Sa laser were locked to the reference-cavity via a PDH laser locking scheme. The locks are stable over many hours.

The linewidths and drift rates of the locked lasers were determined via frequency beat measurements with a frequency comb. The linewidth results are: less than 100 Hz for the MSquared Ti:Sa laser and less than 200 Hz for the diode laser, over a timescale of 12 s. The absolute drift of the MSquared Ti:Sa laser was determined to be 202(1) mHz/s, likely resulting from the aging-related drift of the reference-cavity. Residual amplitude modulation due to an EOM used in the locking setup of the diode laser resulted in drifts of the diode laser, additional to the aforementioned cavity related drift. This EOM has since been replaced by one which contains two crystals in a compensation configuration, that reduces changes in residual amplitude modulation and allows for higher stability.

Moreover, a test ion-cavity, similar to the one which will be used around the trapped ion, but with lower finesse, was locked in air using a PDH locking scheme to 9.0(7) % of its linewidth. In vacuum, factors which degrade the stability of the cavity lock, such as air pressure and temperature fluctuations should be reduced such that a higher stability is anticipated. The resonances of the test ion-cavity structure were determined. This information can be used to implement a filter scheme to avoid driving these resonances in our final ion-cavity setup.

The MSquared Ti:Sa laser was also locked to the reference-cavity at 729 nm, where the finesse of the cavity is much higher. A laser linewidth of less than 30 Hz was achieved over a timescale of 11.5 s. Likely, this linewidth is limited by the bandwidth of the feedback elements of the laser. A straight-forward improvement would be to install an AOM at the output of the laser to be able to apply higher frequency feedback and narrow the linewidth to 1 Hz. Using the 729 nm laser that was stabilized in this thesis, Rabi flops were observed with a trapped  $^{40}\text{Ca}^+$  ion.

The next step is to place an ion-cavity inside the vacuum chamber and attempt to lock it using the frequency-stabilized diode laser as a reference. Then, a cavity-mediated Raman process will be implemented, where the frequency-stabilized MSquared Ti:Sa laser will drive one arm of the Raman transition and the ion will couple to the locked ion-cavity on the other arm of the Raman transition, which triggers the generation of a single 854 nm

## 8. *Conclusion and Outlook*

photon. This trapped-ion cavity system will then act as one of the three nodes of the SciNet quantum network.

## A. PDH Error Signals of the Lasers at 785 nm and 729 nm

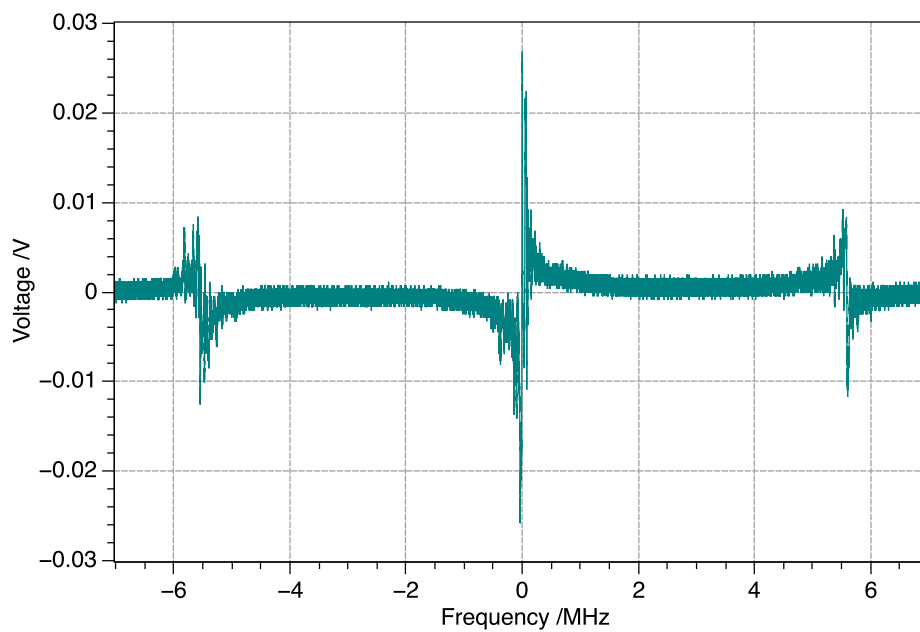


**Figure A.1.:** Error signal of the diode laser at 785 nm with modulation frequency 5.7 MHz and light power of  $70 \mu\text{W}$  going to the reference-cavity. This signal was measured by applying a triangle voltage to the grating piezo of the ECDL.

A. PDH Error Signals of the Lasers at 785 nm and 729 nm

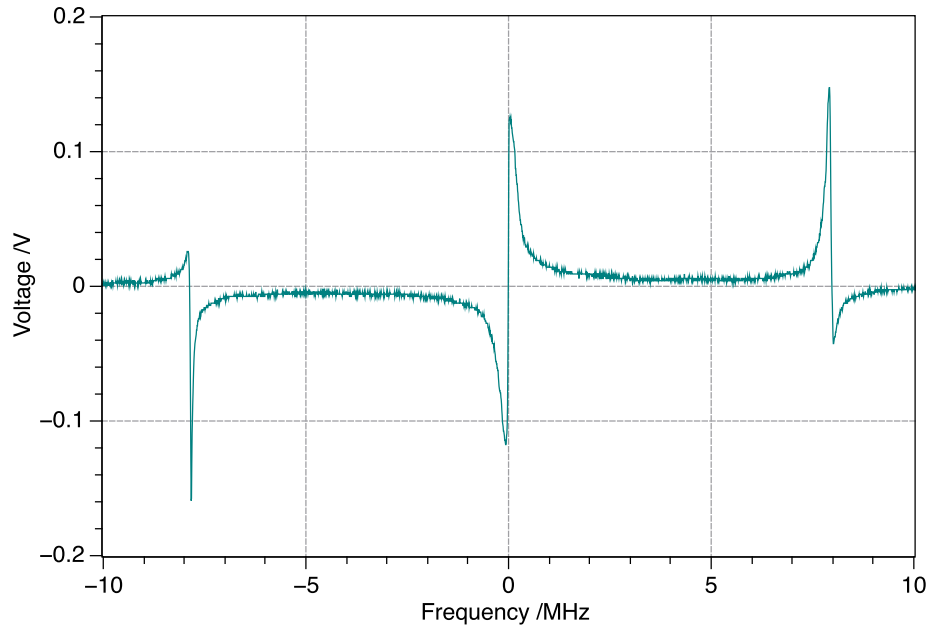


**Figure A.2.:** Error signal of the Ti:Sa at 785 nm with modulation frequency 8 MHz, light power of  $70 \mu\text{W}$  going to the reference-cavity and reflected photodiode signal amplified with MiniCircuits ZFL-1000 amplifier. This signal was measured by applying a triangle voltage to the slow piezo inside the laser cavity. The phase of this error signal is slightly off but still suitable for locking.

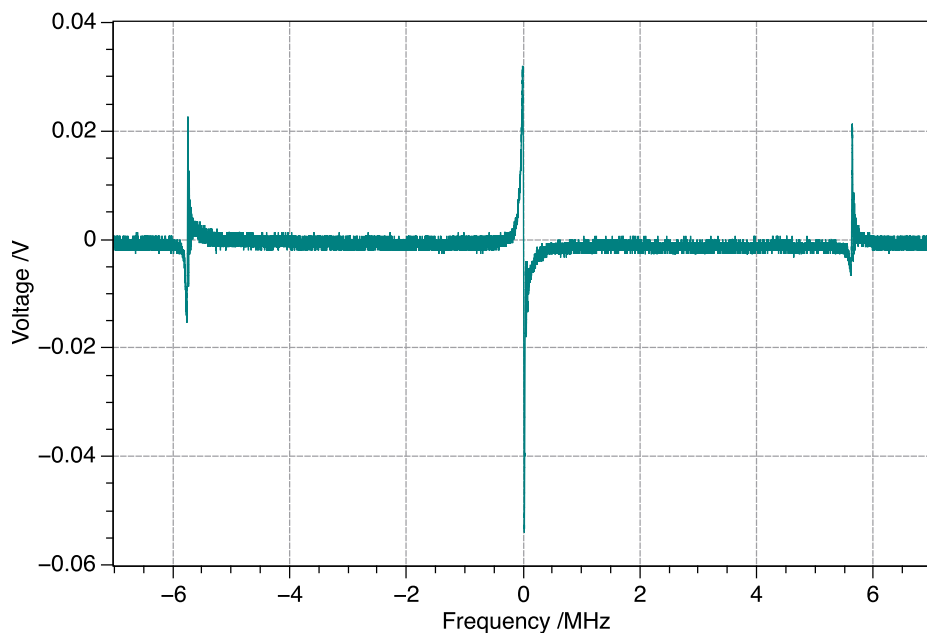


**Figure A.3.:** Error signal of the Ti:Sa at 729 nm with modulation frequency 5.7 MHz, light power of  $20 \mu\text{W}$  going to the reference-cavity and reflected photodiode signal amplified with MiniCircuits ZFL-1000 amplifier. The S/N ratio here is worse compared to the previous MSquared error signal at 785 nm due to the lower light power resonating inside the cavity. This signal was measured by applying a triangle voltage to the slow piezo inside the laser cavity.

## B. Beat Note Between Diode Laser and MSquared Ti:Sa Laser

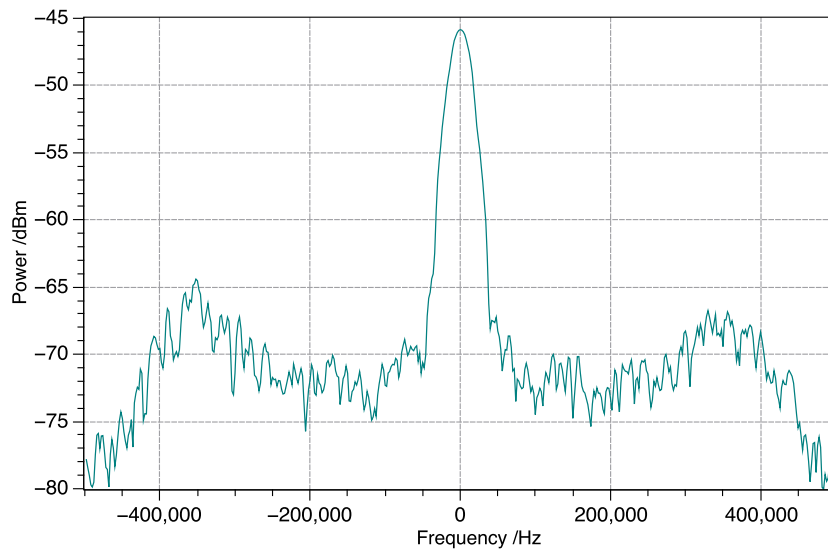


**Figure B.1.:** Beat between the diode laser and MSquared Ti:Sa laser locked to two adjacent modes of the reference-cavity: Servo bumps of the diode laser at  $\sim 400$  kHz are visible.

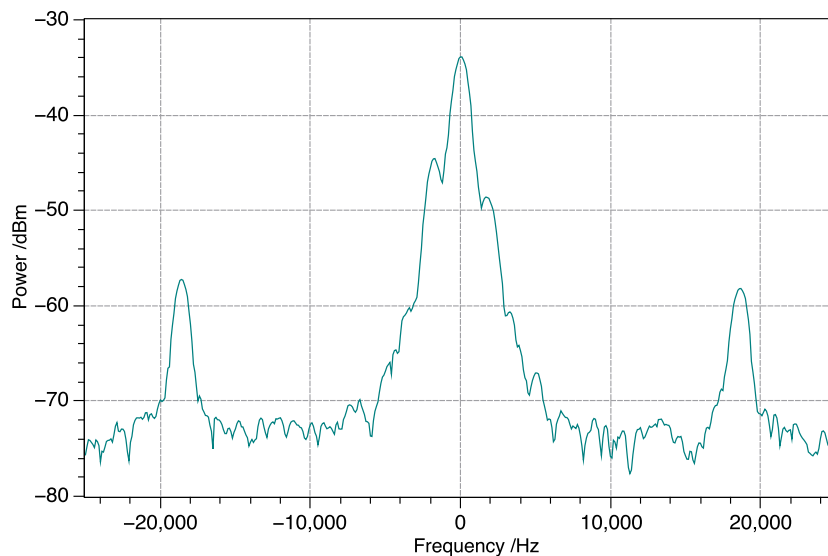


**Figure B.2.:** Beat between the diode laser and MSquared Ti:Sa laser locked to two adjacent modes of the reference-cavity: Sidebands caused by the MSquared Ti:Sa laser etalon dithering at a frequency of 19 kHz are visible.

## C. Laser Drift Measurements

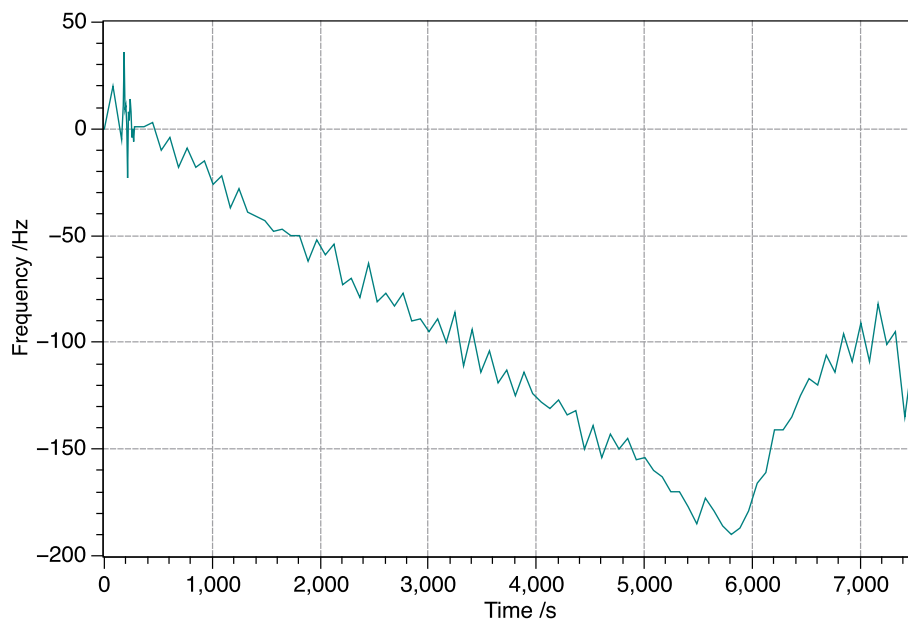


**Figure C.1.:** Frequency of the QSim 729 nm laser, measured in Ramsey experiments with a trapped  $^{40}\text{Ca}^+$  ion. At approximately 6000 s the laser unlocked.

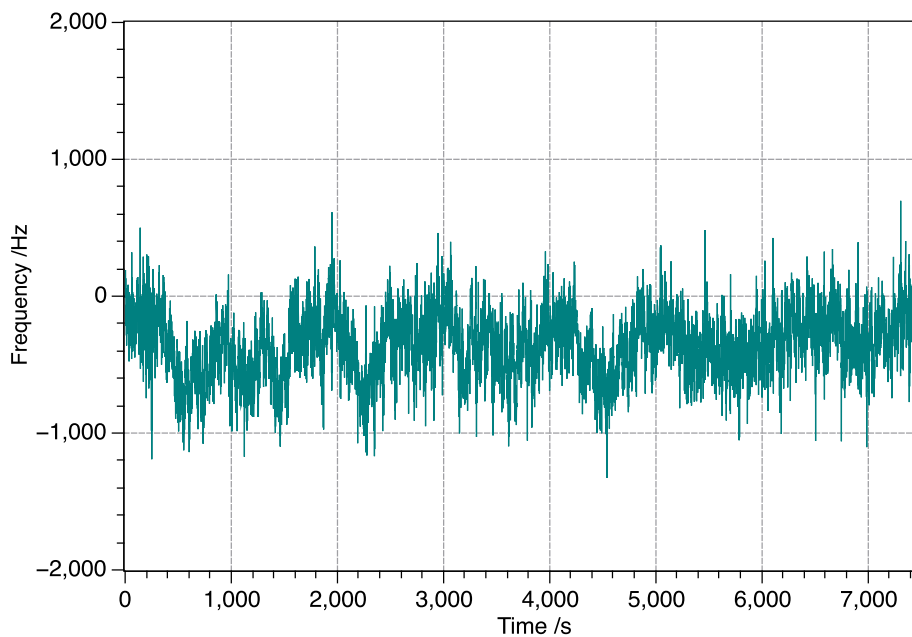


**Figure C.2.:** Beat between the QSim 729 nm and the frequency comb.

### C. Laser Drift Measurements

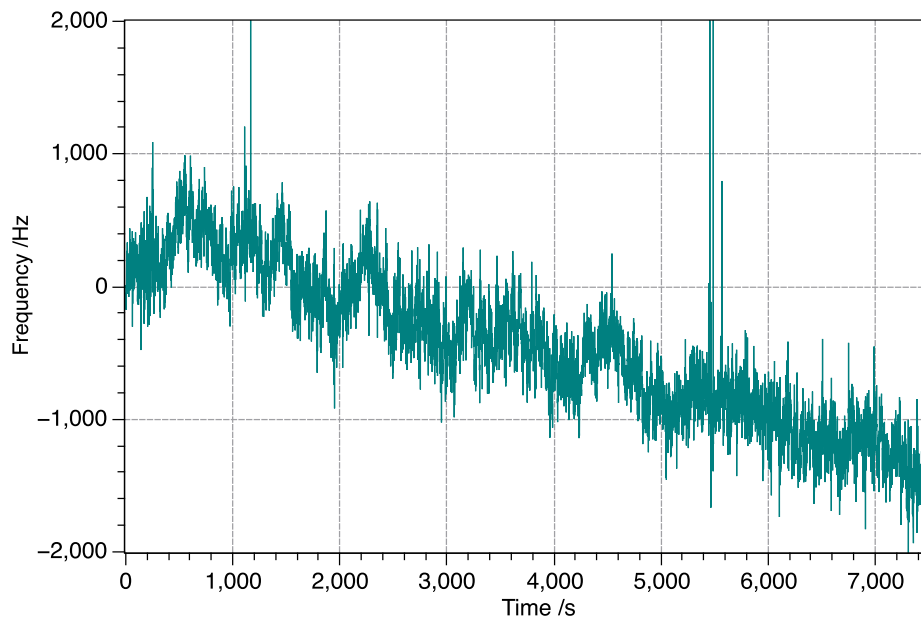


**Figure C.3.:** Beat between the MSquared Ti:sa laser and frequency comb. The cycle slips result from knocking the table the Ti:Sa and diode laser are on.

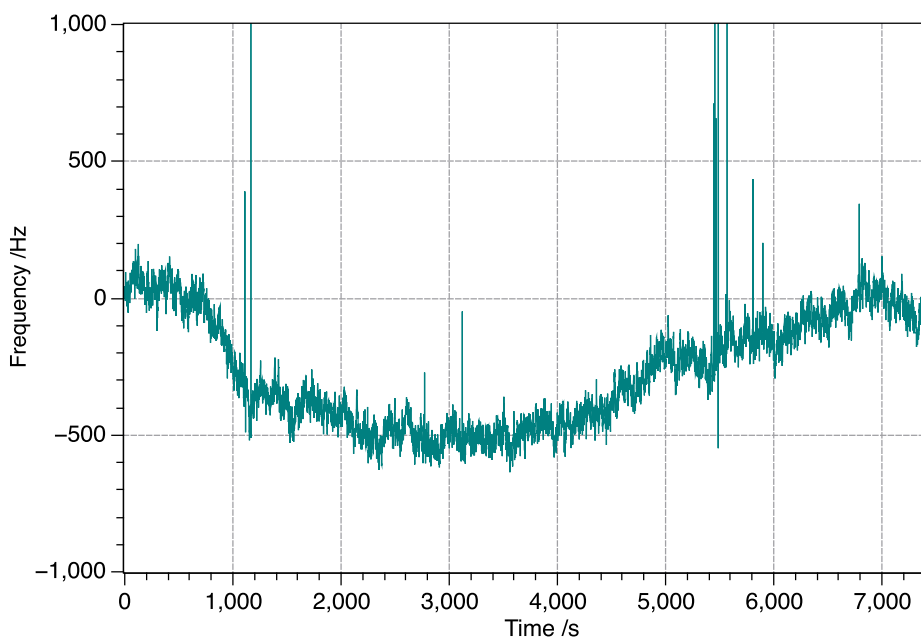


**Figure C.4.:** Beat between diode laser and MSquared Ti:Sa laser. The cycle slips result from knocking the table the two lasers are on.

# Bibliography

- [1] P. Zoller, T. Beth, D. Binosi, R. Blatt, H. Briegel, D. Bruss, T. Calarco, J. I. Cirac, D. Deutsch, J. Eisert, A. Ekert, C. Fabre, N. Gisin, P. Grangiere, M. Grassl, S. Haroche, A. Imamoglu, A. Karlson, J. Kempe, L. Kouwenhoven, S. Kröll, G. Leuchs, M. Lewenstein, D. Loss, N. Lütkenhaus, S. Massar, J. E. Mooij, M. B. Plenio, E. Polzik, S. Popescu, G. Rempe, A. Sergienko, D. Suter, J. Twamley, G. Wendin, R. Werner, A. Winter, J. Wrachtrup, and A. Zeilinger, “Quantum information processing and communication,” *The European Physical Journal D - Atomic, Molecular, Optical and Plasma Physics* **36**, 203–228 (2005).
- [2] C. H. Bennett and G. Brassard, “Quantum cryptography: Public key distribution and coin tossing,” *Theoretical Computer Science* **560**, 7 – 11 (2014), *theoretical Aspects of Quantum Cryptography – celebrating 30 years of BB84*.
- [3] V. Giovannetti, S. Lloyd, and L. Maccone, “Quantum-enhanced measurements: Beating the standard quantum limit,” *Science* **306**, 1330–1336 (2004), <http://www.sciencemag.org/content/306/5700/1330.full.pdf> .
- [4] T. Monz, D. Nigg, E. A. Martinez, M. F. Brandl, P. Schindler, R. Rines, S. X. Wang, I. L. Chuang, and R. Blatt, “Realization of a scalable shor algorithm,” *Science* **351**, 1068–1070 (2016), <http://science.sciencemag.org/content/351/6277/1068.full.pdf> .
- [5] B. P. Lanyon, C. Hempel, D. Nigg, M. Müller, R. Gerritsma, F. Zähringer, P. Schindler, J. T. Barreiro, M. Rambach, G. Kirchmair, M. Hennrich, P. Zoller, R. Blatt, and C. F. Roos, “Universal digital quantum simulation with trapped ions,” *Science* **334**, 57–61 (2011), <http://science.sciencemag.org/content/334/6052/57.full.pdf> .
- [6] P. W. Shor, “Fault-tolerant quantum computation,” in *Proceedings of 37th Conference on Foundations of Computer Science* (1996) pp. 56–65.
- [7] J. I. Cirac, A. K. Ekert, S. F. Huelga, and C. Macchiavello, “Distributed quantum computation over noisy channels,” *Physical Review A* **59** (1999).
- [8] P. W. Shor and J. Preskill, “Simple proof of security of the BB84 quantum key distribution protocol,” *Phys. Rev. Lett.* **85**, 441–444 (2000).
- [9] W. Dür, H.-J. Briegel, J. I. Cirac, and P. Zoller, “Quantum repeaters based on entanglement purification,” *Phys. Rev. A* **59**, 169–181 (1999).
- [10] D. J. Wineland, “Nobel lecture: Superposition, entanglement, and raising schrödinger’s cat,” *Rev. Mod. Phys.* **85**, 1103–1114 (2013).

## Bibliography

- [11] J. I. Cirac, P. Zoller, H. J. Kimble, and H. Mabuchi, “Quantum state transfer and entanglement distribution among distant nodes in a quantum network,” *Phys. Rev. Lett.* **78**, 3221–3224 (1997).
- [12] C. M. da Silva Baptista Russo, *Photon statistics of a single ion coupled to a high-finesse cavity*, Ph.D. thesis, University of Innsbruck (2008).
- [13] A. Stute, *A light-matter quantum interface: ion-photon entanglement and state mapping*, Ph.D. thesis, University of Innsbruck (2012).
- [14] A. Stute, B. Casabone, B. Brandstätter, K. Friebe, T.E. Northup, and R. Blatt, “Quantum-state transfer from an ion to a photon,” *Nat Photon* **7**, 219–222 (2013).
- [15] A. Stute, B. Casabone, P. Schindler, T. Monz., P.O. Schmidt, B. Brandstätter, T.E. Northup, and R. Blatt, “Tunable ion-photon entanglement in an optical cavity,” *Nature* **485**, 482–485 (2012).
- [16] V. Krutyanskiy, M. Meraner, J. Schupp, and B. P. Lanyon, “Polarisation-preserving photon frequency conversion from a trapped-ion-compatible wavelength to the telecom c-band,” *Applied Physics B* **123**, 228 (2017).
- [17] M. A. Nielsen and I. L. Chuang, *Quantum Computation And Quantum Information* (Cambridge University Press, Cambridge, 2000).
- [18] H. J. Kimble, “The quantum internet,” *Nature* **453**, 1023–1030 (2008).
- [19] C. H. Bennett, G. Brassard, S. Popescu, B. Schumacher, J. A. Smolin, and W. K. Wootters, “Purification of noisy entanglement and faithful teleportation via noisy channels,” *Phys. Rev. Lett.* **76**, 722–725 (1996).
- [20] A. Gali, “Theory of the neutral nitrogen-vacancy center in diamond and its application to the realization of a qubit,” *Phys. Rev. B* **79**, 235210 (2009).
- [21] S. Ritter, C. Nolleke, C. Hahn, A. Reiserer, A. Neuzner, M. Uphoff, M. Mücke, E. Figueroa, J. Bochmann, and G. Rempe, “An elementary quantum network of single atoms in optical cavities,” *Nature* **484**, 195–200 (2012).
- [22] T. E. Northup and R. Blatt, “Quantum information transfer using photons,” *Nat Photon* **8**, 356–363 (2014).
- [23] I. V. Inlek, C. Crocker, M. Lichtman, K. Sosnova, and C. Monroe, “Multispecies trapped-ion node for quantum networking,” *Phys. Rev. Lett.* **118**, 250502 (2017).
- [24] C. Gardiner and P. Zoller, *The Quantum World of Ultra-Cold Atoms and Light Book II: The Physics of Quantum-Optical Devices*, Vol. 4 (Imperial College Press, London, 2015).
- [25] C. Maurer, C. Becher, C. Russo, J. Eschner, and R. Blatt, “A single-photon source based on a single  $\text{Ca}^+$  ion,” *New Journal of Physics* **6**, 94 (2004).

## Bibliography

- [26] J.-G. Ren, P. Xu, H.-L. Yong, L Zhang, S.-K. Liao, J. Yin, W.-Y. Liu, W.-Q. Cai, M. Yang, L. Li, K.-X. Yang, X. Han, Y.-Q. Yao, J. Li, H.-Y. Wu, S. Wan, L. Liu, D.-Q. Liu, Y.-W. Kuang, Z.-P. He, P. Shang, C. Guo, R.-H. Zheng, K. Tian, Z.-C. Zhu, N.-L. Liu, C.-Y. Lu, R. Shu, Y.-A. Chen, C.-Z. Peng, J.-Y. Wang, and J.-W. Pan, “Ground-to-satellite quantum teleportation,” *Nature* **549**, 70–73 (2017).
- [27] C. Gobby, Z. L. Yuan, and A. J. Shields, “Quantum key distribution over 122 km of standard telecom fiber,” *Applied Physics Letters* **84**, 3762–3764 (2004), <https://doi.org/10.1063/1.1738173> .
- [28] J. I. Cirac and P. Zoller, “Quantum computations with cold trapped ions,” *Phys. Rev. Lett.* **74**, 4091–4094 (1995).
- [29] T. Monz, P. Schindler, J. T. Barreiro, M. Chwalla, D. Nigg, W. A. Coish, M. Harlander, W. Hänsel, M. Hennrich, and R. Blatt, “14-qubit entanglement: Creation and coherence,” *Phys. Rev. Lett.* **106**, 130506 (2011).
- [30] R. Blatt and C. F. Roos, “Quantum simulations with trapped ions,” *Nature Physics* **8**, 277 EP – (2012).
- [31] T. Monz, *Quantum information processing beyond ten ion-qubits*, Ph.D. thesis, University of Innsbruck (2011).
- [32] L.-M. Duan and C. Monroe, “Quantum networks with trapped ions,” *Rev. Mod. Phys.* **82**, 1209–1224 (2010).
- [33] P. A. Barton, C. J. S. Donald, D. M. Lucas, D. A. Stevens, A. M. Steane, and D. N. Stacey, “Measurement of the lifetime of the  $3d^2D_{5/2}$  state in  $^{40}\text{Ca}^+$ ,” *Phys. Rev. A* **62**, 032503 (2000).
- [34] M. G. Raizen, J. M. Gilligan, J. C. Bergquist, W. M. Itano, and D. J. Wineland, “Ionic crystals in a linear paul trap,” *Phys. Rev. A* **45**, 6493–6501 (1992).
- [35] T.W. Hänsch and A.L. Schawlow, “Cooling of gases by laser radiation,” *Optics Communications* **13**, 68 – 69 (1975).
- [36] J. Jin and D. A. Church, “Precision lifetimes for the  $\text{Ca}^+$  4p  $^2\text{P}$  levels: Experiment challenges theory at the 1% level,” *Phys. Rev. Lett.* **70**, 3213–3216 (1993).
- [37] S. Earnshaw, “On the nature of the molecular forces which regulate the constitution of the luminiferous ether,” *Trans. Camb. Phil. Soc.* **7**, 97–112 (1842).
- [38] W. Nagourney, J. Sandberg, and H. Dehmelt, “Shelved optical electron amplifier: Observation of quantum jumps,” *Phys. Rev. Lett.* **56**, 2797–2799 (1986).
- [39] J. C. Bergquist, Randall G. Hulet, Wayne M. Itano, and D. J. Wineland, “Observation of quantum jumps in a single atom,” *Phys. Rev. Lett.* **57**, 1699–1702 (1986).
- [40] T. Sauter, R. Blatt, W. Neuhauser, and P. E. Toschek, ““quantum jumps’ observed in the fluorescence of a single ion,” *Optics Communications* **60**, 287 – 292 (1986).

## Bibliography

- [41] C. Gardiner and P. Zoller, *The Quantum World of Ultra-Cold Atoms and Light Book I: Foundations of Quantum Optics*, Vol. 2 (Imperial College Press, London, 2014).
- [42] C. Cohen-Tannoudji, J. Dupont-Roc, and G. Grynberg, *Atom-Photon Interactions: Basic Process and Applications* (WILEY-VCH Verlag, 2004).
- [43] M. Chwalla, *Precision spectroscopy with  $^{40}\text{Ca}^+$  ions in a Paul trap*, Ph.D. thesis, University of Innsbruck (2009).
- [44] E. T. Jaynes and F. W. Cummings, “Comparison of quantum and semiclassical radiation theories with application to the beam maser,” *Proceedings of the IEEE* **51**, 89–109 (1963).
- [45] C. Maurer, *Kontrolle der Einphotonenemission eines einzelnen  $\text{Ca}^+$ -Ions*, Master’s thesis, University of Innsbruck (2004).
- [46] B. E. A. Saleh and M. C. Teich, *Fundamentals of Photonics*, 2nd ed. (John Wiley and Sons Inc., New Jersey, 2001).
- [47] *SolsTiS Narrow Linewidth, Tunable CW Ti:Sapphire Laser User Manual v10.3*, M Squared Lasers Ltd.
- [48] K.F. Wall and A. Sanchez, “Titanium sapphire lasers,” *Lincoln Laboratory Journal* **3**, 447–462 (1990).
- [49] W. Demtröder, *Laserspektroskopie*, 5th ed. (Springer Verlag, Berlin Heidelberg, 2007).
- [50] R. Neuhaus, *Diode Laser Locking and Linewidth Narrowing*, Tech. Rep. (TOPTICA Photonics AG, Munich, 2009).
- [51] A. E. Siegman, *Lasers* (University Science Books, California, 1986).
- [52] C. J. Hood, H. J. Kimble, and J. Ye, “Characterization of high-finesse mirrors: Loss, phase shifts, and mode structure in an optical cavity,” *Phys. Rev. A* **64**, 033804 (2001).
- [53] E. D. Black, “An introduction to Pound–Drever–Hall laser frequency stabilization,” *American Journal of Physics* **69**, 79–87 (2001), <https://doi.org/10.1119/1.1286663> .
- [54] U. Tietze, C. Schenk, and E. Gamm, *Halbleiter-Schaltungstechnik*, 15th ed. (Springer-Verlag, Berlin Heidelberg, 2016).
- [55] W. Zhang, M. J. Martin, C. Benko, J. L. Hall, J. Ye, C. Hagemann, T. Legero, U. Sterr, F. Riehle, G. D. Cole, and M. Aspelmeyer, “Reduction of residual amplitude modulation to  $1 \times 10^{-6}$  for frequency modulation and laser stabilization,” *Opt. Lett.* **39**, 1980–1983 (2014).
- [56] Thorlabs, *Electro-Optic Amplitude Modulator EO-AM-NR-Cx EO-AM-R-20-Cx Operating Manual* (2012).

## Bibliography

- [57] H. Müller, *Modern Optical Tests of Relativity*, Ph.D. thesis, Humboldt-Universität zu Berlin (2003).
- [58] L. Postler, *Ein schmalbandiges Halbleiter-Lasersystem für Quanteninformationsverarbeitung und Spektroskopie*, Master's thesis, University of Innsbruck (2015).
- [59] F. Riehle, *Frequency Standards Basics And Applications* (WILEY-VCH Verlag, Weinheim, 2004).
- [60] R.B. Randall and B. Tech, *Frequency Analysis* (Bruël and Kjøer, Denmark, 1987).
- [61] D. S. Elliott, R. Roy, and S. J. Smith, "Extracavity laser band-shape and bandwidth modification," *Phys. Rev. A* **26**, 12–18 (1982).
- [62] A. V. Oppenheim and R. W. Schaffer, *Discrete-time signal processing*, 2nd ed. (Prentice Hall Inc, New Jersey, 1998).
- [63] G. Di Domenico, S. Schilt, and P. Thomann, "Simple approach to the relation between laser frequency noise and laser line shape," *Appl. Opt.* **49**, 4801–4807 (2010).
- [64] R. Stricker, *Gatteroperationen hoher Güte in einem optischen Quantenbit*, Master's thesis, University of Innsbruck (2017).
- [65] J. Ye and S. T. Cundiff, eds., *Femtosecond Optical Frequency Comb: Principle, Operation, and Applications* (Kluwer Academic Publishers / Springer, Massachusetts, 2004).
- [66] M. Guggemos, *Precision spectroscopy with trapped  $^{40}\text{Ca}^+$  and  $^{27}\text{Al}^+$  ions*, Ph.D. thesis, University of Innsbruck (2017).
- [67] C.J. Foot, *Atomic Physics* (Oxford University Press, Oxford, 2004).
- [68] H. Häffner, C.F. Roos, and R. Blatt, "Quantum computing with trapped ions," *Physics Reports* **469**, 155 – 203 (2008).
- [69] C. Hempel, *Digital quantum simulation, Schrödinger cat state spectroscopy and setting up a linear ion trap*, Ph.D. thesis, University of Innsbruck (2014).
- [70] G. Kirchmair, *Frequency stabilization of a Titanium-Sapphire laser for precision spectroscopy on Calcium ions*, Master's thesis, University of Innsbruck (2006).
- [71] M. Teller, *Single-ion addressing for the high-fidelity implementation of quantum network protocols*, Master's thesis, University of Innsbruck (2017).

# Acknowledgments

I would like to thank all the people who were part of this experience and helped me learn so much over the course of the past year:

Ben Lanyon, for allowing me to work on this exciting project, his guidance throughout the year and for his detailed feedback on the first draft of this thesis.

Prof. Rainer Blatt for giving me the opportunity to carry out my master's thesis in such an interesting and inspiring environment.

Josef Schupp, who I spent many hours in the lab with, for his optimism and patience, and also the rest of the photon conversion team, Martin Meraner, Viktor Krutianskii and Vojtech Krcmarsky, for always taking the time for discussions, offering help when I needed it and funny conversations during tea breaks.

The guys from lab 2, Milena Guevara-Bertsch and Daniel Heinrich, who allowed me to use their frequency comb for measurements.

My office mates Christine Maier and Petar Jurcevic for many funny moments and enlightening discussions about physics.

My friends and fellow students for supporting me and always having my back.

Finally, I want to thank my parents, who made all of this possible.